UNIVERSITY OF OKLAHOMA
GRADUATE COLLEGE

POLYCAPROLACTONE-BASED COMPOSITE FOR BONE TISSUE ENGINEERING IN THE TEMPOROMANDIBULAR JOINT MANDIBULAR CONDYLE

A THESIS
SUBMITTED TO THE GRADUATE FACULTY

in partial fulfillment of the requirements for the

Degree of

MASTER OF SCIENCE

By

DYLAN M. GARCIA

Norman, Oklahoma

2025

Downloaded from SHAREOK. Persistent Handle URL: https://hdl.handle.net/11244/341383

POLYCAPROLACTONE-BASED COMPOSITE FOR BONE TISSUE ENGINEERING IN THE TEMPOROMANDIBULAR JOINT MANDIBULAR CONDYLE

A THESIS APPROVED FOR THE

STEPHENSON SCHOOL OF BIOMEDICAL ENGINEERING

BY THE COMMITTEE CONSISTING OF

Dr. John Clegg, Chair

Dr. Michael Detamore

Dr. Sarah Breen

© Copyright by DYLAN M. GARCIA 2025

All Rights Reserved.

Acknowledgements

I would like to thank my present advisor, Dr. John Clegg, and my preceding advisor, Dr. Michael Detamore, for their continuous support and guidance throughout my undergraduate and graduate time. I am grateful for the time they have spent cultivating my personal and professional growth and research goals. I would also like to thank Dr. Sarah Breen for their guidance towards career goals. In addition, I am grateful to the project clinician, Dr. Fabio Ritto, for their insights and advice towards surgical planning. Lastly, I am thankful to Dr. Preston Larson for their assistance with scanning electron microscopy.

I would like to thank Peggy and Charles Stephenson for their generosity in establishing the Stephenson School of Biomedical Engineering, promoting a healthy learning environment and cultivating my learning process.

I am highly grateful to my amazing parents Gary and Pamela Garcia, and my triplet brothers, Ryan and Nathan Garcia. I sincerely thank my grandparents Jim and Lynn Smith (Pawpaw and Nana), and Billy and Ruth Jackson (Papa Billy and Grandma Ruth) for allowing me to complete school and research stress free. Without each of them, I would not have been able to complete graduate school or advance my goals. I am deeply grateful to my fiancé, Emma Nixon, and her wonderful family, Randy, Kathy, and Adam Nixon, for their cherished weekly Sunday meals, which provided me with the nourishment and energy to tackle early Monday lab meetings.

I am thankful to all my past and current lab colleagues for their contributions towards published works. Dr. David Nedrelow for their support during my initial research growth and paving the way for my graduate work around bioresorbable biomaterials. Dr. Emi Kiyotake for their support and instruction to be a better researcher in and out of the lab. Dr. Jakob Townsend for their guidance in experimental design and expert revisions. I am grateful to Peggy Keefe for their continuous support. Lastly, I am thankful for Rana Ajeeb, Mojtaba Ghanbari Mehrabani, Chris Pierce, Ananya Datta, Mia Gonzales, and Dr. Harsh Joshi for their continuous support throughout my research journey. I sincerely thank Brandon Bueltel for motivating me to push myself not only in the research lab but also in pursuing personal growth, such as staying active at the gym, and for his genuine friendliness.

Table of Contents

Acknowledgements ..... **iv**

Table of Contents ..... **v**

List of Figures ..... **viii**

List of Tables ..... **x**

Abstract ..... **xi**

Chapter 1: Introduction **1**

1.1 The Temporomandibular Joint 1

1.2 Specific Aims 4

Aim 1: Tune the degradation and stiffness of 3D-printed biomaterial composites 4

Aim 2: Characterize tissue regeneration in sheep TMJ model 4

Chapter 2: In Vivo Advancements for Tissue Engineering the Temporomandibular Joint **5**

2.1 Abstract 5

2.2 Introduction 6

2.3 Mandibular Condyle 7

2.4 Evaluation of Bioengineered Mandibular Condyle Devices *In Vivo* 10

2.5 TMJ Disc 12

2.6 Evaluation of Bioengineered TMJ Disc Devices *In Vivo* 15

2.7 Outcome Analyses 17

2.6 Discussion 22

2.7 Conclusion 24

Chapter 3: Tuning the Mechanical Performance and Degradation Kinetics of 3D-Printed Biomaterial Composites **26**

3.1 Abstract 26

3.2 Introduction 27

3.3 Materials and methods 28

3.3.1 Materials 28
3.3.2 Composite fabrication and filament manufacturing 28
3.3.3 Fused deposition modeling 29
3.3.4 Scanning electron microscopy and energy dispersive x-ray spectroscopy 29
3.3.5 Uniaxial compression testing 30
3.3.5 Accelerated degradation 30
3.3.6 Statistical analysis 31
3.4 Results 31
3.4.1 Quality assessment of processing biomaterial particles 31
3.4.2 Quality assessment of filament fabrication 33
3.4.3 Quality assessment of 3D-FDM scaffolds 35
3.4.4 Elemental analysis of 3D-FDM scaffolds 37
3.4.5 Modulus and yield strength of porous scaffolds 41
3.4.6 Anisotropic mechanical behavior of infill architecture 43
3.4.7 Modulus and yield strength of solid scaffolds 46
3.4.8 Degradation kinetics of polycaprolactone-composite scaffolds 49
3.4.9 Mechanical property loss of polycaprolactone composite scaffolds 54
3.5 Discussion 60
3.6 Conclusion 64
Chapter 4: Bioengineering of a Patient-Specific Temporomandibular Joint Mandibular Condyle Prosthesis 66
4.1 Abstract 66
4.2 Introduction 67
4.3 Materials and methods 68
4.3.1 Materials 68
4.3.2 Composite fabrication and filament manufacturing 68
4.3.3 Image segmentation 69
4.3.4 Prosthesis: Iteration 1 69
4.3.5 Prosthesis: Iteration 2 70
4.3.6 Prosthesis: Fused deposition modeling 70

4.3.7 Guide: Iteration 1 71
4.3.8 Guide: Iteration 2 71
4.3.9 Guide: Fused deposition modeling 71
4.3.10 Sterilization 71
4.3.11 Shell thickness 72
4.3.12 Marrow packing 72
4.3.13 Dowel placement 73
4.4 Results 73
4.4.1 Prosthesis: Iteration 1 73
4.4.2 Prosthesis: Iteration 2 75
4.4.3 Guide: Iteration 1 77
4.4.4 Guide: Iteration 2 79
4.4.5 Shell Thickness 81
4.4.6 Marrow packing 83
4.5 Discussion 84
4.6 Conclusion 85
Chapter 5: Discussion and Conclusion 87
5.1 Summary 87
5.2 Future Directions 88
5.3 Conclusion 88
References 90
Appendix A 98

List of Figures

Figure 1.1: Illustrations of end stage TMD. 1
Figure 1.2: Clinical management options for temporomandibular joint (TMJ) disorders. 2
Figure 1.3: Illustration of pilot TMJ prosthesis and resected ramus. 3
Figure 2.1: TMJ tissue engineering research timeline. 7
Figure 3.1: Filament fabrication setup. 28
Figure 3.2: Quality assessment of biomaterial composite powders. 32
Figure 3.3: Quality assessment of filament fabrication. 34
Figure 3.4: Quality assessment of 3D-FDM prints. 36
Figure 3.5: Elemental analysis of 3D-FDM prints. 38
Figure 3.6: EDS peaks of elemental composition. 40
Figure 3.7: Modulus and yield stress of porous composites. 42
Figure 3.8: Quality assessment of gyroid and zigzag infill architectures. 43
Figure 3.9: Anisotropic mechanical behavior of gyroid and zigzag infill architectures. 45
Figure 3.10: Quality assessment of roller milled 3D-FDM prints. 46
Figure 3.11: Mechanical properties of solid cylindrical scaffolds prior to submersion. 48
Figure 3.12: Mass retention of solid PCL-composite scaffolds over three weeks. 51
Figure 3.13: Mass retention of solid PCL-composite scaffolds at day one and three. 52
Figure 3.14: Diameter and height retention of solid PCL-composite scaffolds over three weeks. 53
Figure 3.15: Young's modulus loss of solid PCL-composite scaffolds over three weeks. 56
Figure 3.16: Young's modulus of solid PCL-composite scaffolds at day one and three. 57
Figure 3.17: Yield stress loss of solid PCL-composite scaffolds over three weeks. 58
Figure 3.18: Yield stress of solid PCL-composite scaffolds at day one and three. 59
Figure 3.19: Infill performance dependent of print orientation on 3D-FDM build plate. 62
Figure 4.1: Condylectomy procedure for the bioengineered mandibular condyle device. 67
Figure 4.2: Illustration of the testing setup for shell thickness uniaxial compression. 72
Figure 4.3: Prosthesis Iteration 1 74
Figure 4.4: Prosthesis Iteration 2 76
Figure 4.5: Guide: Iteration 1 78
Figure 4.6: Guide: Iteration 2 80
Figure 4.7: Modulus and yield stress of bioengineered condylar prostheses with varying shell thicknesses. 82
Figure 4.8: Packing condylar heads with marrow and ground bone mixture. 83
Figure A.1: Temporomandibular joint tissue engineering triad approach. 99
Figure A.2: Scaffold biomaterials allow for tailoring mechanical, degradation, and bioactive properties. 100
Figure A.3: Fabrication of biomaterial composites. 101
Figure A.4: Energy dispersive spectroscopy of 20 wt% HAp dot and rectangular mapping. 102
Figure A.5: Ball milling versus roller milling for 6 hours. 103

Figure A.6: Macroscopic images of microarchitecture. 104
Figure A.7: Polycaprolactone long-term versus accelerated degradation. 105
Figure A.8: Porosity generation on inferior side of prosthesis. 108
Figure A.9: Tapered condyle-ramus interface. 109

List of Tables

Table 2.1: Summary of In Vivo Condylectomy Models of the Mandibular Condyle. 9
Table 2.2: Summary of In Vivo TMJ Discectomy Models of the TMJ Disc. 14
Table 2.3: Summary of Outcome Analyses for in vivo Tissue Engineering Studies of the TMJ. .. 19
Table 2.4: (Continued) 20
Table 2.5: (Continued) 21
Table A.1: Prosthesis Design Criteria 106
Table A.2: Guide Design Criteria 107

Abstract

The temporomandibular joint (TMJ) is a bilateral-complex articulation that connects the mandible to the skull, enabling essential functions such as chewing, speaking, and swallowing. TMJ disorders (TMDs) affect millions worldwide, leading to pain, dysfunction, and reduced quality of life. In severe cases involving advanced internal derangement, trauma, or osteoarthritis, surgical interventions, such as condylectomy, costochondral grafts, or total joint reconstruction may be required. These current solutions for chronic TMD management and etiology often lack patient specificity, exhibit poor long-term outcomes, and fail to adequately restore native joint function, leaving out growing patients or those with metal hypersensitivity, among others. To address these challenges, bioengineered mandibular condyle prostheses have emerged as a promising alternative, offering personalized solutions with bioresorbable materials to support tissue regeneration of the TMJ. This project aimed to develop a combinatory prosthesis composed of polycaprolactone (PCL), hydroxyapatite (HAp), and demineralized bone matrix (DBM), leveraging three-dimensional-fused deposition modeling (3D-FDM) techniques to optimize mechanical performance and degradation kinetics. Anatomical biomimicry and mechanical robustness were further enhanced using computer-aided design (CAD) and computed tomography (CT) data. Uniaxial mechanical testing demonstrated that increased bioactive material weight percentages and ball milling improved compressive properties. Under accelerated degradation conditions, PCL/DBM composites were more prone to bulk degradation compared to PCL/HAp composites, suggesting that HAp may be necessary for structural integrity. This indicates that a 50 wt% HAp composite may enhance mechanical performance and biological outcomes *in vivo* by increasing bioactive content, addressing the osteogenic limitations in our pilot study. For our future ovine animal model study, we incorporated a slurry of ground bone, bone marrow, and recombinant human bone morphogenetic protein-2 to promote controlled osteogenesis at the condyle-ramus interface. A novel 50 wt% HAp composite biomaterial, homogenized with ball milling and combined with an osteogenic cellular slurry, may further combat the limitations of existing end-stage devices by offering a patient-tailorable solution that integrates with the mandibular condyle, providing biomechanical stability and promoting bone regeneration. These advancements offer a significant step toward clinically translatable TMJ mandibular condyle replacements.

Chapter 1: Introduction

1.1 The Temporomandibular Joint

The temporomandibular joint (TMJ) is considered the most used joint in the body. Commonly referred to as a ginglymoarthrodial joint, the TMJ environment consists of the temporal bone, articular disc, and the temporal bone, bi-laterally, forming a hinge-like joint allowing sliding and rotation (1). The mandibular condyle develops from the mandibular bone, whereas the articular eminence and glenoid fossa arise from the temporal bone. Together, the TMJ is essential for daily functions such as speaking, facial expressions, and mastication, all fundamental to maintaining a higher quality of life.

A 2024 epidemiological study revealed that temporomandibular joint disorder (TMD)-related symptoms are prevalent in 34% of the worldwide population, costing an estimated $4 billion annually (2). Yet, only 10% of patients seek conservative and non-invasive therapies, such as physiotherapy and pharmacological treatment, for symptomatic relief (3). In the case of prevailing TMJ dysfunction (1-5%), that is, internal derangement, osteoarthritis, and trauma, patients often seek surgical interventions **(Figure 1.1)** (4; 5). TMJ disorder (TMD) symptoms can range from painful joint clicking, limited mastication, and/or chronic localized pain around the joint (6). Therefore, the pathology and etiology of TMD are 1) complex and 2) multifactorial involving not only the facial musculature and bony features but systemic factors such as underlying

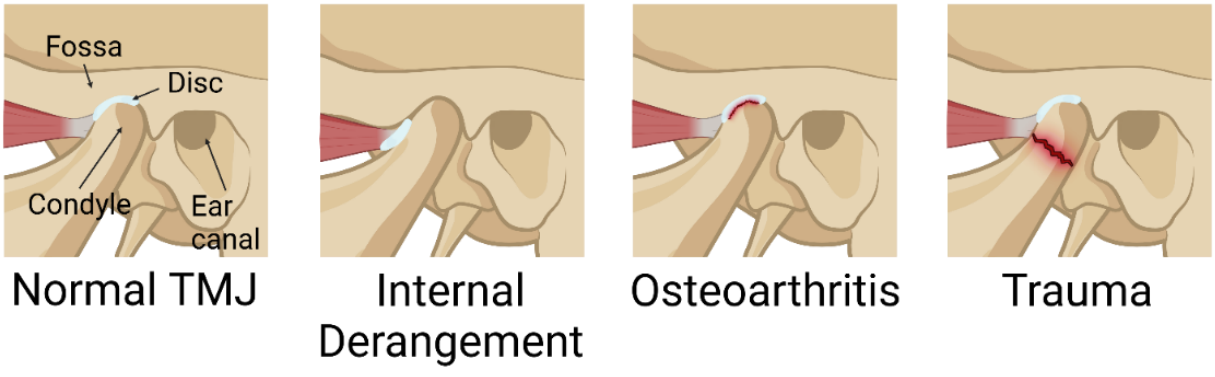

Figure 1.1: Illustrations of end stage TMD.

For simplicity, only the lateral pterygoid muscle disc attachment was included. Inferiosuperiorly, the TMJ is composed of mandibular condyle, disc, and fossa. The ear canal rests posteriorly. Common chronic TMD includes internal derangement, osteoarthritis, and trauma, all requiring surgical intervention. Created in https://BioRender.com.

conditions, infections, and overall physiological health (7). Therefore, management options and treatment must be optimized to individual patient needs.

Generally, after a detailed physical examination, conservative treatments are implemented. Conservative treatments are not limited to physiotherapy and pharmacological treatment, but as well as splints, bite guards, and counseling (5; 8). If respective symptoms continue, minimally invasive treatments may be explored, such as arthroplasty or arthrocentesis for early stage TMD and diagnosing (1; 5). If chronic pain persists or minor surgeries fail, open surgical reconstruction is considered. For unsalvageable degeneration (i.e., arthritis), or defects in the mandibular condyle or disc, condylectomy and discectomy may be used to excise the tissue. Generating severe malocclusion, FDA-approved total joint replacement (TJR) alloplastic grafts are considered, replacing the entire TMJ joint **(Figure 1.2)** (9). However, TJR may require follow-up surgeries due to complications or elicit inflammatory responses through residual nickel from metal alloys (3; 10; 11). Another surgical intervention, costochondral grafts, has been used in the management of end-stage TMD, especially for growing children (12). A costochondral graft harvests the patient's rib bone to mimic the mandibular condyle. However, autologous grafts involve a second surgical site and risk unpredictable growth, delaying functional recovery and causing further complications (13; 14). While recent reports of TJR and costochondral graft surgical implementation demonstrate improvements in facial symmetry, occlusion, depression, and quality of life, alloplastic replacements cannot restore TMJ functionality in juvenile patients or those with



Figure 1.2: Clinical management options for temporomandibular joint (TMJ) disorders.

Non-invasive treatments include splints, NSAIDs, and hyaluronic injections. Minimally invasive treatments such as arthroplasty (left) and arthrocentesis (right) are employed to visually observe the joint with a small arthroscopic camera or inject a steroidal solution. If these management options fail, invasive procedures, such as condylectomy and discectomy (not shown) or autologous costochondral grafts (tan) and total joint replacement (silver) are employed. Created in https://BioRender.com.

metal hypersensitivities, while costochondral grafts pose significant risks, including unpredictable growth. Moreover, both approaches often necessitate secondary surgeries, adding to the overall burden on patients (14-17).

To overcome end-stage mandibular condyle pathology for juvenile, metal-allergenic, or trauma patient populations, a bioengineered mandibular condyle may potentially be a superior replacement to functionally restore the structure. Aliphatic polyesters and bioactive biomaterials have played a significant role in maxillofacial tissue engineering (18). Utilizing these biomaterials, Detamore *et al.* fabricated a mandibular condylar device for a caprine model for 6 months (19). We used rapid three-dimensional (3D)-fused deposition modeling (FDM), computer-aided design (CAD), and computed tomography (CT) scans to produce a patient-specific TMJ device. The acellular device consisted of a synthetic polymer, polycaprolactone (PCL), and bioceramic, hydroxyapatite (HAp), relying on the blood supply from the resected ramus and TMJ environment for tissue ingrowth (**Figure 1.3**). Neocartilage was observed on the superior interface with novel bone formation internal and external to the scaffold. Yet, there was a dissatisfaction with osteogenesis in relation to scaffold degradation after excision *en bloc*. Though the PCL composite scaffold demonstrated sufficient mechanical stability, its degradation rate remained slower than the natural bone resorption process, resulting in reduced osteogenesis. To improve performance *in vivo*, we aim to produce higher bioactive material for TMJ prosthetics that optimize design tradeoffs of mechanical performance (stiffness, yield stress), degradation rate, and release of growth factors that promote osteogenesis. We hypothesize that increasing the amounts of HAp and a new material, demineralized bone matrix (DBM), will enhance the scaffold's mechanical properties and accelerate the degradation to better align with bone remolding, ultimately leading to improved regenerative outcomes *in vivo*.



Figure 1.3: Illustration of pilot TMJ prosthesis and resected ramus.

Mandibular condyle prosthesis with screw holes, generated by computed tomography (CT) to be patient specific (right). The device fits on the posterior edge of the ramus of the mandibular bone (left). A 30° angle is created by condylectomy using a cutting guide to create the resected condyle (not shown).

1.2 Specific Aims

Aim 1: Tune the degradation and stiffness of 3D-printed biomaterial composites

To optimize the performance of 3D-printed PCL-based composite scaffolds for mandibular condyle regeneration, it is essential to balance the degradation rate and stiffness of the biomaterial to match natural bone remodeling. To address this, we will fabricate composite scaffolds using 3D-FDM, incorporating varying amounts of HAp and DBM with PCL. Mechanical testing will assess stiffness and yield stress, while accelerated degradation assays will evaluate how composition influences degradation kinetics. By correlating mechanical properties and degradation data with scaffold formulations, we aim to identify the optimal combination of materials that achieves a balance between stiffness and controlled degradation. We expect that increasing the concentrations of HAp and DBM will result in enhanced mechanical properties while promoting degradation rates that are more consistent with natural bone resorption, and faster than the pilot biomaterial composite.

Aim 2: Characterize tissue regeneration in sheep TMJ model

To achieve functional restoration of the mandibular condyle, it is crucial to design a bioengineered device that supports osteogenesis, either by relying on the biomaterial properties (i.e., pilot study) or by the inclusion of growth factors, ground bone, and bone marrow slurry. To investigate this, we will evaluate PCL, HAp, and DBM composite prostheses in a condylectomy model, assessing their mechanical performance and creating design wants and constraints with project clinician guidance. The analysis will include ramus-condyle interface compression and design to characterize suitable device designs prior to *in vivo*. We expect that the hollow scaffold geometry and design will exhibit sufficient mechanical support to limit micromotion on the resected ramus and house the bioactive slurry. Combined with data from Aim 1, we aim to enhance osteogenesis by optimizing the mandibular condyle device design and biomaterial composite formulation to align with new bone formation, ultimately promoting successful mandibular condyle regeneration in a sheep TMJ model.

Chapter 2: In Vivo Advancements for Tissue Engineering the Temporomandibular Joint

2.1 Abstract

Clinically available end-stage solutions for temporomandibular joint (TMJ) disorder (TMD) include alloplastic total joint replacement or autogenous grafts, which may limit adaptability, risk foreign body reaction, and require secondary surgeries. These permanent prosthetics, which do not adapt to the patient's growth, are fabricated from a limited range of metallic materials, and are inadequate for (1) juvenile patients, (2) patients with metal hypersensitivity, and (3) patients with advanced tissue degeneration or structural damage to the TMJ. A bioengineered tissue replacement alternative, developed using biodegradable materials, stem cells, and chondrogenic/osteogenic growth factors, may offer a promising solution for restoring TMJ functionality. Researchers have previously published critical evaluation of the design and testing of TMJ prosthetic devices. However, these past analyses have not focused on summarizing and critiquing results that were specifically obtained from orthotopic models for the mandibular condyle and articular disc, two TMJ structures that are prone to painful symptoms from trauma and/or degenerative diseases. The purpose of the present review is to separately analyze the methodology, results, and outcomes from bioengineering research aimed at regenerating the mandibular condyle and articular disc in orthotopic models. Mandibular condyle tissue engineering favors bioactive-bioinert polymer scaffolds loaded with transforming growth factor (TGF) superfamily growth factors and patient-specific fabrication. Contrastingly, disc tissue engineering bodes towards scaffold-free approaches using ECM-derived, natural polymer, or cell-based scaffolds. Ultimately, our review identified common strategies that TMJ bioengineers have attempted to produce regenerative off-the-shelf replacements for the mandibular condyle and articular disc. Promising outcomes and study limitations are discussed.

2.2 Introduction

With emerging techniques in the tissue engineering field, improved clinical indications, and annual TMJ bioengineering conferences, tissue engineering applications for the TMJ are on the horizon. Over the last two decades, pioneering bioengineers have provided exemplary reviews of the TMJ field. As the field evolves, these reviews—covering structure and function, TMD indications, animal models, TMJ tissue engineering strategies, and future directions—paved the way for advancing preclinical TMJ research (**Figure 2.1**).

During TMJ tissue engineering infancy, structure and function reviews have been especially helpful for future directives for biomimicry of TMJ tissues (20-22). A decade later, clinicians and bioengineers elucidated trends to indicate, diagnose, and manage complex TMD (3; 10; 23). As *in vivo* work commenced, relevant animal models for clinical translation were identified (24; 25) and maxillofacial tissue engineering strategies were thoroughly reviewed (1; 26; 27). Discussion between bioengineers, scientists, and dental professionals during TMJ bioengineering conferences ultimately established essential clinical questions for TMJ research (28-31). Over the past two decades, there have been notably few articles exclusively reviewing *in vivo* preclinical studies. Among them, the most relevant contribution, is an excellent review by Helgeland *et al.* (13), providing a valuable analysis of scaffold-based tissue engineering in ectopic and orthotopic animal models to compare acellular versus cellular constructs for the mandibular condyle and disc. Helgeland and colleagues from Annika Rosén's group expressed that the addition of these osteogenic and chondrogenic cells enhanced TMJ tissue regeneration in six orthotopic TMJ models. From the Kyriacos Athanasiou group, Donahue *et al.* discussed the hurdles remaining for the articular disc tissue engineering field, such as, fixation/surgical techniques, device scale-up, and mechanical properties biomimicry from orthotopic, ectopic, subcutaneous, and non-implantation models. Such papers drive the need for systematic reviews, evaluating TMJ animal models and potential for promising bioengineered replacements.

Building upon the previous TMJ literature foundation, the present review aims to analyze recent advancements in scaffold-based tissue engineering for the TMJ, orthotopically, incorporating additional studies from the past seven years to provide a comprehensive overview of these *in vivo* preclinical models. TMD is the result of normal TMJ mechanical and physiological stimulation, therefore in the present review, ectopic models were excluded. We analyzed *in vivo*

preclinical models using condylectomy and discectomy surgical procedures for clinical relevancy of chronically affected TMJ structures (i.e., mandibular condyle and disc) (32). The authors are aware of osteochondral, osteoarthritis, and subcutaneous implantation models, however, such articles covering ectopic implantation (13; 33) and subcutaneous implantation have been thoroughly reviewed (34-46).

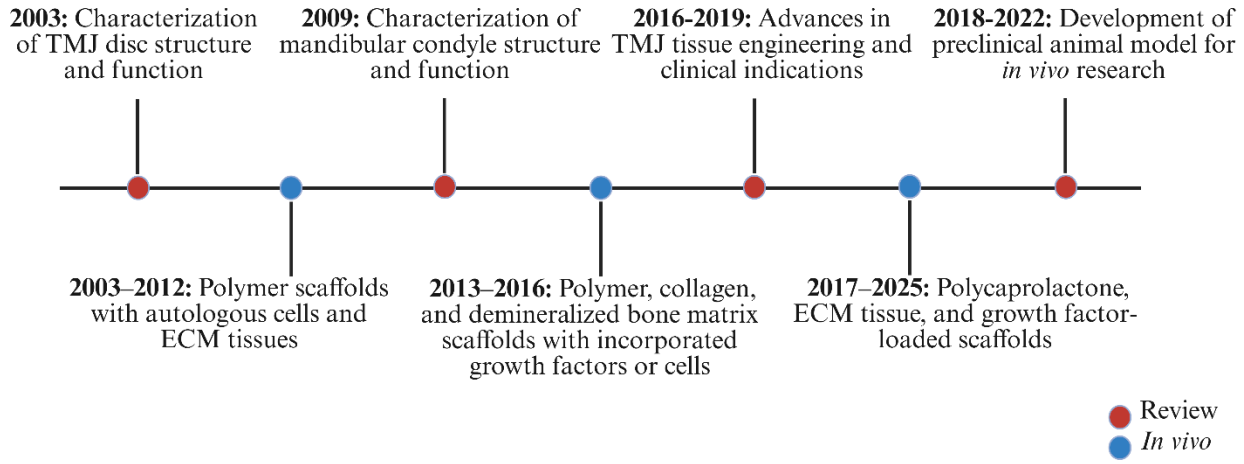

Figure 2.1: TMJ tissue engineering research timeline.

Timeline of essential reviews and pioneering in vivo work regarding the regenerative solutions to the TMJ mandibular condyle and disc. The timeline highlights key studies that enhance clinical translation of bioengineered tissues and advancements in the TMJ field. Created in https://BioRender.com.

2.3 Mandibular Condyle

Originating from the mandible and ramus, the mandibular condyle's complex mechanisms help maneuver the lower jaw, allowing the mouth to perform different facial expressions, swallow, and breathe. The mandibular condyle articulates with the glenoid fossa and articular eminence regions of the temporal bone producing translational and rotational movements for daily functions (1). Briefly, the mandibular condyle can rotate laterally, slide anteriorly, and translate or rotate anteriorly towards the other joint. Both mandibular condyles on each side can slide in opposite directions (anterior or posteriorly) (47). Human mandibular condyles are elliptical in shape and run 13-25 mm mediolateral and 6-16 mm anteroposterior (48). The range of shape and size differs for each individual and species (49). Interestingly, at the superior surface rests a layer of fibrocartilage, rather than hyaline cartilage seen in other joints (e.g., knee) (50). Fibrocartilage acts as a shock-absorber and allows for smooth sliding or rotation. Additionally, the cartilage layer is

composed of organized zones including the fibrous zone, proliferative zone, mature zone, and the hypertrophic layer to assist with load distribution. Due to unique fibrocartilage and underlying bone, consisting of limited blood supply in the surrounding disc interface and condylar neck, regeneration of a bioengineered mandibular condyle remains a challenge (26).

The mandibular condyle and ramus are critical structures within the TMJ that are susceptible to a variety of pathological conditions (51). Bioengineering these structures has become an essential area of exploration to restore functionality and improve TMD outcomes (52). A decade ago, a review was published on the potential indications for tissue engineering the TMJ (32). Comprised of relevant researchers and clinicians in the TMJ field, that is, Michael Detamore, Alejandro Almarza, Louis Mercuri, and Larry Wolford, the authors indicated selective TMD for a bioengineered mandibular condyle device. Briefly, those with 1) trauma, 2) skeletally immature patients (juvenile), 3) hyperplasia, and 4) metal hypersensitivities may be candidates. However, it is still unclear whether bioengineered mandibular condyle constructs are superior to current clinical approaches, such as costochondral grafts or total joint replacement (TJR). To explore potential regenerative solutions, preclinical studies were collected and reviewed over the last two decades (19; 53-57). Approaches using condylectomy only were evaluated to represent end stage clinical relevancy. Approaches using partial condylectomy were included to represent traumatic TMD **(Table 2.1)**. By closely examining the methods and results, the authors aim to establish reproducible and reliable models for translation into clinical practice (19; 53-59).

Table 2.1: *Summary of In Vivo Condylectomy Models of the Mandibular Condyle.*

Authors	Species	Age, Sex, Strain	n	Endpoint	Cells	Cell Source (C)	Scaffold (S)	Hydrogel (H)	GF	Conclusions
Ueki *et al.*, 2003 (53)	Rabbit	12-16 weeks, male, JW	60	2, 4, 8, 12, 24 weeks	No cells		PLA, PGA, Gelatin sponge		rhBMP-2	S + GF ≥ S > empty control
Smith *et al.*, 2007 (54)	Minipig	6-8 months, NR, Yucatan	5	1-3 months	BM	Autologous, iliac crest	PCL			3-month bone volume > 1-month bone volume > empty control
El-Bialy *et al.*, 2010 (55)	Rabbit	NR, NR, NZW	12	4 weeks	BMSC	Autologous, femur	UBM ECM, Porcine; Collagen sponge			S + ultrasound treatment > S alone > empty S + ultrasound treatment > empty control
Ciocca *et al.*, 2013 (56)	Sheep	2 years, female, NR	3	4 months	No cells		HA			Peripheral bone growth and fibrous tissue > internal bone growth and fibrous tissue
Bhumiratana *et al.*, 2016 (58)	Minipig	2 years, NR, Yucatan	14	3, 6 months	ASC	Autologous, fat	DBM, Bovine			S + C > S > empty control
Chen *et al.*, 2020 (59)	Minipig	1-2 years, male, Yucatan	19	6 months	ASC	Autologous, fat	DBM, Bovine			S + C > S > acellular scaffold
Abramowicz *et al.*, 2021 (57)	Minipig	6 months, male, Yucatan	3	6 weeks; 6 months	No cells		PCL		rhBMP-2	Healthy control ≥ S
Nedrelow *et al.*, 2023 (19)	Goat	3-5 years, female, Spanish Cross	6	4-6 months	No cells		PCL/HA	PHA/PEGDA/DVC		S ≥ S + H

NR, not reported; ASC, adipose-derived stem cells; BM, bone marrow; BMSC, bone-marrow mesenchymal stem cells; DBM, demineralized bone matrix; DVC, devitalized cartilage; ECM, extracellular matrix; HA, hydroxyapatite; n, number of animal specimens; JW, Japanese White; NZW, New Zealand White; PCL, poly(ε-caprolactone); PEGDA, poly(ethylene glycol) diacrylate; PGA, polyglycolic acid; PHA, pentanoate-modified hyaluronic acid; PLA, polylactic acid; rhBMP-2, recombinant human bone morphogenetic protein-2; UBM, urinary bladder

2.4 Evaluation of Bioengineered Mandibular Condyle Devices *In Vivo*

Several synthetic and natural polymers have been used as scaffold biomaterials for mandibular condyle tissue engineering applications. Natural polymers such as gelatin and collagen were employed in both rabbit models (53; 55). Interestingly, both groups used combinatory (synthetic or ECM) sponge scaffolds to assess bone regeneration. Ueki and colleagues evaluated the empty control condylar defect (unilateral condylectomy) using recombinant human bone morphogenetic protein-2 (rhBMP-2) and PLA/polyglycolic acid (PGA), and PGS groups at 5 timepoints up to 24 weeks (53). Compared to the empty control condylar defect, the rhBMP-2/PLA/PGA group displayed enhanced bone and cartilage tissue formation. Though the results did not elucidate the factors involved with the novel tissue formation, a bone morphogenetic protein (BMP) dosage of 2-5 μg induced significant regeneration in the mandibular condyle. However, it is still unclear whether BMP is necessarily required for osteochondral growth. Later, El-Bialy and colleagues produced urinary bladder (UBM) extracellular matrix (ECM) or collagen sponge constructs for New Zealand White (NZW) rabbits. Due to the fibrocartilage lining of the mandibular condyle and limited blood supply, self-regeneration is a challenge, especially for degenerative diseases. Thus, this group used low-intensity ultrasound treatment to stimulate chondrocyte differentiation, anticipating enhanced osteochondral regeneration. Furthermore, bone-marrow mesenchymal stem cells (BMSC) isolated from autologous femurs were expanded and seeded onto collagen sponges and inserted into the UBM ECM scaffolds. Compared to scaffolding alone, histological analysis of bone, cartilage, and fibrous tissues were increased (55). Gaining utility in TMD management, ultrasound in combination with bioengineered constructs may offer improved and accelerated osteochondral regeneration without the need for growth factors, promoting tissue healing and functional recovery more efficiently (60).

Synthetic biomaterials including polyesters, such as polylactic acid (PLA), polyglycolic acid (PGA), and polycaprolactone (PCL) were tested in larger animal models (e.g., minipig, sheep, goat). Biodegradable polyesters are generally easy to process, biocompatible, and mechanically tough (61). Smith *et al.*, Ciocca *et al.*, and Abramowicz *et al.*, opted for single polymer or bioceramic constructs only (54; 56; 57). In 2007, Smith and colleagues from the Scott Hollister group, developed a PCL mandibular condyle construct using computed tomography (CT),

displaying feasibility of scaffold development. The CT method was similarly used in scaffold construction for all tabled studies except for the rabbit model studies. Each condylar scaffold was loaded with bone marrow aspirated from autologous iliac crest and packed into the shell design. After one- and three-month timepoints, significant bone growth was observed interiorly and exteriorly. Specifically, the bone volume increased by 3-fold. Additionally, cartilaginous tissue growth was observed with safranin O (SO) staining, mimicking the fibrocartilage found on the mandibular condyle. The sole biodegradable (long-term) PCL scaffold and bone marrow aspirate is a viable option for osteochondral regeneration. Recently, Abramowicz and colleagues from the same group employed a PCL scaffold with a rhBMP-2 coating (57). Here, a two-step temporalis flap approach was used prior to mandibular condyle implantation. Briefly, the scaffold was implanted into the temporalis muscle for 6 weeks and then rotated into the mandibular condyle space. The BMP impregnated-vascularized scaffold had the ability to maintain functional condylar height, condylar volume, and bone volume fraction compared to control. Bioengineered constructs with osteoinductive growth factors hold the potential enhance bone regeneration, but other release methods, such as collagen sponges seen in clinics and previous studies, could enhance more controlled delivery (62). A decade ago, hydroxyapatite (HAp) scaffolds were implanted into sheep condyles for 4 months by Ciocca and colleagues (56). HAp is an osteoconductive bioactive material allowing osteoblasts to adhere to the scaffold, facilitating novel bone formation (61; 63). However, pure HAp exhibits low tensile strength and poor fracture toughness, making it highly brittle and unsuitable for load-bearing applications. (64). Unsurprisingly, fractures were observed in the scaffold. In large fractures, lack of osteoblastic activity can be explained by micromotion due to the movement of biomaterial during mastication. Increased peripheral bone growth and fibrous connective tissue were observed compared to the porous internal portion.

To overcome mechanical disadvantages, a common strategy is to fabricate biodegradable scaffolds blends, or composites, enabling tough bioactive scaffolds for tissue engineering (65). These composites, as seen recently in our group, have shown promising results for mandibular condyle regeneration (19). Nedrelow *et al.* displayed that through biomechanical evaluation, the scaffold stiffness (as measured by compressive modulus) increased by 67% with HAp. Integrated to the PCL-HAp composite, a pentanoate-modified hyaluronic acid (PHA)-poly(ethylene glycol) diacrylate (PEGDA)-devitalized cartilage (DVC) hydrogel was evaluated to stimulate articular cartilage regeneration (19). Though neocartilage tissues were observed, a well-integrated and

layered structure of native mandibular condyle cartilage remained a challenge after 6 months. Hydrogels may provide a solution to cartilaginous tissue regeneration, but further investigation is necessary to understand the release and degradation characteristics in orthotopic models (19). Other limitations in bone regeneration may have been due to the absence of cells or growth factors, which have been shown to enhance evident bone volume growth in scaffolds (13).

Many groups opted to omit the use of growth factors and rely on the osteogenic properties of the scaffold or cells. Specifically, Chen and colleagues from Gordana Vunjak-Novakovic's group, utilized perfusion bioreactor technology to seed and grow autologous adipose-derived stem cells (ASC) onto demineralized bone matrix (DBM) scaffolds (59). ASC are highly available and require minimally invasive harvesting, demonstrating clinical translatability. Bovine derived bone scaffolds were seeded with 3-week bioreactor perfused ASC into Yucatan minipigs (58). The cell-seeded platform resulted in strong condyle regeneration internal to the scaffold and maintained mechanical loading in the large animal model. The combinatory osteoinductive model and bioreactor technology displayed feasibility for developing bioengineered platforms (66; 67).

The use of aliphatic polyesters, ECM-derived, and demineralized constructs allowed all animal models to gain daily use over the course of the experiment. Namely, PCL, PLA, and PGA hold the potential to serve as long-term scaffolds, able to support cells and mechanical loads sustained by the mandibular condyle and disc. Combining polymers with bioceramics or hydrogels may promote enhanced regeneration while maintaining mechanical properties for the mandibular condyle. Other methods display that the use of autologous cells, harvested from the iliac crest and adipose tissue, may assist with osteochondral growth in the fibrous layers and promote superior function recovery. The use of bioreactors to grow and maintain cell viability allow culture onto scaffolds prior to implantation. The studies revealed that mandibular condyle constructs must mimic the mechanical loads and biochemical signals experienced in the TMJ to successfully restore the mandibular condyle.

2.5 TMJ Disc

Sandwiched between the mandibular condyle and temporal bone rests a dense fibrocartilaginous disc, playing a pivotal role in TMJ mechanics (20). The purpose of the disc is to facilitate smooth and efficient jaw movements during mastication and talking by distributing mechanical loads across the joint and minimizing friction between the condyle and the temporal

bone. Unlike the bony mandibular condyle, which bears significant compressive forces, the disc absorbs impact and stabilizes the joint through its fibrous, flexible structure, allowing for dynamic articulation without direct bone-to-bone contact. Additionally, the nonhomogeneous disc serves as a cushion between the mandibular condyle and fossa-eminence complex, reducing the forces generated onto the bony surfaces (20). Mirroring the shape of the mandibular condyle, the elliptical articular disc is divided into three zones: anterior band, intermediate zone, and posterior band (20). The overall shape is longer mediolateral (23 mm) than anteroposterior (14 mm) and is maintained in place by fibrous connective tissue. The three zones and structures assist with transmitting forces, translation, and rotation. Further structure function of the disc can be found here (20). Briefly, the fibroblast- and chondrocyte-like cells run in the intermediate zone and periphery, respectively. Cells are more prevalent in the anterior and posterior bands than the intermediate zone and vary for species and age (3). The disc is highly fibrous and contains mainly type I collagen, similarly to the fibrocartilage lining on the mandibular condyle. Enclosed within a fibrous connective tissue capsule, the disc is surrounded by synovial fluid, which serves as a lubricant for both an upper and lower cavity (22; 68; 69). Yet, the disadvantage lies in the avascularity of the disc, requiring the capsule for nutrient and waste exchange. Limitations of vasculature contribute to the disc's vulnerability to degenerative changes and trauma over time (70).

Indications for a bioengineered TMJ disc are for TMD include, but are not limited to, 1) disc trauma, 2) Wilkes stage III and IV internal derangement, and 3) as a complement to a bioengineered mandibular condyle (32). Creating biomimetic disc replacements remains a challenge due to the complex disc shape and various biochemical compositions along the different zones. Preclinical studies have explored various platforms for addressing disc pathology, using mainly unilateral/bilateral or partial discectomy. These recent studies aim to evaluate the feasibility of bioengineered approaches for disc substitution regeneration. Approaches using unilateral/bilateral discectomy were evaluated to represent internal derangement (Wilkes) clinical relevancy. Approaches using partial discectomy were included to represent disc trauma **(Table 2.2)**. By closely examining the methods and conclusions, the authors aim to offer valuable insights into the regenerative potential of these models (71-83).

***Table 2.2**: Summary of In Vivo TMJ Discectomy Models of the TMJ Disc.*

Authors	Species	Age, Sex, Strain	n	Bilateral/ Unilateral or Partial	Endpoint	Cells (C)	Cell Source	Scaffold (S)	GF (G)	Conclusions
Chan *et al.*, 2004 (71)	Rabbits	3 months, male, NZW	24	Partial	3 months	No cells		Collagen, Bovine; Subdermal graft		Collagen S ≥ subdermal S > empty control
Lai *et al.*, 2005 (72)	Rabbits	3 months, male, NZW	44	Partial	1, 2, and 3 months	No cells		Collagen, Bovine; Subdermal graft		Collagen S ≥ subdermal S > empty control
Brown *et al.*, 2011 (73)	Canine	NR, female, Mongrel	7	Bilateral and Unilateral	3, 4, 8, 12, and 24 weeks	No cells		UBM ECM, Porcine		Healthy control ≥ UBECM device > empty control
Brown *et al.*, 2012 (74)	Canine	NR, female, Mongrel	10	Bilateral	6 months	No cells		UBM ECM, Porcine		Healthy control ≥ UBECM device > empty control
Ahtiainen *et al.*, 2013 (75)	Rabbit	2.5-3 years, female, NZW	10	Bilateral	6 and 12 months	ASC	Autologous, neck	PLA	TGF-β1	C + S + G > C + S
Kobayashi *et al.*, 2015 (76)	Rabbit	NR, male, JW	18	Partial	2, 4, and 8 weeks	MSC	Autologous, bone marrow aspirate	Collagen, Porcine		C + S > S > empty control
Tarafder *et al.*, 2016 (77)	Rabbit	NR, NR, NZW	8	Partial	6 weeks	No cells		PLGA μS + PCL	CTGF + TGF-β3	Healthy control ≥ S + G > S
Wang *et al.*, 2017 (78)	Rabbit	3 months, male, NZW	36	Partial	1, 2, and 3 months	No cells		Collagen, Bovine		Healthy control ≥ S > empty control
Vapniarsky *et al.*, 2018 (79)	Minipig	NR, NR, Yucatan	19	Bilateral	2 and 8 weeks	cC	Allogeneic, rib		TGF-β1 + LOXL2 + C-ABC	C > empty control
Ângelo *et al.* 2022 (80)	Sheep	2-5 years, female, Black Merino	24	Bilateral	6 months	No cells		PGS + PCL, PEGDA + PCL, PCL		PGS + PCL ≥ PEGDA + PCL = PCL
Brown *et al.*, 2022 (81)	Pig	3-9 months, female, NR	30	Bilateral and Unilateral	2, 4, 12, and 24 weeks	No cells		SIS ECM, Porcine		S > empty control
Chung *et al.*, 2022 (82)	Canine	12-15 months, female, Beagle	5	Bilateral	22 days	No cells		SIS ECM, Porcine		S > empty control
Jeong *et al.*, 2025 (83)	Minipig	16-18 months, female and male, Yucatan	11	Unilateral	3 months	No cells		PLGA μS + PCL	CTGF + TGF-β3	S + G > empty control

NR, not reported; ASC, adipose stem cells; C-ABC, chondroitinase ABC; cC, costal cartilage; CTGF, connective tissue growth factor; ECM, extracellular matrix; JW, Japanese White; LOXL2, lysyl oxidase-like 2; MSC, mesenchymal stem cells; NZW, New Zealand White; PCL, poly(ε-caprolactone); PEGDA, poly(ethylene glycol) diacrylate; PGS, poly(glycerol sebacate); PLA, polylactic acid; PLGA, poly(lactic-co-glycolic) acid; SIS, small intestine submucosa; TGF-β1, transforming growth factor beta 1; TGF-β3, transforming growth factor beta 3; UBM, urinary bladder; μS, microspheres.

2.6 Evaluation of Bioengineered TMJ Disc Devices *In Vivo*

TMJ disc regeneration models can be divided into bilateral, unilateral, and partial discectomy. Generally, partial discectomy models are used as proof-of-concept and include perforations, mimicking defects or disc thinning during early stages of disc TMD. Several partial discectomy procedures used rabbit animal models as a pilot. The earliest group compared the regenerative potential of bovine derived reconstituted collagen template to subdermal grafts (71). Contrastingly to the mandibular condyle, the utilization of natural polymers such as collagen may allow cell adhesion and migration in a primarily chondrocyte environment. Chan and colleagues employed contrast-enhanced magnetic resonance imaging (MRI) to display the degree of disc regeneration using reconstituted collagen template. Histological analysis showed dense connective tissue in the concave shaped scaffold. Though, mandibular condyle and fossa erosion, as well as joint effusion was observed. A year later, the same group took a closer look, adding earlier timepoints at 1 and 2 months (72). Similarly, the collagen scaffold showed superior rabbit disc regeneration over subdermal grafts. Using the same reconstituted collagen template a decade later, Wang and colleagues from the same group showed similar regeneration of rabbit disc a decade later. The construct enabled not only morphological similarities but expressed normal type II collagen (COL2) and type I collagen (COL1) bundles were observed after 3 months (78). In contrast to the bovine-derived collagen constructs, a decade later, Kobayashi and colleagues used porcine-derived collagen scaffolds in combination with autologous bone marrow aspirate were used in a partial discectomy (76). Injured rabbit discs did not regenerate completely after 8 weeks, but those with bone marrow aspirate performed superiorly to collagen scaffolds alone.

Brown *et al.* from Alejandro Almarza's group utilized a an ECM scaffold disc replacement, showing morphological similarities to native canine discs after 24 weeks (73). Specifically, the porcine-derived UBM construct displayed similar size and shape, in addition to that, native disc cell populations, such as the dominant COL1 were observed. Comparable results were confirmed a year later strongly concluding cell-free ECM constructs are suitable for disc replacement after bi- and unilateral discectomy (74). A decade later, Brown and colleagues created a similar cell-based ECM scaffold made of decellularized porcine small intestinal submucosa (SIS). Continuing their acellular ECM-deprived approach, the use of SIS ECM displayed similar efficacy compared to UBM ECM scaffolds. Both scaffolds protected condylar fibrocartilage deterioration and

remodeled native TMJ morphologies. However, using larger and juvenile animal models (pig), a more rapid regeneration of novel tissue formation was observed (3 months) compared to adult mongrel canines in the past (81; 82). From the Kyriacos Athanasiou group, Vapniarsky and colleagues opted to use costal chondrocytes as a scaffold free platform. Athanasiou and colleagues used a growth factor cocktail of transforming growth factor beta 1 (TGF-β1), lysyl oxidase-like 2 (LOXL2), and chondroitinase (C-ABC) to stimulate chondrocyte differentiation and extracellular matrix remodeling in a minipig model, which led to positive outcomes in disc regeneration (79).

Compared to the mandibular condyle, there are fewer biodegradable aliphatic polyesters utilized in disc bioengineering. However, polymers such as PLA, PCL, and polyglycerol sebacate (PGS) have been evaluated as TMJ disc scaffold biomaterials. For example, one group used adipose-derived stem cells (ASCs), which were sourced from the neck of the same rabbit undergoing surgery seeded on a synthetic PLA scaffold (75). The ASC seeded synthetic PLA scaffolds and encapsulated TGF-β1 displayed smoother morphologies than control scaffold. However, arthrosis and displacement were observed during both timepoints, bilaterally. One group incorporated PLGA microspheres (μS) into their scaffold design, combining them with PCL to provide a biodegradable matrix that supported MSC attachment, differentiation, and controlled release of connective tissue growth factor (CTGF) and transforming growth factor beta 3 (TGF-β3) (77). The spatiotemporal delivery system may overcome zonal cartilage regeneration in the disc (83). Similarly, Ângelo *et al*. fabricated reinforced PGS scaffolds with PCL fibers to mimic sheep discs (80). The group additionally observed other disc substitutes, that is, PCL and PEGDA and PCL alone. After 6 months, biomaterial fragmentation was observed for PEGDA/PCL and PCL groups, and condylar degeneration was present.

With the disc, utilizing autogenous or allogenic cell types may be key for the challenges of chondrogenesis and zonal regeneration. Growth factor releasing synthetic scaffolds for disc replacement offered controlled chondrocyte differentiation and extracellular matrix remodeling (77; 84). Contrastingly, cell-based ECM-derived or scaffold-free platforms may offer a suitable disc replacement with increased clinical translation (73; 74; 79; 81; 82). However, an observed disadvantage to scaffold-free approaches is implant dislocation or varied *in vivo* degradation rate, which could limit clinical applicability (75; 81; 83). Additionally, aliphatic composite scaffolds may fail to endure daily loads, resulting in fragmentation and condylar deterioration (80). The

studies revealed that platforms must support the mechanical loads and induce differentiation to overcome avascularity in the TMJ disc space.

2.7 Outcome Analyses

We compared the outcomes for both condylectomy and discectomy orthotopic models to establish a standard for *in vivo* TMJ tissue engineering evaluation. The outcomes were divided into histological, biomechanical, biochemical, imaging, quantification, and functionality **(Table 2.3-2.5)**.

All in vivo studies reported histological findings of condylar or disc tissue regeneration. Employing hematoxylin and eosin (H&E) allowed for the assessment of general tissue morphology and organization, while safranin O (SO) and immunohistochemistry (IHC) were used to detect proteoglycans and identify protein markers, respectively, indicating regenerative tissue quality. Additional staining methods, such as fast green (FO) and Alcian blue (AB) for glycosaminoglycans, Masson's trichrome (MT) for collagen, von Kossa (VK) and Alizarin red (AR) for mineralization, and acid fuchsin (AF) and toluidine blue (TB) for cellular and matrix components, provided more comprehensive insights into biochemical characteristics and structure.

Two studies included biomechanical analysis prior to implantation (19; 56), and two studies analyzed biomechanical properties at the conclusion of the various time points throughout the study (59; 81). These analyses demonstrated that some bioengineered constructs maintained comparable mechanical properties to native tissues, although variability existed depending on material composition and implantation duration. Four studies compared both native and bioengineered tissues (57; 58; 73; 79), revealing that the engineered constructs exhibited partial restoration of mechanical functions. Biochemical assays were performed to detect osteogenic and cartilaginous markers of constructs *in vitro* (55; 77; 79) and to compare native and bioengineered tissues (19; 58; 59; 66; 75; 78; 79; 81). Increased expression of osteogenic markers, such as collagen type I (COL1) and osteocalcin (OCN), was noted in constructs containing mineralized components, while cartilaginous markers like aggrecan and collagen type II (COL2) were elevated in disc-like structures. In addition, various groups employed immunolabeling of bioengineered devices to detect specific protein expression, including cluster of differentiation 3 (CD3), cluster of differentiation 4 (CD4), cluster of differentiation 31 (CD31), cluster of differentiation 68 (CD68), and smooth muscle actin (SMA), among others. (19; 58; 73; 74; 79).

Regarding mandibular condyle studies, osteo tissue quantification included total new bone formation, bone volume fraction, vascularization, and semi-quantitative assessments such as gross scoring (19; 54; 55; 57-59). Disc bioengineering quantification included vascularization, water content, glycosaminoglycan (GAG) content, collagen (COL) content, osteoarthritis or pathological scoring, body mass analysis, and multi-organ analysis (73; 74; 77; 79-82). These metrics demonstrated varying degrees of regenerative success.

Micro-computed tomography (μCT) and light microscopy were employed at the conclusion of the study (19; 55; 57; 80) or throughout (53; 54; 58; 59; 75) to assess bone formation and structural integration. Most disc tissue engineering studies opted for gross or macroscopic imaging (72-74; 76; 77; 79; 81), magnetic resonance images (MRI) (71; 81; 82), and fluorescence imaging (77) to evaluate construct morphology, positional stability, and tissue adaptation.

Functionality assessments indicated that all specimens retained function (weight gain and occlusion) after device implantation. However, implant dislocation (59; 75; 81; 82), infection (19; 59), or fragmentation (80) was observed in some studies, highlighting challenges in maintaining long-term stability and biocompatibility. These findings underscore the importance of optimizing device design and material composition to enhance *in vivo* performance.

Table 2.3: *Summary of Outcome Analyses for in vivo Tissue Engineering Studies of the TMJ.*

Authors	Species	Outcome Analyses					
Condyle		Histological	Biomechanical	Biochemical	Imaging	Quantification	Retained Function
Ueki *et al.*, 2003 (53)	Rabbit	H&E			Photomicrographs	Discal tissue, area below the discal tissue, integration, adhesion to disc	Yes
Smith *et al.*, 2007 (54)	Minipig	H&E, SO, FG			µCT	Total new bone, new bone external to implant, new bone internal to implant	Yes
El-Bialy *et al.*, 2010 (55)	Rabbits	H&E, SO, VK		COL2. OPN	µCT, photomicrographs	BV/TV, CV/TV, FV/TV	Yes
Ciocca *et al.*, 2013 (56)	Sheep	AF, TB	Compressive modulus		CT	Planned cut vs. actual post-op cut superimposition	Yes
Bhumiratana *et al.*, 2016 (58)	Minipig	H&E, IHC, VK, MP	Flexural modulus	ALP, COL1, BSP, ON, CD31	CT, µCT	Bone volume, bone volume fraction, normalized condyle height, scaffold area, surface resorption, vascular number per area	Yes
Chen *et al.*, 2020 (59)	Minipig	H&E, MP, MT, IHC	Compressive modulus, hydraulic permeability, frictional testing	BSP, OCN, OPN	CT, µCT, fluorescent tag (oxytetracycline)	Ramus and subchondral BV/TV, Tb.Th, Tb.N, Tb.Sp	Yes, n = 1 implant dislocation, n = 1 infection
Abramowicz *et al.*, 2021 (57)	Minipig	H&E, TB, SO	Compressive modulus		Radiographic, µCT, photomicrographs	Condyle height, condyle volume, and total bone volume/condyle volume	Yes
Nedrelow *et al.*, 2023 (19)	Goat	H&E, AB, IHC	Maximum stress, yield stress, flexural modulus, load transmitted %	COL2, CD4	µCT	Gross scoring: Degeneration, hypertrophy, macroscopic appearance, overall	Yes

Table 2.4: *(Continued)*

Disc							
Chan *et al.*, 2004 (71)	Rabbit	H&E			MRI		Yes
Lai *et al.*, 2005 (72)	Rabbit	H&E			Macroscopic imaging		Yes
Brown *et al.*, 2011 (73)	Canine	H&E, HP		CD31, CD68, SMA, CAL	Light microscopy, macroscopic imaging	Number of CD31+ vessels, vessel diameter, total vasculature area	Yes
Brown *et al.*, 2012 (74)	Canine	H&E, VK	Tangent modulus, peak stress, equilibrium stress, stress relaxation	CD31, CD68, SMA, COL, GAG	Light microscopy, macroscopic imaging	Water, GAG, and COL content	
Ahtiainen *et al.*, 2013 (75)	Rabbit	H&E, MT		COL1, COL2, ACAN	CBCT	qRT-PCR	Yes, implant dislocation
Kobayashi *et al.*, 2015 (76)	Rabbit	H&E, TB			Macroscopic imaging		Yes
Tarafder *et al.*, 2016 (77)	Rabbit	H&E, PR, SO, AR, AB, IHC		COL1, COL2, GAG	Macroscopic imaging, fluorescence imaging,	Collagen thickness, OARSI scoring	Yes
Wang *et al.*, 2017 (78)	Rabbit	H&E, IHC		COL1, COL2	Light microscopy		Yes
Vapniarsky *et al.*, 2018 (79)	Minipig	H&E, PR, SO, IHC	Compressive modulus, relaxation modulus, tensile modulus, ultimate tensile strength	COL, GAG, CD3, CD20, CD68	Macroscopic imaging	% Defect closed, repair tissue modulus, interface modulus, OA score, GAG %, COL %	Yes

Table 2.5: *(Continued)*

Ângelo *et al.*, 2022 (80)	Sheep	Levai-Laczkó		Biodistribution	SEM, CT	Ruminant kinematics, body mass, bone erosion,	Yes, implant fragmentation
Brown *et al.*, 2022 (81)	Pig	H&E	Tensile stress, tensile modulus, tensile SF, compressive stress, compressive modulus	DNA, COL, GAG	MRI, macroscopic imaging, light microscopy	Hydroxyproline content, GAG content, DNA content for disc and condylar cartilage	Yes, implant dislocation
Chung *et al.*, 2022 (82)	Canine	H&E, IHC		Hematology	MRI, radiographs	Pathology scoring, biochemistry reporting	Yes, implant dislocation
Jeong *et al.*, 2025 (83)	Minipig	H&E, MT, AB, PR	Compressive and tensile instantaneous moduli, relaxation moduli, coefficient of viscosity, nanoindentation	CGRP	Macroscopic imaging	Degradation	

NR, not reported; AB, alcian blue; ACAN, aggrecan; AF, acid fuchsin; ALP, alkaline phosphatase; AR, alizarin red; BSP, bone siloprotein; BV/TV, bone volume/total volume; CAL, calsequestrin; CBCT, cone beam computed tomography; CD3, cluster of differentiation 3; CD4, cluster of differentiation 4;CD20, cluster of differentiation 20; CD31, cluster of differentiation 31; CD68, cluster of differentiation 68; CGRP, calcitonin gene-related peptide; COL, collagen; COL1, type I collagen; COL2, type II collagen; COL10, type X collagen; CT, computed tomography; CV/TV, cartilage volume/tissue volume; FG, fast green; FVTV, fibrous tissue volume/tissue volume; GAG, glycosaminoglycan; H&E, hematoxylin and eosin; HP, Herovici polychrome; ICRS, International Cartilage Repair Society; IHC, immunohistochemical; MP, Movat's pentachrome; MRI, magnetic resonance imaging; MT, Masson's trichrome; µCT, microcomputed tomography; OA, osteoarthritis; OARSI, osteoarthritis research society international; OCN, osteocalcin; ON, osteonectin; OPN, osteopontin; PR, picrosirius red; qRT-PCR, quantitative Reverse Transcription Polymerase Chain Reaction; SEM, scanning electron microscopy; SF, strain at failure; SMA, smooth muscle actin; SO, safranin O; Tb.N, trabecular number; Tb.Sp, trabecular spacing; Tb.Th, trabecular thickness; TB, toluidine blue; VK, von Kossa.

2.6 Discussion

With emerging techniques in the tissue engineering field, improved clinical indications, and now-yearly TMJ bioengineering conferences, bioengineered tissue engineering applications for the TMJ are on the horizon. Here, we briefly reviewed the anatomical components of the TMJ and clinical indications for the mandibular condyle and TMJ disc. Additionally, we evaluated bioengineering scaffold biomaterials, cells, and growth factors using condylectomy and discectomy surgical procedures *in vivo*. Connecting recent approaches and outcome analyses of bioengineered tissue replacements of the mandibular condyle and disc may benefit indicated TMD and accelerate the TMJ bioengineer's goal to restore the TMJ.

In future design of preclinical models, the reporting of gender, age, species, and strain is of high importance. Especially when comparing methodology and outcome analyses such as the present report. For example, the use of adult canines compared to juvenile pigs displayed varied results using the same scaffold (73; 74; 81). These differences could be attributed to differences in the model organism or animal age, which cannot be distinguished based on the current data. Therefore, establishing standardization of reports would limit discrepancy and improve clinical translation, such as randomized, blind preclinical studies following Animal Research: Reporting of In Vivo Experiments (ARRIVE) guidelines (85-87). Appropriate controls should also be selected (i.e., bilateral vs. unilateral). Most of the condylectomy and discectomy models utilized empty contralateral control, effectively reducing the number of animals required and distinguishing the bioengineered scaffold.

These pioneering *in vivo* experiments for the mandibular condyle and disc have employed a range of animal models, reflecting the variety of species-specific anatomical and biological challenges. Canine models provide insights into the effects of different ECM scaffolds in a larger mammalian model (73; 82). Rabbits offer a more accessible and rapid model for studying stem cell-based interventions and have been known as an appropriate model for disc regeneration (52; 53; 55; 71; 75; 77). Goat models offer a larger animal model with anatomical similarities, better for long-term experiments and clinical translation after proof-of-concept studies (19). The golden standard for TMJ preclinical models, that is, the minipig, offer similar TMJ physiology, mastication, and translational potential (24; 54; 79; 88). The diverse range of animal models reflects the complexity of translating tissue engineering strategies from preclinical studies to

clinical practice (24). Animal selection should be the work of prior characterization studies *in vitro* and smaller proof-of-concept *in* vivo animal studies to address the needs end goal. Future *in vivo* studies for the mandibular condyle and disc must incorporate larger animals (dog, rabbit, goat, pig) to evaluate the stimulation of biochemical signals and mechanical forces to further elucidate the performance of engineered constructs.

For the mandibular condyle, the studies revealed that mandibular condyle constructs must mimic the mechanical loads and biochemical signals experienced in the TMJ. The use of aliphatic polyesters allowed all animal models to gain daily use over the course of the experiment. Namely, PCL, PLA, and PLGA hold the potential to serve as long-term scaffolds, able to support cells and mechanical loads sustained by the mandibular condyle and disc. Combining polymers with bioceramics or hydrogels may promote enhanced regeneration while maintaining mechanical properties for the mandibular condyle. It has been shown that creating polymer composites allows for tailoring the degradation rate, aligning bone resorption and regeneration timelines (89). Autologous cells, harvested from the iliac crest or articular cartilage may assist with osteochondral growth in the fibrous layers and promote superior function recovery. However, the inclusion of cells to tissue engineered scaffolds may decrease translation due to developmental costs and regulatory challenges (90).

For the TMJ disc, utilizing autologous cells or endogenous growth factors may be key for the challenges of chondrogenesis and zonal regeneration. To assist with proliferation and differentiation signaling, biochemical presence is usually the routine route towards enhanced regeneration, as seen by Helgeland *et al.* (13). Growth factor releasing synthetic scaffolds for disc replacement offered controlled chondrocyte differentiation and extracellular matrix remodeling in the condyle (77; 84). Contrastingly, cell-based ECM-derived platforms may offer a suitable disc replacement with increased clinical translation (73; 74; 81; 82). Bovine and ovine ECM have been used in other tissues and are approved for clinical use (91). However, a notable disadvantage of scaffold-based approaches is the potential for implant dislocation, which can comprise functional integration and long-term stability (75; 81). Addressing this challenge requires the development of fixation strategies for secure anchorage, especially for the TMJ disc, to mitigate possible displacement during load-bearing functions (92).

2.7 Conclusion

Each decade, innovative technologies become more resourceful for tissue engineering applications. For the TMJ, advanced imaging techniques such as magnetic resonance images (MRI), CT, and finite element models have continued to allow researchers to produce patient specific devices or assist in TMJ etiology for clinical use. Namely, it began with Scott Hollister and colleagues developing mandibular condylar scaffolds based on MRI and CT with additive manufacturing techniques (93). Image-based approach, in combination with fused deposition modeling or selective laser sintering, can process complex biomaterial composites for TMJ structures (19; 77). Recent reviews cover additive and subtractive manufacturing techniques for polymer biomaterials and maxillofacial applications, particularly the mandibular condyle. (61; 94; 95).

Etiology hurdles lie outside of the TMJ tissue engineering process. For trauma induced TMD or prior multiple failed surgeries, scar tissue may inhibit functional restoration using bioengineered replacements. Lack of blood supply following preclinical surgeries may lead to unsatisfactory regeneration. Therefore, it is essential that bioengineers and clinicians work closely together towards a solution for indicated patient populations and use past *in vivo* studies to carefully design regenerative implants in future studies. The authors comment on a compliment to bioengineered discs with a bioengineered condyle (32). FDA-approved TJR prostheses usually involve a metal and polymer device. Using a similar design, a potential effective solution for end-stage TMD is to bioengineer the mandibular condyle and disc together. However, a combinatory bioengineered approach should be investigated after successful restoration of individual TMJ structures. Following a systematic review of orthotopic preclinical studies, the trajectory of mandibular condyle tissue engineering is increasingly oriented toward bioactive-bioinert polymer scaffolds incorporating growth factor cocktails from the TGF superfamily, combined with patient-specific fabrication techniques. In contrast, disc tissue engineering is trending toward scaffold-free approaches utilizing ECM-derived materials, natural polymers, or cell-based constructs. Ultimately, the goal for TMJ bioengineers remains the development of regenerative, off-the-shelf replacements for both the mandibular condyle and articular disc, enabling long-term management of TMD.

This research builds upon two decades of foundational work by addressing the critical challenge of balancing bone resorption, degradation rate, and osteogenesis in tissue engineered-based constructs. By investigating the mechanical compression and degradation properties of HAp, DBM, and PCL 3D-printed biomaterials, this thesis aims to optimize scaffold formulations that balance bioactivity with structural integrity. In the pilot study, we opted for an acellular mandibular condyle device, relying inherently on the blood supply from the resected ramus and TMJ environment. Here, in addition to increased bioactivity (i.e., more HAp and DBM), we will pack the architecture of the device with a slurry of ground bone, bone marrow, and rhBMP-2. Helgeland *et al.* stated that the addition of osteogenic and chondrogenic growth factors and cells may improve TMJ tissue regeneration.

Through this work, we aim to bridge the gap between preclinical innovations and clinical translation by producing robust, bioactive scaffolds that withstand physiological loading while promoting tissue regeneration. By leveraging advanced and rapid fabrication techniques and quantitative assessment of material performance, this research contributes new insights into the development of off-the-shelf, regenerative replacements for the mandibular condyle and articular disc, paving the way for more durable and clinically viable TMJ solutions.

Chapter 3: Tuning the Mechanical Performance and Degradation Kinetics of 3D-Printed Biomaterial Composites

3.1 Abstract

Hydroxyapatite (HAp) and demineralized bone matrix (DBM) were combined with polycaprolactone (PCL) to create bioactive scaffold composites. Scaffold compositions were systematically varied to produce groups with differing ratios of HAp, DBM, and PCL to compare against previously used 20 wt% HAp/80 wt% PCL compositions. The compositions included 20 wt% HAp, 50 wt% HAp, 20 wt% DBM, 50 wt% DBM, and 20 wt% and 50 wt% HAp-DBM at a 1:3 ratio. Composites were processed using coarse (no milling), cryo-milling and roller milling, followed by filament extrusion and 3D printing into cylindrical scaffolds. Quality assessment characterization involved scanning electron microscopy (SEM)-energy-dispersive X-ray spectroscopy (EDS) for surface morphology and elemental composition analysis of processing methods, filament fabrication, and the 3D-printed scaffolds. Mechanical testing included uniaxial compression to assess compressive modulus and yield strength, while physicochemical characterization involved degradation studies monitoring mass loss in 5 M NaOH. Outcomes demonstrated that scaffolds with increased HAp content exhibited enhanced Young's (compressive) modulus, while those with DBM showed faster bulk degradation, but loss of mechanical properties over time due to increased porosity. The relationship between mass and mechanical performance loss in 5 M NaOH allows us to infer long-term performance by comparison with our ongoing 6-month study of PCL in phosphate-buffered saline (PBS), providing insights into how the optimized material may behave *in vivo*. Based on these data, an optimal and safe composition may include 50 wt% HAp in future sheep animal model. The protocols support the feasibility of fabricating composite scaffolds for mandibular condyle reconstruction assessment.

3.2 Introduction

Tissue engineering employs a diverse range of biomaterials and other bioactive ingredients to support the growth of tissues **(Figure A.1)**. For the temporomandibular joint (TMJ), aliphatic polyesters, extracellular matrix (ECM)-derived materials, and bioceramics have played a significant role in scaffold biomaterials. Aliphatic polyesters have been used extensively for various biomedical devices (96). This type of synthetic polymer possesses favorable mechanical properties, is biodegradable, and easy to process. Therefore, aliphatic polyesters are strong candidates for use in the high stress and complex TMJ mandibular condyle environment. Namely, polycaprolactone (PCL), polylactic acid (PLA), and polyglycolic acid (PGA) have been fabricated into mandibular condyle implants (19; 53; 54; 57).

A limitation of a synthetic polyester for TMJ bioengineering is their lack of bioactivity to induce bone growth. To combat this limitation, some studies have focused on harnessing the inherent regenerative potential of the biomaterial interface to promote bone formation—an approach that was also employed in our pilot study. Bioceramic materials, such as hydroxyapatite (HAp) and ECM-derived materials, that is, urinary bladder or demineralized bone matrix (DBM), have been combined with aliphatic polyester scaffolds as composites (19) or alone (55; 58; 59). Composites are made by physically combining two or more distinct materials to achieve enhanced properties. In this way, this composite platform allows the scaffold to retain favorable mechanical properties from PCL, integrate into the resected bone with HAp, or induce osteo cells with DBM, attractive for clinical translation and functional restoration of the mandibular condyle environment.

With a degradation rate of 1-2 years *in vivo*, PCL provides longer-term support than PLA and PGA, while also offering greater ductility and toughness (89). Using a faster-degrading material may lead to catastrophic failure in vivo due to premature loss of mechanical integrity before complete tissue regeneration. Therefore, this aliphatic polyester was selected as a base biomaterial for the implant. HAp was chosen due to its osteoconductive properties, attractive for scaffold integration to the resected ramus, decreased micromotion, and increased stiffness. It has been shown that PCL/HAp composites exhibit increased compressive modulus with higher weight percentage (wt%) HAp (19; 89). To enhance osteogenic outcomes further, DBM, was combined with PCL. DBM has been used extensively in oral and maxillofacial implants, offering bioactivity

for cell attachment and tissue regeneration (See Chapter 2). This osteogenic composite may recruit osteo cells, offering enhanced bone regeneration *in vivo* for the mandibular condyle **(Figure A.2)**.

The objective of this study is to establish quantitative tradeoffs between the inclusion of bioactive components in PCL composite and stiffness, yield behavior, degradation rate, and degradation mechanism. This analysis will be used to inform the selection of a biomaterial for a 3D-printed, regenerative, TMJ mandibular condyle prosthetic in a sheep model for Aim 2. Here, we tailored the mechanical and degradational properties of the composite, while assessing new formulations for PCL, HAp, and DBM. Using uniaxial compression and accelerated degradation conditions, we can determine new formulations that may be attractive for *in vivo* implants.

3.3 Materials and methods

3.3.1 Materials

All materials were purchased from Sigma-Aldrich (St. Louis, MO) unless otherwise stated.

3.3.2 Composite fabrication and filament manufacturing

Demineralized bone matrix (DBM, Allosource, Centennial, CO) powder was prepared in a large cryo-vial by cryogrinding (6875 Freezer/Mill, SPEX SamplePrep, Metuchen, NJ) for 40 minutes. The resulting DBM powder was further sieved through a 150 µm filter to collect a fine powder. Polycaprolactone (PCL, 50 kDa MW, Polysciences, Inc., Warrington, PA) with various

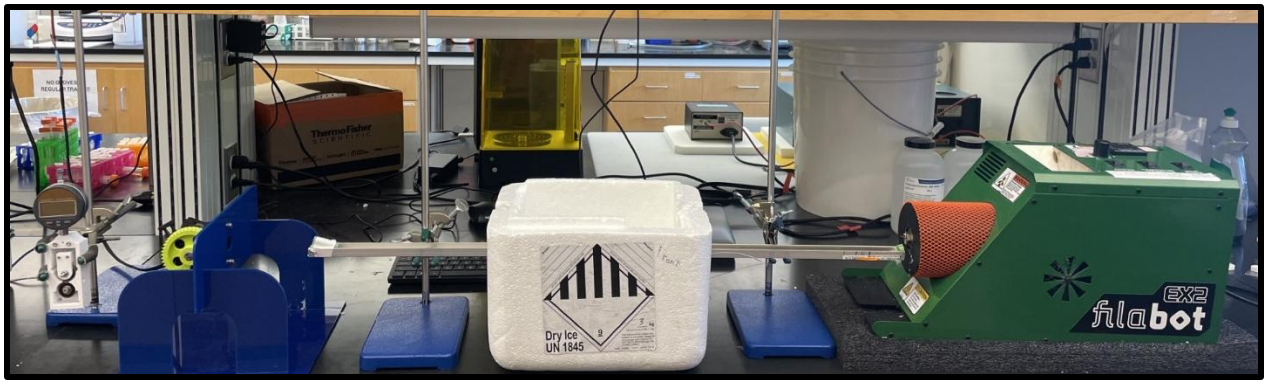

Figure 3.1: Filament fabrication setup.

Filament extrusion process for material preparation from right to left. The compositions were extruded through a cylindrical die (green/orange) and cast through a cold-water trough (silver/white). A custom puller motor assembly (blue/yellow) was used to draw the filament, with manual adjustments made to the extrusion and pulling rates to achieve the desired filament diameter.

concentrations of hydroxyapatite (HAp, Sigma-Aldrich, St. Louis, MO) and DBM were mixed by roller mill for 6 hours. The compositions were poured into a filament extruder (Filabot, Barre, VT) and extruded at 60°C through a cylindrical die. The filament melt was cast through a cold deionized (DI) water (0°C) trough and pulled by a custom puller motor assembly **(Figure 3.1)**. Manually adjusting the rate of extruder and puller allowed the formation of a filament diameter of ~1.75 mm. The resulting filament was collected on a spool and placed in a desiccator (Stat Pro, PAC, Grapevine, TX) to remove moisture and prepare for fused deposition modeling **(Figure A.3)**.

3.3.3 Fused deposition modeling

Dried filament was fed into a Cura Lulzbot TAZ 6 printer (Lulzbot, Fargo, ND) or Prusa MK4 (Prusa Research, Prague, Czech Republic) for 3D-FDM (three-dimensional fused deposition modeling) with 0.4 mm nozzle at 80°C and bed temp at 40°C. Print speeds were 5 mm $\times$ s^{-1} unless stated otherwise. Cylindrical scaffolds were designed using Meshmixer (Meshmixer, San Rafael, CA) and were 5 mm in diameter and height unless stated otherwise. Each scaffold was sliced with 100% infill and two wall layers using a rectilinear pattern creating a solid structure.

3.3.4 Scanning electron microscopy and energy dispersive x-ray spectroscopy

Macroscopic images of the 3D-printed scaffolds were captured using a Nikon DSLR camera (Nikon Americas Inc, Melville, NY) and Nikon AF-S DX Nikkor 18-55mm VR II (Nikon Americas Inc, Melville, NY) lens to document morphology and overall structure (n=1). A small ruler was included in each image as a reference for the scale bar. The camera was positioned at a fixed distance from the sample to ensure consistency between images. Images were acquired under standardized lighting conditions to minimize shadows and reflections, allowing for accurate visual comparison between scaffold groups. Non-conductive (not sputter coated) samples (n=1) were imaged by a Quattro S field-emission environmental scanning electron microscope (SEM) (FE-ESEM, Thermo Fisher Scientific, Waltham, MA) with a 20 kV acceleration voltage. Secondary electron (SE) and backscattered electron (BSE) images were used to visualize elemental distribution and topography at two magnifications (50x and 500x). Energy dispersive x-ray spectroscopy (EDS) was used to produce rectangular greyscales and color maps to visually differentiate carbon, oxygen, phosphorus, calcium, and nitrogen elements at 20 kV acceleration voltage and magnification of 50x and 500x. Raw electron count data allows the quantification of the area under curve for each elemental peak and provides weight and elemental percentage

estimates. The area under curve was calculated for each peak with a baseline of 100 employing GraphPad Prism 10.4.1 (GraphPad Software, San Diego, CA). The weight percentages were calculated based on the intensity of characteristic X-ray peaks, corrected for factors like atomic number and absorption. The atomic percentages were derived from the same X-ray data but normalized to reflect the elemental atomic ratios rather than mass fractions, indicating the relative number of atoms of a specific element compared to the total number of atoms detected.

3.3.5 Uniaxial compression testing

All specimens underwent compression in the z-direction using a uniaxial tester (TestResources, Shakopee, MN). A tare load of 10 N was applied and samples were compressed at a rate of 1 mm × min^{-1} (n=8). The compressive modulus was calculated by evaluating the slope of a linear line, fixed from 0 to 10% strain and offset by 0.2% on the x-axis. The yield strength was calculated by finding the highest stress where the linear line and stress-strain data intersect, representing the amount of stress needed to permanently deform the biomaterial.

3.3.5 Accelerated degradation

5 M sodium hydroxide (NaOH) solution was prepared by gradually mixing 40 g of NaOH pellets (Thermo Fisher Scientific, Waltham, MA) into 0.2 L of deionized water under agitation to dissolve. Solid cylindrical samples (n=80) of 5 mm height and diameter were created for PCL alone and composites: 20 wt% HAp, 20 wt% DBM, 50 wt% HAp, 50 wt% DBM, 5 wt%/15 wt% HAp/DBM and 12.5 wt%/37.5 wt% HAp/DBM. The height and diameter of all specimens was reported prior to submersion using a caliper (iGAGING, San Clemente, California). 1 mL of 5 M NaOH solution was added to a 7 mL screw-on vial under the fume hood. Individual cylindrical samples were placed into a vial and incubated at 37°C. One group (n=8) was never subjected to 5 M NaOH solution (control). Experimental groups were assayed daily for one week (n=8 per time point) and again in the second and third week for nine time points. Samples were removed and dried in a vacuum desiccator for 12 hours prior to weighing (for mass loss), volume measurement (for degradation mechanism), and mechanical testing. Mass, diameter, and height retained percentages, and compression and yield loss were calculated for each experimental specimen, relative to the untreated specimen at day 0, for each timepoint.

3.3.6 Statistical analysis

GraphPad Prism 10.4.1 (GraphPad Software, San Diego, CA) was used to perform all statistical analyses. A Student's T-test was used to compare two composite groups. A One-way analysis of variance (ANOVA) was used to compare multiple composite groups. If a significant difference was observed, Tukey's and Dunnett's post-hoc tests were used to compare significance between groups and PCL control, respectively. Individual One-way ANOVA was used for specific time points during degradation experiments. A simple non-linear regression model using one phase exponential decay was fitted along the accelerated degradation time points. All results were reported as mean ± standard deviation.

3.4 Results

3.4.1 Quality assessment of processing biomaterial particles

To achieve the overarching objective of fabricating TMJ prosthetics with different amounts of bioactive components (HAp and DBM) we sought to produce new composite filaments containing highly controlled quantities of each material component. First, we validated the composition (prior to filament fabrication and extrusion printing) using SEM-EDS **(Figure 3.2)**. SEM-EDS allows for the evaluation of material composition, based on qualitative and quantitative analysis of x-ray emission data. We employed SE and BSE, at 50x and 500x magnification, which displays a topographical image and compositional contrast, respectively. Prior to extrusion printing, each subsequent cryo-milling session decreases the overall diameter of the biomaterial particles, except for DBM and 20 wt% DBM where one cryo-mill cycle was needed. Compared to ball-milling, which serves as the control bioprocessing method used in pilot, the composition displayed less homogeneity. In the cryoground 20 wt% HAp group, brighter regions in the BSE indicate higher numbered elements, that is, calcium and phosphorus from HAp, next to darker regions, which may exhibit oxygen from PCL.

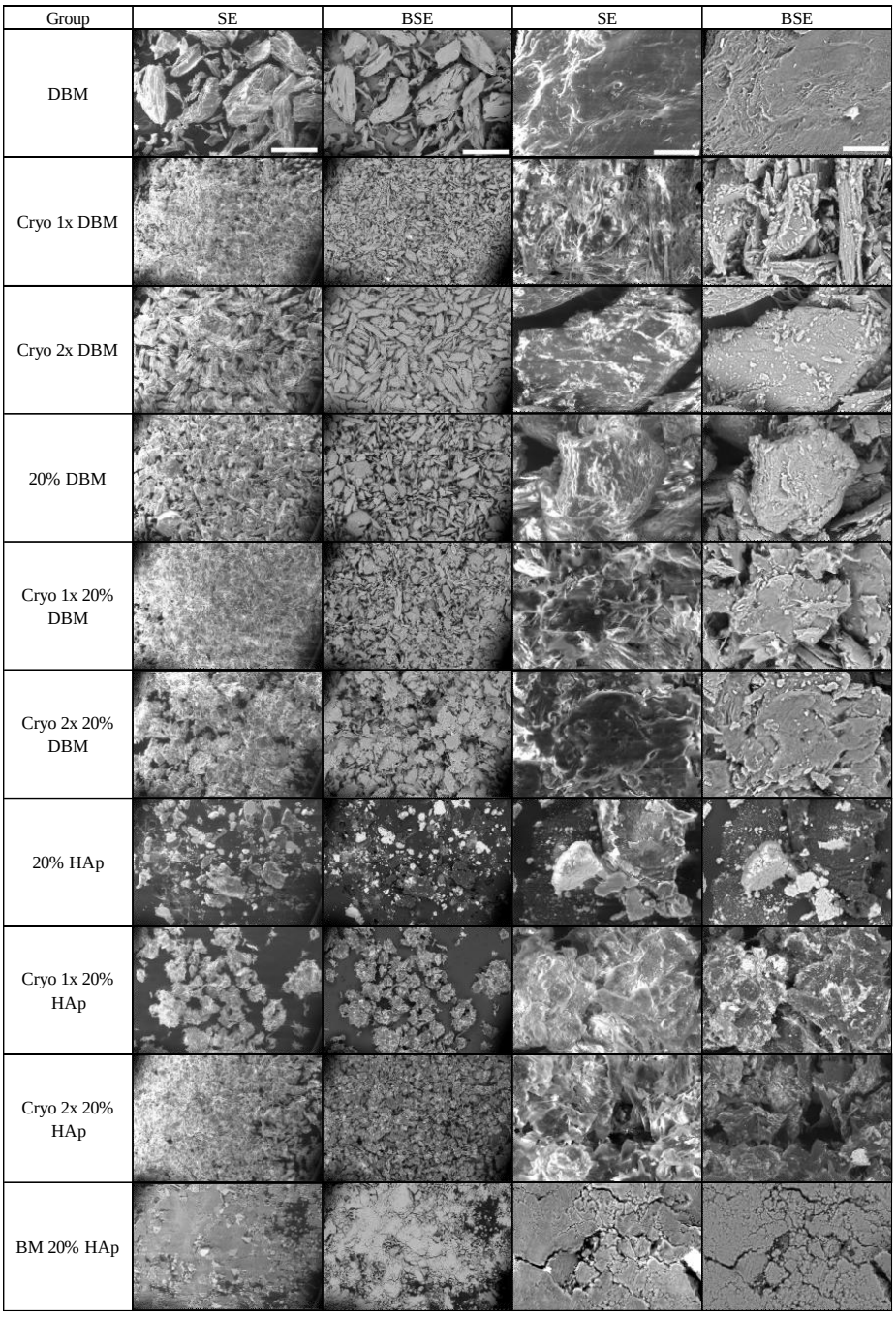

Figure 3.2: Quality assessment of biomaterial composite powders.

Cryogrinding of demineralized bone matrix (DBM), 20 wt% DBM, and 20 wt% hydroxyapatite (HAp) was performed to compare against control ball-milled 20 wt% HAp used in the pilot study. Scanning electron microscopy (SEM) images displayed that cryogrinding effectively reduced the size of larger DBM particles (>2 mm), creating a rougher topography suitable for subsequent milling and processing. However, cryogrinding of the composite materials (20 wt% HAp and DBM) may not be optimal, as the resulting particles remain larger and less homogeneous compared to the ball-milled control. Scale bar represents 1 mm and 0.1 mm for 50x and 500x magnification, respectively.

3.4.2 Quality assessment of filament fabrication

Next, we validated the bioactive components within the filament (prior to extrusion printing) using SEM-EDS **(Figure 3.3)**. Similarly, SE and BSE images were used to visualize topography and elemental distribution at 50x magnification. The groves observed are the result of the gear puller in the filament fabrication assembly. Interestingly, 20 wt% HAp and 20 wt% DBM displayed a rougher exterior compared to PCL and ball-milled 20 wt% HAp controls. The rough topography observed in the 20 wt% DBM group may be due to a drawing die, which we use to decrease the diameter of large (>1.90mm) fabricated filament to allow 3D-printing. Utilizing BSE, bright white particles, indicated as HAp, can be seen embedded in all HAp filaments, and even the combinatory 12.5 wt%/37.5 wt% HAp-DBM filament. The SEM-EDS analysis suggests that while all filaments exhibit various topographical features, the distribution of HAp and DBM particles appears relatively homogenous across the different biomaterial compositions.

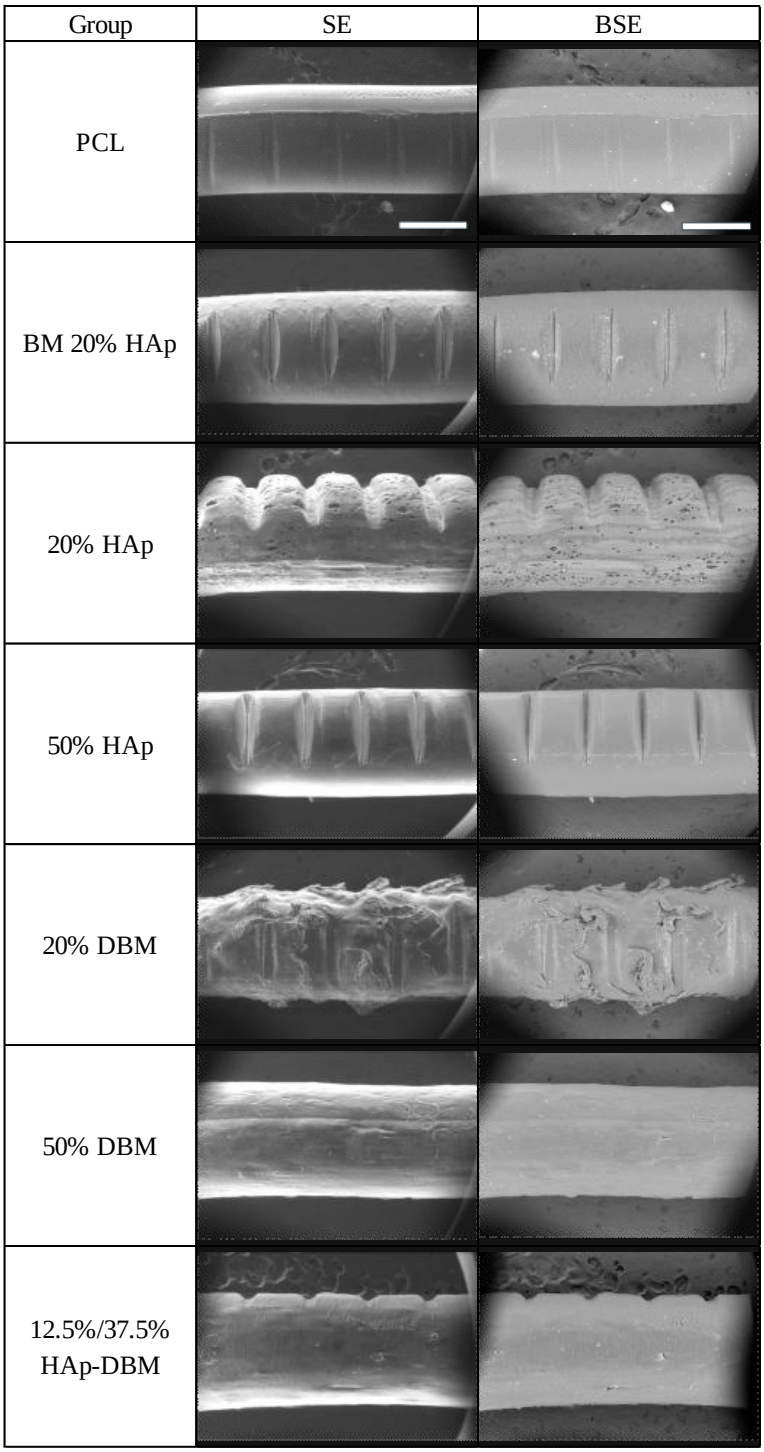

Figure 3.3: Quality assessment of filament fabrication.

Scanning electron microscopy (SEM) images of 20 and 50 wt% hydroxyapatite (HAp) and demineralized bone matrix (DBM) composites were taken at 50x magnification. Filament sections were adhered to carbon tape and assessed using secondary electron (SE) and backscattered electron (BSE) imaging. The 20 wt% groups exhibited rougher edges, with the 20 wt% DBM showing a particularly rough topography, likely due to the tapering the larger diameter (>1.90 mm) to a 3D-printable size (1.75 mm). Scale bar represents 1 mm for 50x magnification.

3.4.3 Quality assessment of 3D-FDM scaffolds

Here, we validated the bioactive compositions after extrusion printing using SEM-EDS **(Figure 3.4)**. SE and BSE images were used to visualize elemental distribution and topography at two magnifications (50x and 500x). All filaments exhibited successful printing of cylindrical specimens, with limited artifacts on the top and sides of the print. Employing SE, prints containing DBM exhibited rougher surfaces compared to HAp surfaces, which displayed a smoother exterior surface. White particles, indicated as HAp, and streak lines can be observed in the 20 wt% HAp and 50 wt% HAp. Similarly, bright wavy streaks can be observed at a higher magnification in the 50 wt% DBM and 12.5 wt%/37.5 wt % HAp-DBM groups. The SEM-EDS analysis suggests that while all 3D-printed filaments exhibit varying surface characteristics, their overall composition remains well-integrated across the different formulations.

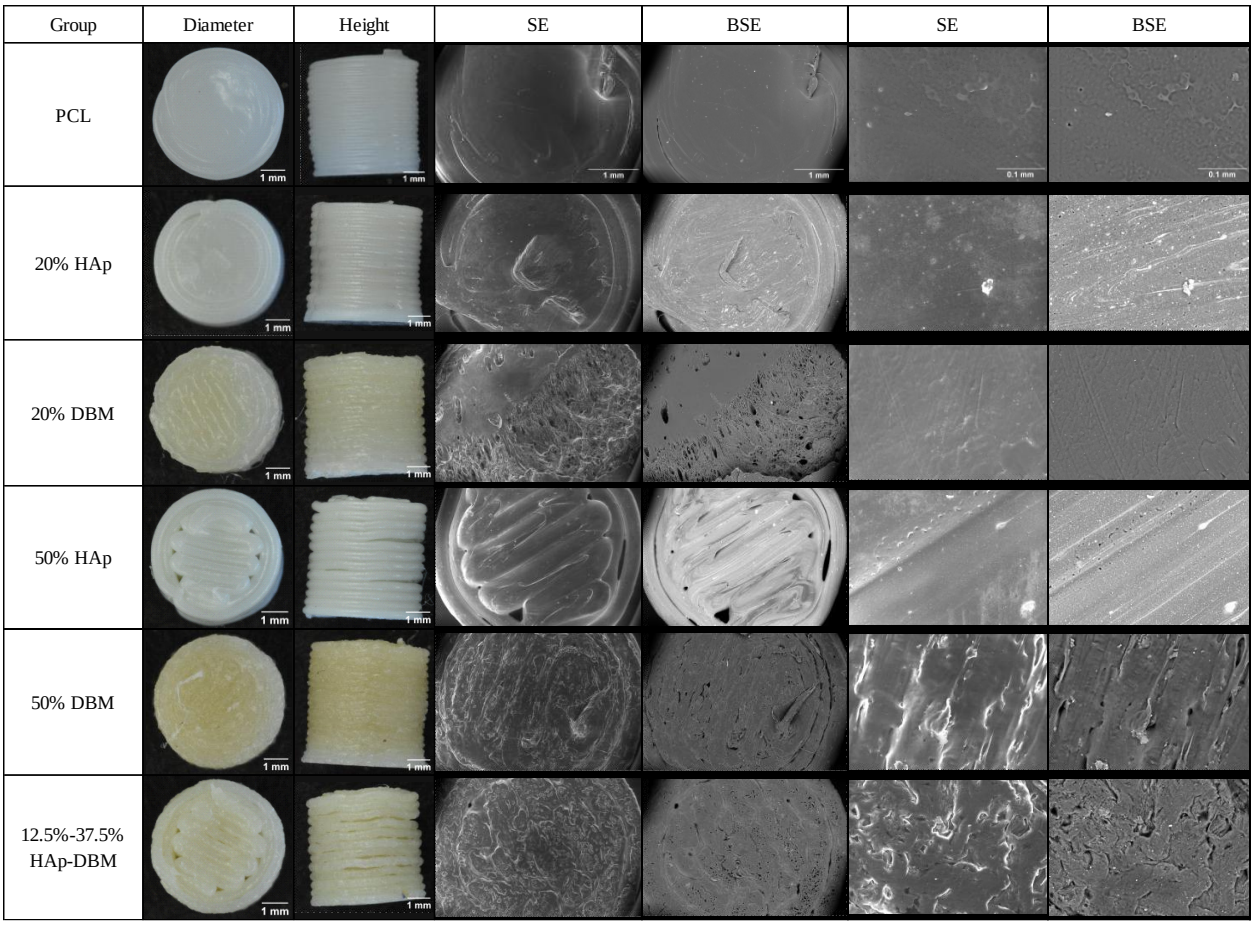

Figure 3.4: Quality assessment of 3D-FDM prints.

The various composite materials were imaged both macroscopically and microscopically at the top surface. Two magnifications, 50x and 500x, were used for secondary electron (SS) and backscattered electron (BSE) imaging. Brighter areas in the BSE images indicate increased electron scattering, which correlates with higher atomic number elements such as calcium (Ca) and phosphorus (P). Notably, as the proportions of hydroxyapatite (HAp) and demineralized bone matrix (DBM) increased, the printed structures became opaquer. Additionally, DBM-containing groups exhibited a rougher topography. Scale bar represents 1 mm and 0.1 mm for 50x and 500x magnification, respectively.

3.4.4 Elemental analysis of 3D-FDM scaffolds

Next, we used SEM-EDS analysis to qualitatively differentiate calcium (Ca), phosphorus (P), nitrogen (N), and oxygen (O), which are based on known elemental compositions of HAp (Ca, P), DBM (N, O), and PCL (O) **(Figure 3.5)**. A greyscale was used to provide a clear and effective way to visualize the intensity of x-ray signals detected from different elements. The color maps were utilized to better interpret the data by visualizing the spatial distribution of elements within each composition. Qualitatively, the bright white dots and streaks in the 20 wt% and 50 wt% HAp groups were confirmed to be higher concentrations of Ca and P, which show a denser intensity of those elements from color mapping. Lowest signal intensity of Ca and P were observed in 20 wt% and 50 wt% DBM. In the same composition groups, N was most prevalent and spatially dispersed. Similarly, O was observed to be distributed throughout the compositions. The elemental analysis suggests that the formulations retained a relatively dispersed composition with higher amounts of Ca and P in HAp compositions and higher amounts of N in DBM specimens. Interestingly N was present in all groups, possibly due to contamination in the screw extrusion hopper.

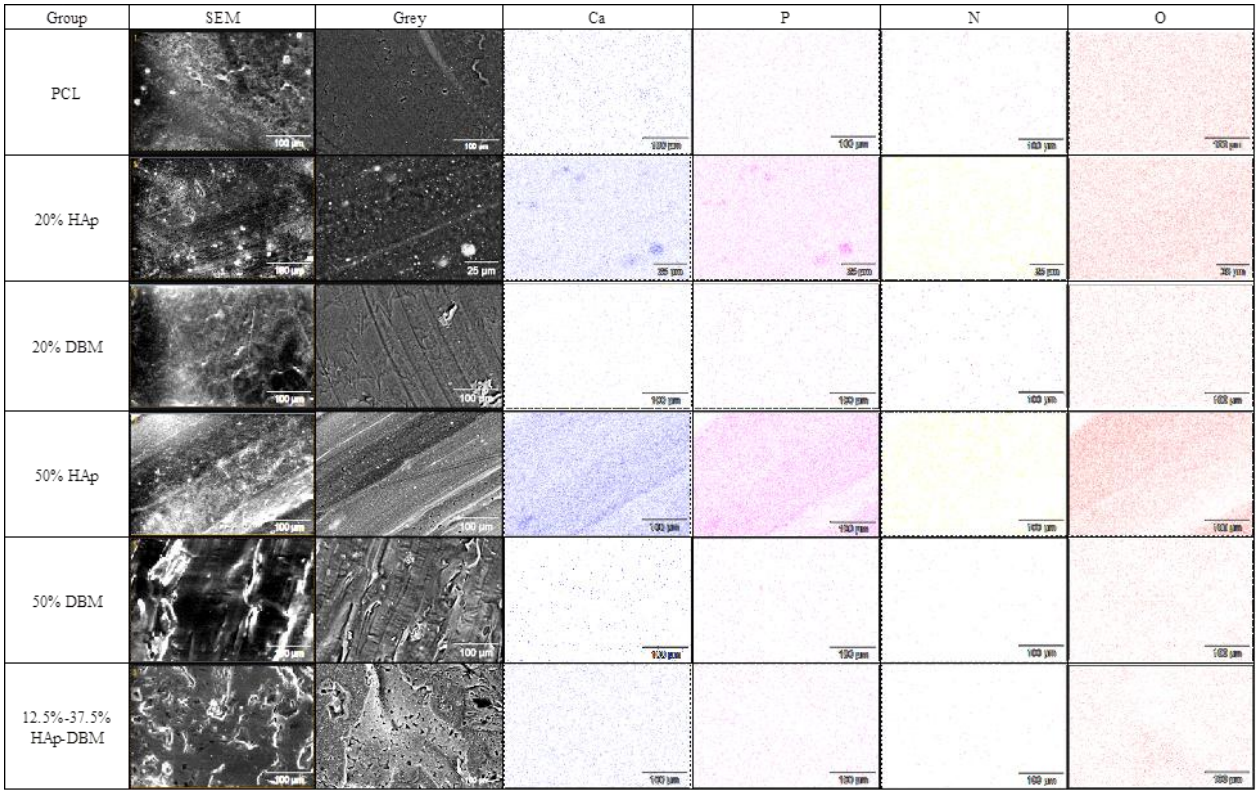

Figure 3.5: Elemental analysis of 3D-FDM prints.

Elemental analysis of the composites was performed using energy-dispersive X-ray spectroscopy (EDS). Rectangular EDS mapping was conducted on images taken at 500x magnification. Relevant elements—calcium (Ca), phosphorus (P), nitrogen (N), and oxygen (O)—were identified based on electron scatter signals. The figure displays qualitative color maps, with brighter particulates in the grayscale images indicating higher concentrations of Ca and P, particularly in the hydroxyapatite (HAp) composite groups. Low levels of N were consistently observed across all groups, likely due to contamination in the screw extrusion hopper. Scale bar represents 25 micron and 100 micron.

Finally, we evaluated each material based on expected emissions for Ca (3.69 KeV), P (2.01 keV), N (0.39 keV), O (0.52 keV), and C (0.27 keV) using SEM-EDS. Raw electrons count data, generated by the Quattro S SEM microscope, were inputted to visually analyze elemental peaks **(Figure 3.6)**. Though low amounts Ca and P were observed in the color maps for PCL alone, the electron count displayed no reading, exhibiting low intensity. Interestingly, the raw electron count displayed a high amount of N in PCL filament, which could be introduced during filament fabrication. To quantitively verify HAp in the bright white dots, a single point EDS analysis produced the Ca and P raw electron count, displaying a 4.8-fold and 3.8-fold increase compared to the 20 wt% HAp group, respectively **(Figure A.4)**. Furthermore, a 1.4-fold and 1.6-fold increase were observed for P and Ca in the 50 wt% HAp group compared to 20 wt% HAp, respectively. A 1.1-fold increase was observed for N in 50 wt% DBM compared to 20 wt% DBM. However, a 1.4-fold decrease was observed for O, comparing the same DBM groups, which may indicate higher amounts of DBM in the 50 wt% group. The reliability of the raw electron counts data remains uncertain, necessitating further investigation to confirm the fold-change trends and potential fabrication-related influences.

Group	Electron Count	Elemental Analysis
PCL	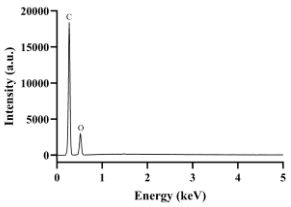	**Element** / **AUC** / **Weight %** / **Atomic %** **C** 783.4 41.0 47.1 **N** 0.0 16.1 15.9 **O** 139.5 42.8 37.0 **P** 0.0 0.0 0.0 **Ca** 0.0 0.0 0.0 **Total** **922.9** **100.0** **100.0**
20% HAP	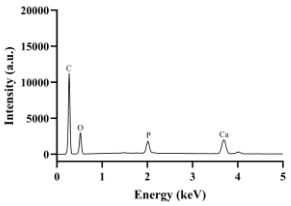	**Element** / **AUC** / **Weight %** / **Atomic %** **C** 478.9 35.0 43.6 **N** 0.0 12.0 12.9 **O** 142.5 41.7 38.9 **P** 208.1 3.5 1.7 **Ca** 200.2 7.8 2.9 **Total** **1029.7** **100.0** **100.0**
20% DBM	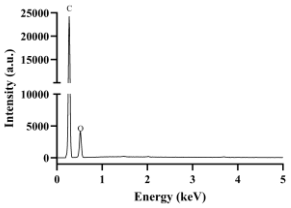	**Element** / **AUC** / **Weight %** / **Atomic %** **C** 1041.0 41.4 47.7 **N** 0.0 14.4 14.3 **O** 200.3 43.8 37.9 **P** 0.0 0.1 0.0 **Ca** 0.0 0.3 0.1 **Total** **1241.3** **100.0** **100.0**
50% HAP	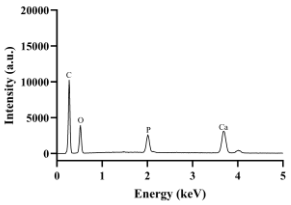	**Element** / **AUC** / **Weight %** / **Atomic %** **C** 432.9 31.1 40.2 **N** 0.0 9.8 10.9 **O** 184.9 43.7 42.4 **P** 290.7 4.6 2.3 **Ca** 319.0 10.8 4.2 **Total** **1227.5** **100.0** **100.0**
50% DBM	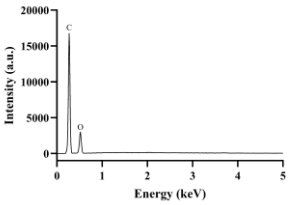	**Element** / **AUC** / **Weight %** / **Atomic %** **C** 715.6 40.1 46.3 **N** 0.0 16.0 15.8 **O** 139.5 43.7 37.8 **P** 0.0 0.1 0.0 **Ca** 0.0 0.1 0.1 **Total** **855.1** **100.0** **100.0**
12.5%/37.5% HAP-DBM	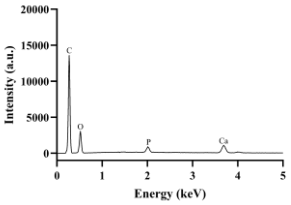	**Element** / **AUC** / **Weight %** / **Atomic %** **C** 581.0 37.9 45.4 **N** 0.0 13.6 13.9 **O** 140.1 42.8 38.5 **P** 88.1 1.7 0.8 **Ca** 94.1 4.1 1.5 **Total** **903.3** **100.0** **100.0**

Figure 3.6: EDS peaks of elemental composition.

The figure presents the raw electron count, area under the curve, weight percentage (%), and atomic % obtained from the EDS data. Fold change revealed that the 50 wt% HAp composites exhibited a 1.4- and 1.6-fold increase for calcium (Ca) and phosphorus (P) compared to the 20 wt% HAp group. Additionally, both 20 wt% and 50 wt% DBM composites demonstrated higher weight percentages of nitrogen (N) compared to the HAp groups. A 1.4-fold decrease was observed in the 50 wt% DBM group, indicating higher amount of DBM compared to 20 wt% DBM. Notably, the PCL-only group showed the highest amount of N among all tested groups, likely due to contamination in the screw extrusion hopper.

3.4.5 Modulus and yield strength of porous scaffolds

Next, we evaluated the mechanical performance of PCL composites with increased HAp content to enhance the proportion of bioactive components. This exploratory study sought to analyze how much HAp can be added to the composition and be fabricated into scaffolds. We fabricated filaments with 60-80 wt% bioactive materials but were unusable for 3D-FDM (data not shown). Moreover, the compositions were not milled (i.e., coarse). Additionally, in the interest of our previous design employing zigzag microarchitecture, porous zigzag cubes (5 mm^3) composed of PCL and 20–50 wt% HAp was fabricated and subjected to uniaxial compression testing. The compressive modulus, or Young's modulus, displayed a direct relationship compared to non-milled HAp mass ratios with PCL **(Figure 3.7A)**. The highest Young's modulus, exhibited by 30 wt% HAp, was 65.9 ± 5.38 MPa. PCL (0% HAp), 20 wt% HAp, 40 wt% HAp, and 50 wt% HAp revealed a modulus of 28.5 ± 5.97 MPa, 41.4 ± 2.51 MPa, 48.2 ± 4.80 MPa, and 60.8 ± 3.06, respectively. Compared to PCL alone, the HAp mass ratios displayed a significant difference exercising a Dunnett *post hoc.* The yield stress did not exhibit large differences between groups, however, the 30 wt% HAp group and 40 wt% HAp was significantly greater than control prints containing PCL alone **(Figure 3.7B)**. A new batch of 30 wt% HAp, denoted with an asterisk, was analyzed to test batch variability observed during the first run. The new 30 wt% HAp displayed a 60.3% and 83.6% decrease for the Young's modulus and yield stress, respectively **(Figure 3.7C, D)**. In contrast, the new 30 wt% HAp modulus did not display a significant difference compared to PCL alone. The ball milled 20 wt% HAp (BM 20 wt% HAp) mechanical performance exhibited statistically significant differences compared to non-milled 20 wt% HAp and PCL alone **(Figure 3.7E, F**). One limiting factor of this study was the absence of roller milling. Instead, we combined precisely measured quantities of each material component in a vessel and mixed them for 2 minutes. This shorter bioprocessing method, compared to the 6-hour duration typical of roller milling, resulted in inconsistent data, indicating a potential disadvantage in mechanical properties employing no milling processing **(Figure A.5)**. Furthermore, the low homogeneity of these specimens likely contributed to the variability observed in the mechanical data. Nevertheless, these coarse compositions exhibited a significant improvement over pure PCL, suggesting that increasing HAp content may lead to a higher Young's modulus.

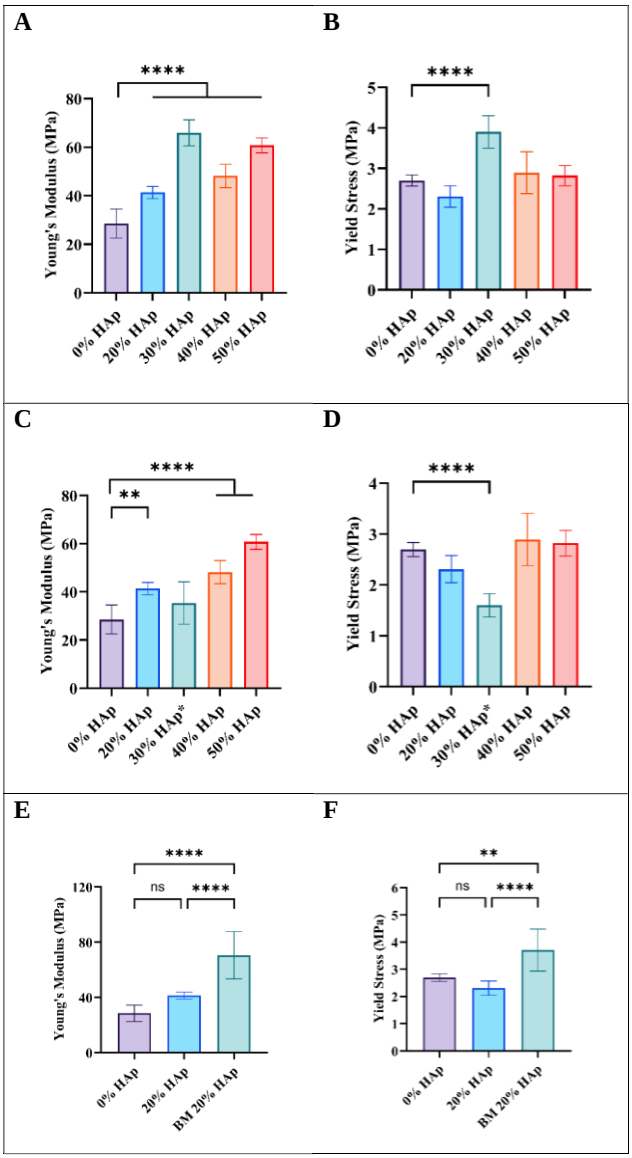

Figure 3.7: Modulus and yield stress of porous composites.

The mechanical properties of PCL and HAp composite groups (20, 30, 40, and 50 wt% HAp) were compared using a one-way ANOVA and Dunnett post hoc. 0 wt% HAp represents PCL control. ***(A)*** *Young's modulus of PCL was significantly lower than all HAp groups ($p < 0.0001$).* ***(B)*** *Yield stress analysis revealed that PCL was significantly lower than the 30 wt% HAp group only ($p < 0.0001$).* ***(C)*** *To assess batch variability, a new batch of 30 wt% HAp (30 wt% HAp*) was compared. The new batch showed no significant difference from PCL, while PCL remained significantly lower than 20 wt% PCL ($p < 0.01$), 40 wt% HAp ($p < 0.0001$), and 50 wt% HAp groups ($p < 0.0001$).* ***(D)*** *Yield strength comparisons including the new batch showed that PCL was significantly higher than the new 30 wt% HAp ($p < 0.0001$).* ***(E)*** *A comparison of Young's modulus between PCL, 20 wt% HAp, and ball-milled 20 wt% HAp (BM 20 wt% HAp) demonstrated that the ball-milled variant had significantly higher modulus than both the original 20 wt% HAp and PCL groups ($p < 0.0001$).* ***(F)*** *Yield stress analysis for the same groups showed that the ball-milled 20 wt% HAp exhibited significantly higher yield stress compared to both the original PCL ($p < 0.01$) and 20 wt% HAp ($p < 0.0001$). Error bars represent standard deviation.*

3.4.6 Anisotropic mechanical behavior of infill architecture

We then evaluated a gyroidal microarchitecture design to compare its mechanical performance against the previously tested zigzag geometry. Investigating anisotropic mechanical behavior is crucial for prosthetic devices, as the prostheses often experience multidirectional loading in the TMJ. Designing microarchitectures that account for these varied stress orientations can enhance mechanical reliability and longevity, ultimately improving clinical outcomes. Our previously used 150-micron infill was generated with infill or gyroid architecture to form an open face 10 x 10 x 10 mm^3 PCL scaffold **(Figure A.6)**. Quality assessment evaluated the mass and side length dimensions for the constructs. The gyroid group weighed significantly more at 494 ± 8.01 mg compared to 444 ± 9.15 mg for the zigzag group **(Figure 3.8A)**. The side lengths were statistically significant compared to one another for the gyroid group **(Figure 3.8B)**. For the zigzag group, the scaffold was taller than wide, having significant differences comparing the z-axis to the x- and y-axis **(Figure 3.8C)**. Utilizing PCL compositions alone, the results indicate that though

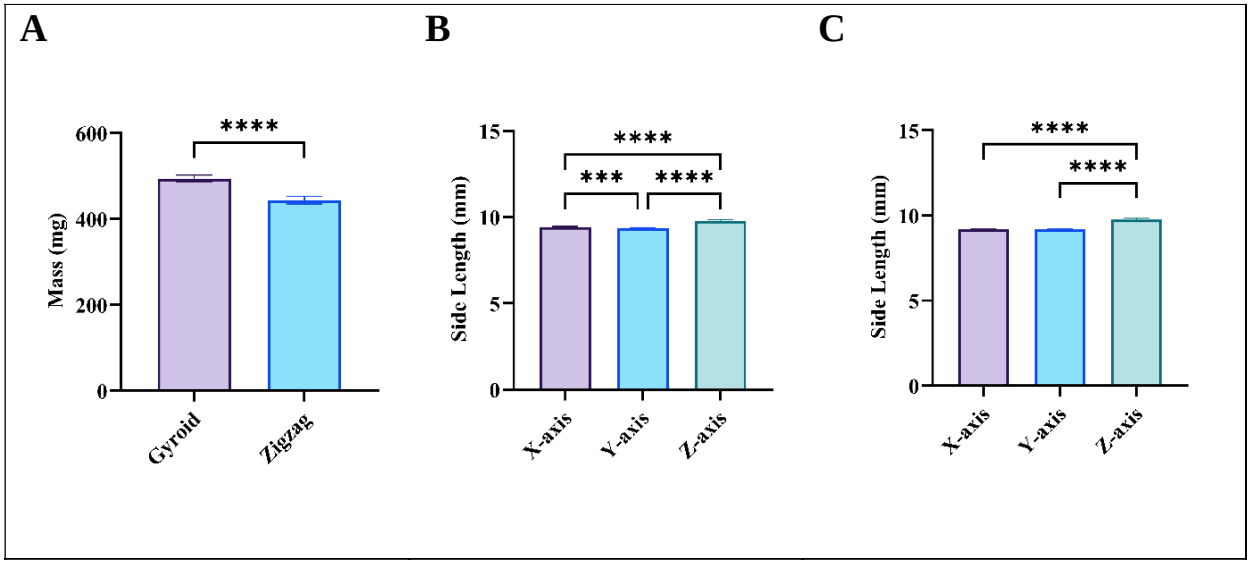

Figure 3.8: Quality assessment of gyroid and zigzag infill architectures.

Mechanical properties of gyroid and zigzag infill scaffolds were assessed to evaluate anisotropic behavior and mass consistency. ***(A)*** *Mass comparison between gyroid and zigzag architectures revealed that gyroid scaffolds had significantly higher mass than zigzag scaffolds ($p < 0.0001$).* ***(B)*** *Gyroid side length comparison along the x, y, and z axes showed significant differences between each pair of axes: x vs. y ($p < 0.001$), y vs. z ($p < 0.0001$), and x vs. z ($p < 0.0001$).* ***(C)*** *Zigzag side length comparison between axes indicated significant differences between two of the axes: y vs. z ($p < 0.0001$) and x vs. z ($p < 0.0001$).). Error bars represent standard deviation. Statistical significance was determined using one-way ANOVA followed by Tukey's post-hoc testing.*

significant differences between mass and side length were observed, the print quality remained relatively the same between both infill structures.

Here, the scaffolds underwent uniaxial compression testing in multiple orientations to evaluate mechanical performance and assess anisotropic behavior. By characterizing the anisotropic properties, we can leverage scaffold designs and fused deposition modeling to enhance durability and functional performance under physiological loading conditions. Gyroid architecture exhibited isotropic behavior with a Young's modulus of 26.8 ± 0.99 MPa, 25.7 ± 0.70 MPa, and 27.5 ± 1.60 MPa in the x-, y-, and z-axis directions **(Figure 3.9A)**. In these respective directions, the gyroid architecture exhibited a yield stress of 2.63 ± 0.05 MPa, 2.50 ± 0.13 MPa, and 2.57 ± 0.22 MPa **(Figure 3.9B)**. The gyroid mechanical performance did not display any significant differences. In contrast, the zigzag architecture displayed anisotropic properties with a Young's modulus of 33.5 ± 3.68 MPa, 32.6 ± 1.78 MPa, and 21.7 ± 6.16 MPa and yield stress of 3.07 ± 0.17 MPa, 3.08 MPa, and 1.97 ± 0.18 MPa **(Figure 3.9A, B)**. There was a statistically significant difference comparing the z-axis to the x- and y-axis. These findings suggest that gyroid architecture exhibits more uniform-isotopic properties, while the zigzag design shows anisotropic characteristics that could be advantageous in applications requiring directional strength. The anisotropic behavior in the zigzag design can be controlled by the orientation of the scaffold on the build plate of the 3D printer.

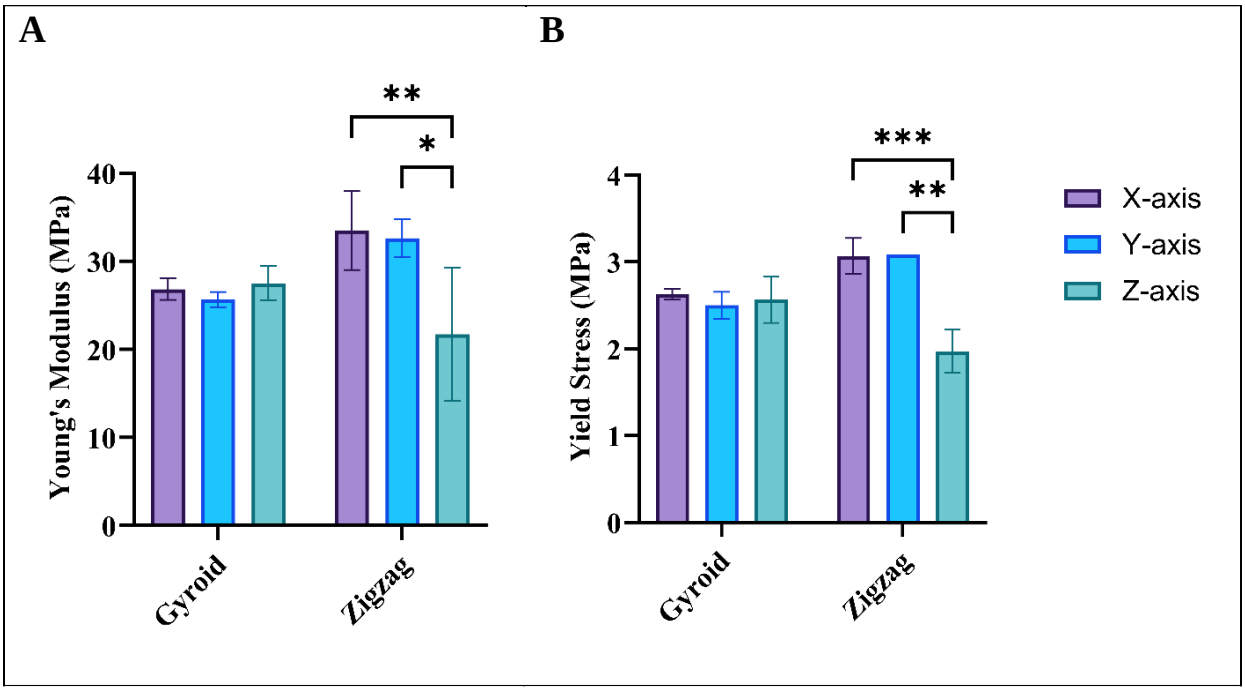

Figure 3.9: Anisotropic mechanical behavior of gyroid and zigzag infill architectures.

(A) *Young's modulus comparison for gyroid and zigzag infill architectures along the x, y, and z axes. Zigzag scaffolds exhibited anisotropic behavior, with the z-axis displaying significantly higher modulus compared to the y-axis ($p < 0.05$) and x-axis ($p < 0.01$). In contrast, gyroid scaffolds demonstrated isotropic properties, with no significant differences observed between axes.* ***(B)*** *Yield strength comparison for the same architectures and axes. Similar to modulus, zigzag scaffolds showed anisotropic characteristics, with the z-axis being significantly higher than the y-axis ($p < 0.01$) and x-axis ($p < 0.001$). Gyroid scaffolds maintained isotropic behavior, with no significant differences between axes. Error bars represent standard deviation. Statistical significance was determined using one-way ANOVA followed by Tukey's post-hoc testing.*

3.4.7 Modulus and yield strength of solid scaffolds

To further investigate the intrinsic material properties, we fabricated solid cylindrical scaffolds with a diameter and height of 5 mm after roller milling the compositions for 6 hours. These dense constructs, free from intentional porosity, enabled a more accurate assessment of the material itself. At this stage of the project, we opted for zero microarchitecture given the hollow condyle design. We introduced DBM into the compositions, including two multimaterial groups, aiming to achieve a final scaffold with both osteoconductive and osteoinductive properties. Previous research evaluated combinatory HAp and DBM at 3:1, 1:1, and 1:3 ratios, finding that the 1:3 ratio exhibited the highest bioactivity performance (data not shown). Therefore, we proceeded with this ratio at 20 and 50 wt%. Quality control measures included evaluating the mass, diameter, and height of the printed samples.

The scaffold masses for PCL, 20 wt% HAp, 50 wt% HAp, 20 wt% DBM, 50 wt% DBM, 5/15 wt% HAp-DBM, and 12.5/37.5 wt% HAp-DBM were 97.1 ± 10.4 mg, 101 ± 12.0 mg, 102 ± 10.1 mg, 76.7 ± 20.2 mg, 89.6 ± 13.0 mg, 99.3 ± 3.6 mg, and 83.9 ± 6.2 mg, respectively. The data indicate that higher DBM content in PCL composites (20 wt%, 50 wt% DBM, and 12.5/37.5 wt%

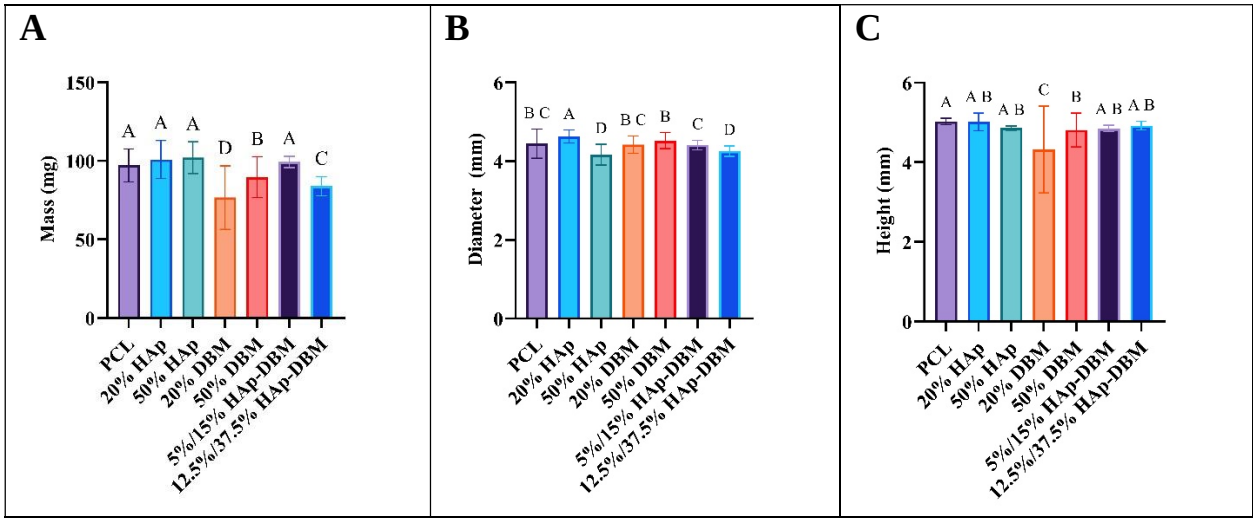

Figure 3.10: Quality assessment of roller milled 3D-FDM prints.

(A) *Mass distribution of scaffolds composed of PCL, HAp, DBM, and multimaterial composites. Higher DBM content resulted in decreased mass volume, indicating reduced print quality.* ***(B)*** *Average diameter measurements, showing statistical differences between compositions but maintaining overall dimensional consistency.* ***(C)*** *Average height measurements, displaying similar trends to diameter with slight variations between groups. Statistical comparisons were performed using one-way ANOVA followed by Tukey's post hoc test. Compact letter display is used to denote groups that are not significantly different from one another.*

HAp-DBM) decreased print quality for these milled scaffolds, as reflected by reduced mass volumes **(Figure 3.10A)**. Among the compositions tested, 20 wt% DBM exhibited the lowest mass, which was attributed to the use of half-prints at the first two timepoints. The average diameter and height followed similar trends **(Figure 3.10B, C)**. Although statistical significance between groups was observed, the diameter and height remained between 4- and 5-mm. Statistical comparisons were performed using compact letter display, where groups sharing the same letter are not significantly different from one another. These findings suggest that prolonged processing methods, such as roller milling, and the incorporation of HAp and DBM generally do not compromise print quality or dimensional accuracy.

Prior to submersion, we evaluated the Young's modulus (compressive modulus) and yield stress of the biomaterial composites (n=8). Compared to porous coarse PCL, 20 wt% HAp, and 50 wt% HAp scaffolds, the solid specimens exhibited a 3.23-fold, 1.73-fold, and 1.34-fold increase in Young's modulus, respectively **(Figure 3.11A)**. Notably, the 100 wt% PCL (0 wt% HAp) scaffolds displayed a significant increase compared to the 20 wt% HAp scaffolds. Non-significant differences were observed between 20 wt% HAp, 20 wt% DBM, 50 wt% DBM, and 12.5/37.5 wt% HAp-DBM. Similar trends were noted with the yield stress, although the yield point of the 20 wt% DBM scaffold was significantly decreased ($p < 0.05$) **(Figure 3.11B)**. These findings suggest that while the addition of bioactive materials may enhance mechanical properties compared to porous scaffolds alone, no significant trends were observed for solid scaffolds containing 20 and 50 wt% ratios. This limitation underscores the challenge of balancing processing and mechanical strength when designing composite scaffolds for load-bearing applications. Future mixtures should undergo bidirectional processing (e.g., ball milling) rather than unidirectional methods (e.g., roller milling) to further investigate the relationship between composite homogeneity and mechanical performance. However, the roller milled experimental groups were still above par for the required loads experienced by the mandibular condyle in a sheep model (10-25 MPa) (97).

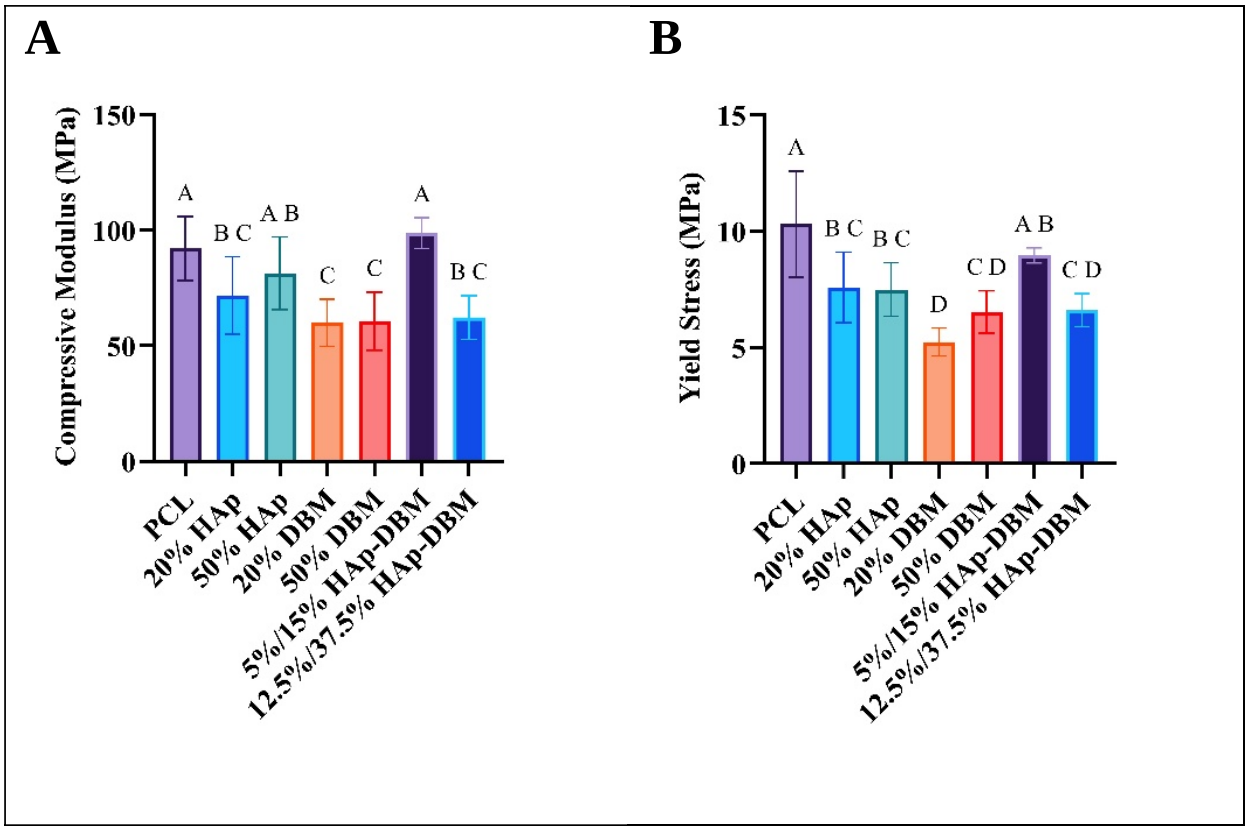

Figure 3.11: Mechanical properties of solid cylindrical scaffolds prior to submersion.

(A) *Young's modulus (compressive modulus) comparison of 20 and 50 wt% biomaterial composites, indicating improved stiffness in solid specimens. The pure PCL scaffold showed a significant increase compared to the 20 wt% HAp scaffold ($p < 0.05$).* ***(B)*** *Yield stress comparison between scaffolds, showing similar trends to Young's modulus but with a significantly decreased yield point for 20 wt% DBM ($p < 0.05$). Statistical comparisons were performed using one-way ANOVA followed by Tukey's post hoc test. Compact letter display was used to indicate groups that were significantly different from one another.*

3.4.8 Degradation kinetics of polycaprolactone-composite scaffolds

The degradation kinetics of PCL composite scaffolds are critical to their performance in load-bearing and regenerative applications. Properly balancing the degradation rate with tissue formation is essential to maintain structural integrity and ensure successful tissue integration. If the scaffold degrades too rapidly, it may lose mechanical stability before adequate tissue regeneration occurs, leading to implant failure. Conversely, slow degradation can impede tissue remodeling and limit the release of bioactive molecules. In composite scaffolds, the inclusion of bioactive materials such as HAp and DBM can further influence degradation behavior. While PCL itself degrades slowly, the incorporation of faster-degrading components may alter the composite's overall kinetics, potentially affecting both mechanical strength and bioactivity. Understanding these kinetics is therefore essential to designing scaffolds that not only provide initial support but also gradually transfer load to the newly formed tissue as the scaffold degrades.

We assessed the same solid scaffolds, PCL, 20 wt% HAp, 50 wt% HAp, 20 wt% DBM, 50 wt% DBM, 5/15 wt% HAp-DBM, and 12.5/37.5 wt% HAp-DBM for up to three weeks, with daily timepoints in the first week. During each timepoint removal, the scaffolds were extracted and dried. After 12 hours in a vacuum desiccator, the samples underwent weighing and caliper measurements to evaluate mass, diameter, and height retention relative to original measurements. A one-phase exponential decay was fitted to generate a non-linear simple regression. Expectedly, the PCL scaffolds did not degrade greatly, however, neither did the 20 wt% and 50 wt% HAp samples (**Figure 3.12)**, contrastingly to a previous experiment analyzing degradation kinetics of coarse samples (See Appendix A). A more rapid degradation was observed for DBM and HAp-DBM containing composites, reaching below 50% mass retained by day two. Two timepoints were selected, day one and day three, to sample a One-way ANOVA analysis with Tukey's *post hoc*. Here, a compact letter display is used to denote groups that are not significantly different from one another. On day one, the 50 wt% DBM mass retention percentage was significantly less compared to all groups ($p < 0.0001$) **(Figure 3.13A)**. On day three, similar trends were observed, however, other DBM groups, that is, 20 wt% DBM, 5/15 wt% HAp-DBM, and 12.5/37.5 wt% HAp-DBM displayed a significant difference to the rest of the control and HAp groups **(Figure 3.13B)**. The inclusion of DBM biomaterials accelerated the degradation of the scaffolds compared to HAp, and more notably with the higher 50 wt% ratio. Diameter and height retention data indicate that the

scaffolds experience bulk degradation as well as observation of generated porosity (data not shown) **(Figure 3.14A, B)**. Measurements were taken at each timepoint, with diameter and height measurements ceasing once the samples had degraded sufficiently. Mass retention in the latter timepoints increased likely due to possible NaOH precipitate deposition or drying inconsistencies from day fourteen to twenty-one.

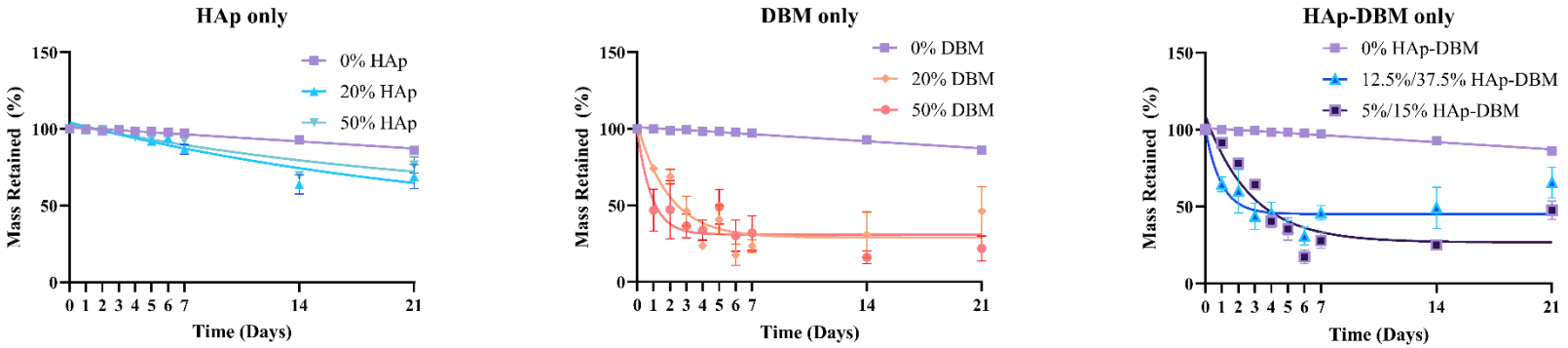

Figure 3.12: Mass retention of solid PCL-composite scaffolds over three weeks.

Scaffolds composed of PCL (0%), 20 wt% HAp, 50 wt% HAp, 20 wt% DBM, 50 wt% DBM, 5/15 wt% HAp-DBM, and 12.5/37.5 wt% HAp-DBM were assessed for mass retention at daily timepoints during the first week and weekly thereafter up to three weeks. Scaffolds were extracted, dried in a vacuum desiccator for 12 hours, and measured at each timepoint. A one phase exponential decay simple regression curve was fitted for each composite group.

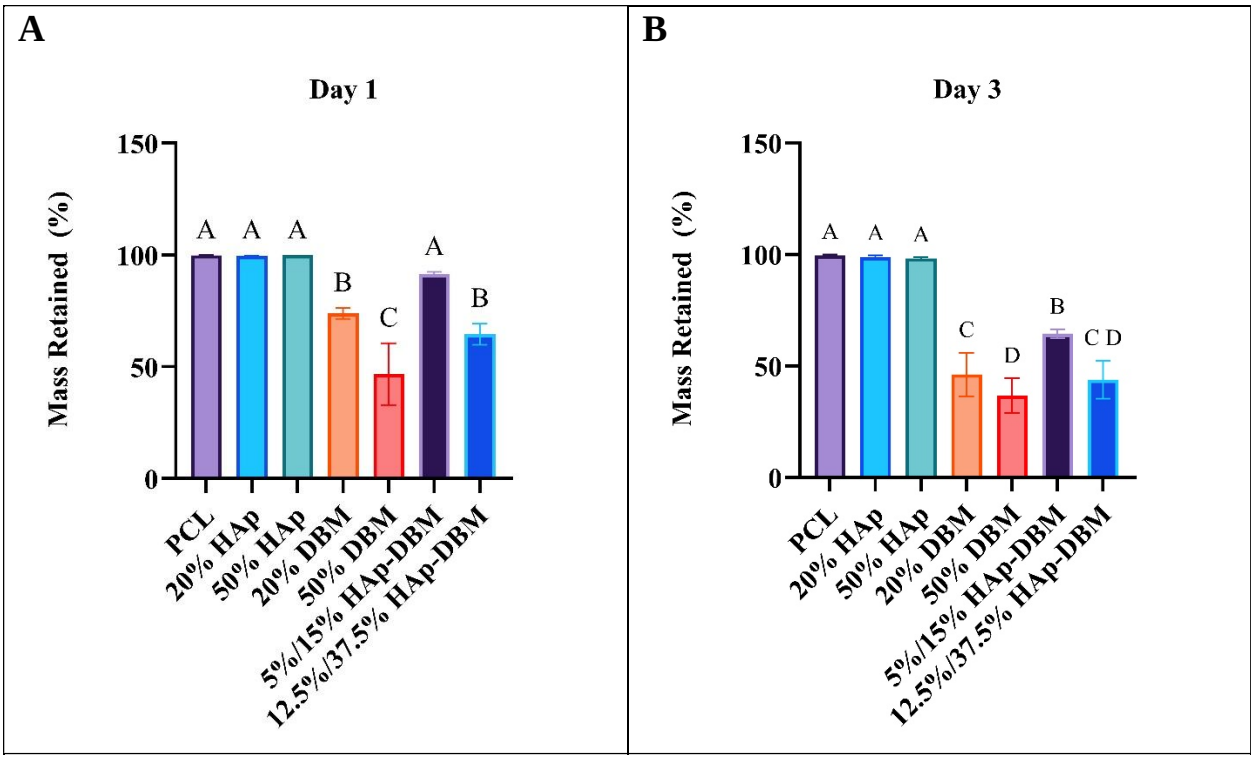

Figure 3.13: Mass retention of solid PCL-composite scaffolds at day one and three.

(A) *Mass retention for the 50 wt% DBM scaffolds was significantly lower on day one compared to all other groups ($p < 0.0001$).* ***(B)*** *On day three, similar trends were observed, with other DBM groups (20 wt% DBM, 5/15 wt% HAp-DBM, and 12.5/37.5 wt% HAp-DBM) also displaying significant differences relative to the control and HAp groups. The inclusion of DBM accelerated degradation, with the 50 wt% DBM scaffolds showing the most significant decrease in mass retention. Statistical analysis was performed using one-way ANOVA followed by Tukey's post hoc test, and compact letter display was used to indicate groups that were significantly different from one another.*

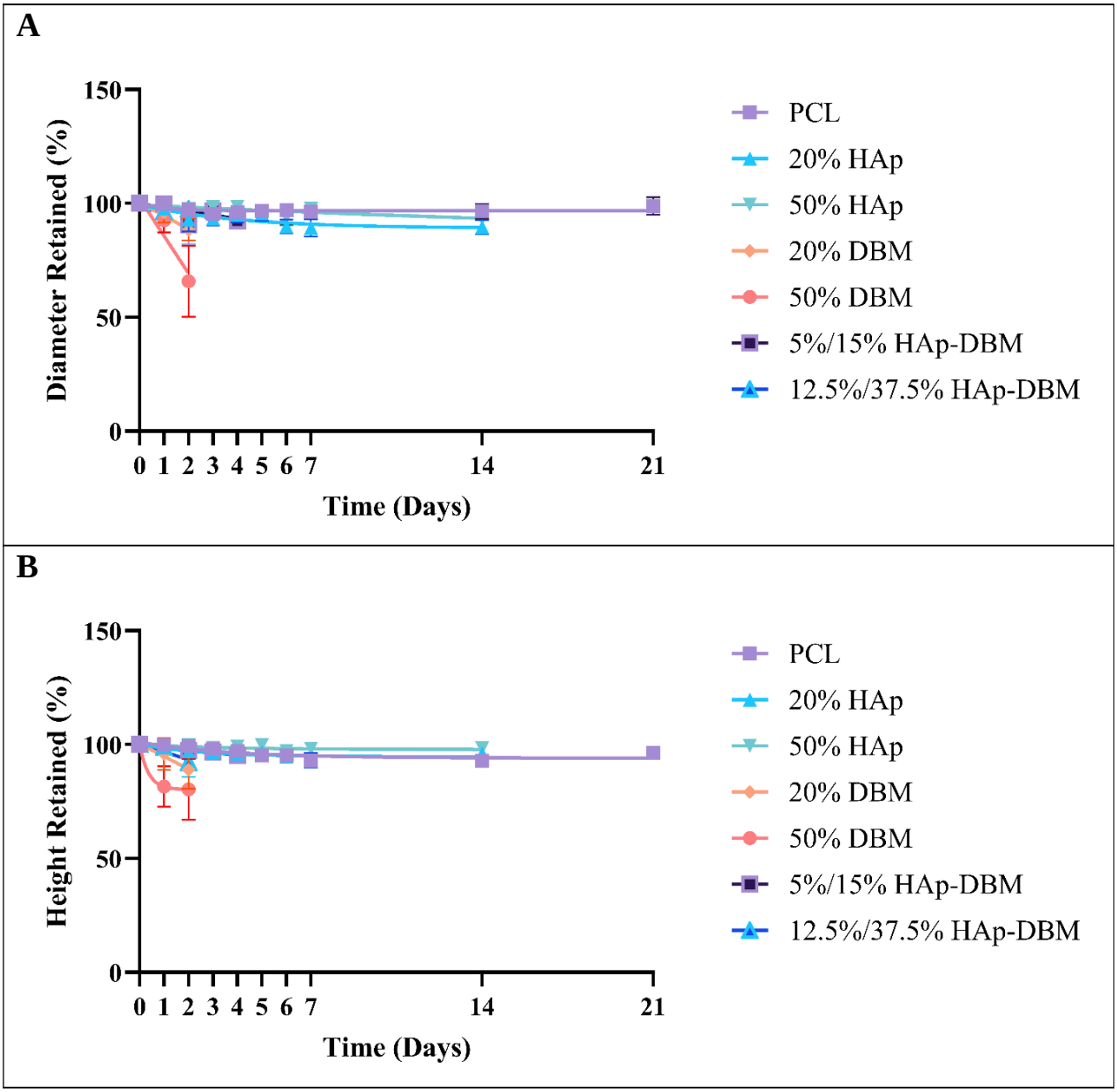

Figure 3.14: Diameter and height retention of solid PCL-composite scaffolds over three weeks.

(A) *Diameter retention of scaffolds composed of PCL, 20 wt% HAp, 50 wt% HAp, 20 wt% DBM, 50 wt% DBM, 5/15 wt% HAp-DBM, and 12.5/37.5 wt% HAp-DBM over three weeks of degradation. Measurements were taken at each timepoint, with diameter measurements ceasing once the samples had degraded sufficiently. The 20 wt% and 50 wt% DBM groups stopped on day 2 due to significant degradation.* ***(B)*** *Height retention of the same scaffolds over time. Similar to diameter measurements, height measurements were discontinued once degradation reached a critical point, with the 20 wt% and 50 wt% DBM groups ceasing on day 2. The height and diameter became unmeasurable after significant degradation had occurred, that is, day two for DBM containing groups, and day twenty-one for HAp containing groups.*

3.4.9 Mechanical property loss of polycaprolactone composite scaffolds

After drying and measurements of diameter, height and mass, we evaluated the Young's modulus (compressive modulus) and yield stress of the biomaterial composites. The specimens underwent uniaxial compression to assess the loss of Young's modulus and yield stress under accelerated conditions, simulating the mechanical challenges scaffolds face during degradation in vivo. This testing is essential for understanding how the mechanical properties evolve as the scaffold degrades, providing insights into the relationship between porosity (i.e., bulk degradation) and mechanical performance. Monitoring these changes allows for the optimization of scaffold design, ensuring that the material retains sufficient strength to support tissue growth while gradually transferring load to the regenerating tissue. Additionally, the data can help predict the functional lifespan of scaffolds, ensuring that they maintain structural integrity during the critical stages of tissue formation and remodeling.

Composites containing only DBM exhibited a steep decrease in mechanical performance during the early time points, particularly for 12.5/37.5 wt% HAp-DBM **(Figure 3.15)**. Interestingly, the PCL control and 20 wt% and 50 wt% HAp groups showed an increase in compressive modulus, likely due to NaOH etching, which has shown to enhance the Young's modulus in previous research (data not shown). However, as the samples reached later points in the first week (i.e, day five and seven), a decline in mechanical performance was observed for the 20 wt% and 50 wt% HAp composites until day twenty-one. To statistically compare these results, a One-way ANOVA was applied to selected time points, specifically day one and day three. On day one, the DBM-only groups and the 5/15 wt% HAp-DBM composites showed statistically significant differences compared to the PCL and HAp-only groups, indicating that higher DBM ratios, or DBM alone, contributed to a loss of mechanical integrity **(Figure 3.16A)**. By day three, the 5/15 wt% HAp-DBM composite exhibited a decrease in modulus compared to day one. Additionally, the HAp-only groups did not show significant differences from the PCL group, indicating a slow degradation rate, which was also observed in the pilot study **(Figure 3.16B)**. Similar trends were seen for yield stress **(Figure 3.17)**, except for the 5/15 wt% HAp-DBM composite, which showed no statistical significance compared to the 20 wt% HAp group on day one **(Figure 3.18A)**. By day three, the yield stress of the PCL and HAp-only groups remained non-

significant, while all other groups containing DBM or multimaterial showed significantly reduced yield stress **(Figure 3.18B)**.

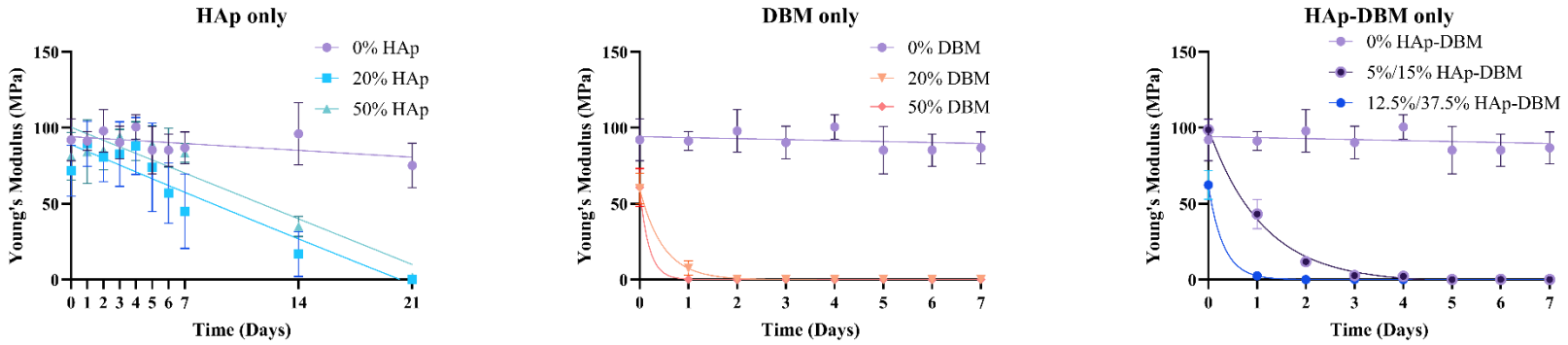

Figure 3.15: Young's modulus loss of solid PCL-composite scaffolds over three weeks.

Compressive modulus of PCL (0%), 20 wt% HAp, 50 wt% HAp, 20 wt% DBM, 50 wt% DBM, 5/15 wt% HAp-DBM, and 12.5/37.5 wt% HAp-DBM scaffolds over three weeks. A significant decrease in modulus was observed for the DBM-only and 12.5/37.5 wt% HAp-DBM groups during the early time points. PCL and HAp groups showed an increase in compressive modulus due to NaOH etching, with a subsequent decrease in the 20 wt% and 50 wt% HAp groups by day five. A one phase exponential decay simple regression curve was fitted for each composite group.

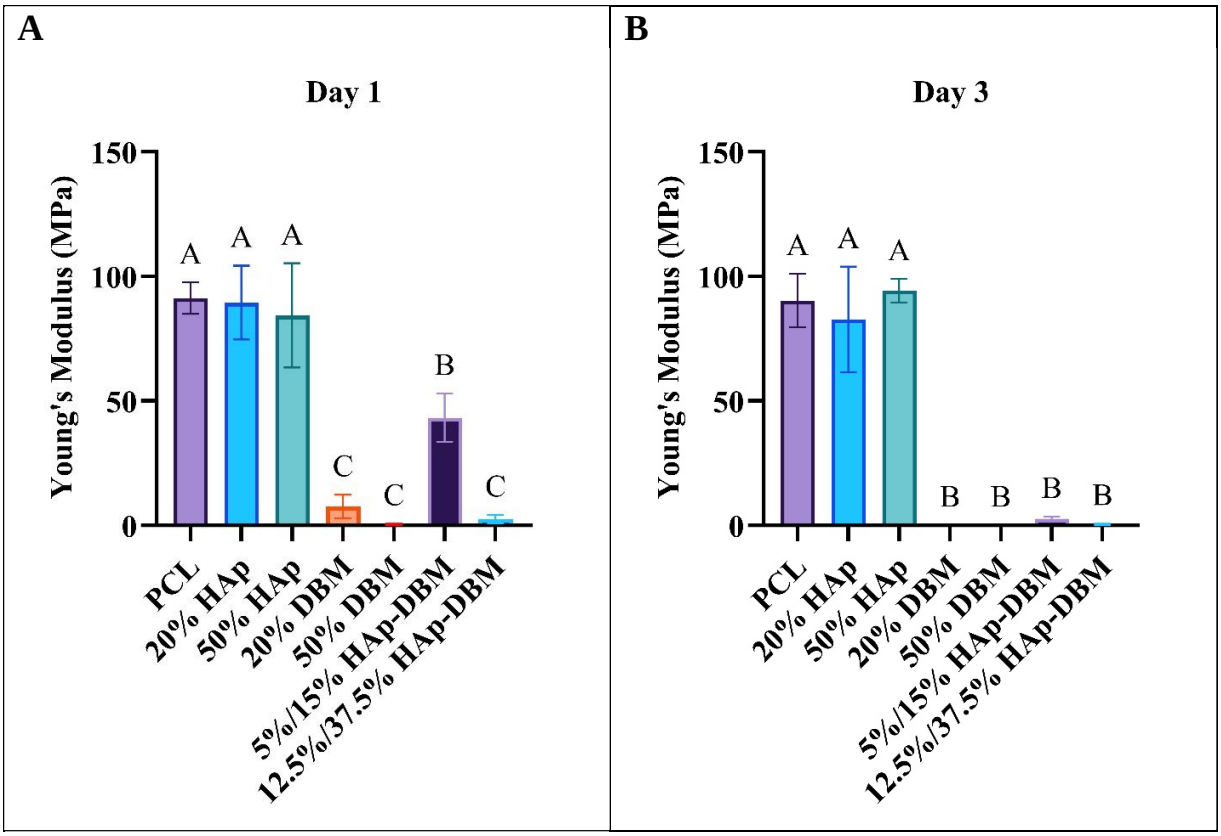

Figure 3.16: Young's modulus of solid PCL-composite scaffolds at day one and three.

(A) *Statistical comparison of compressive modulus at day one. The DBM-only and 5/15 wt% HAp-DBM groups showed significant differences compared to PCL and HAp-only groups ($p < 0.0001$), indicating that higher DBM ratios or DBM alone contributed to loss of mechanical integrity.* ***(B)*** *Compressive modulus at day three, showing a significant decrease in the 5/15 wt% HAp-DBM group compared to day one ($p < 0.0001$), with HAp groups displaying slow degradation and no significant difference compared to PCL. Statistical analysis was performed using one-way ANOVA with Tukey's post hoc test, and compact letter display was used to indicate groups that were significantly different from one another.*

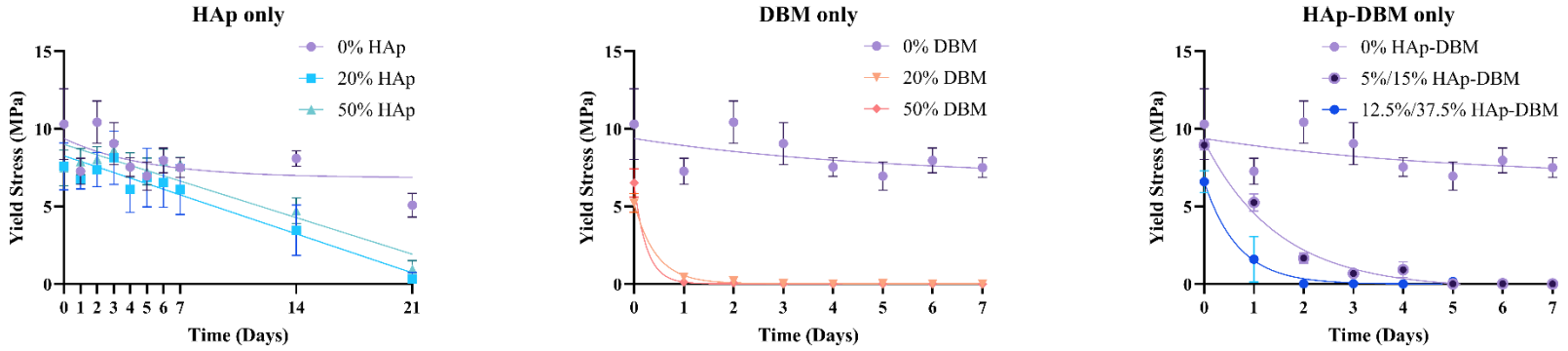

Figure 3.17: Yield stress loss of solid PCL-composite scaffolds over three weeks.

Yield stress loss of PCL, 20 wt% HAp, 50 wt% HAp, 20 wt% DBM, 50 wt% DBM, 5/15 wt% HAp-DBM, and 12.5/37.5 wt% HAp-DBM scaffolds over three weeks. A significant decrease in yield stress was observed for the DBM-only and 12.5/37.5 wt% HAp-DBM groups during the early time points. PCL and HAp groups showed an increase in yield stress likely due to NaOH etching, with a subsequent decrease in the 20 wt% and 50 wt% HAp groups by day five and until day twenty-one. A one phase exponential decay simple regression curve was fitted for each composite group.

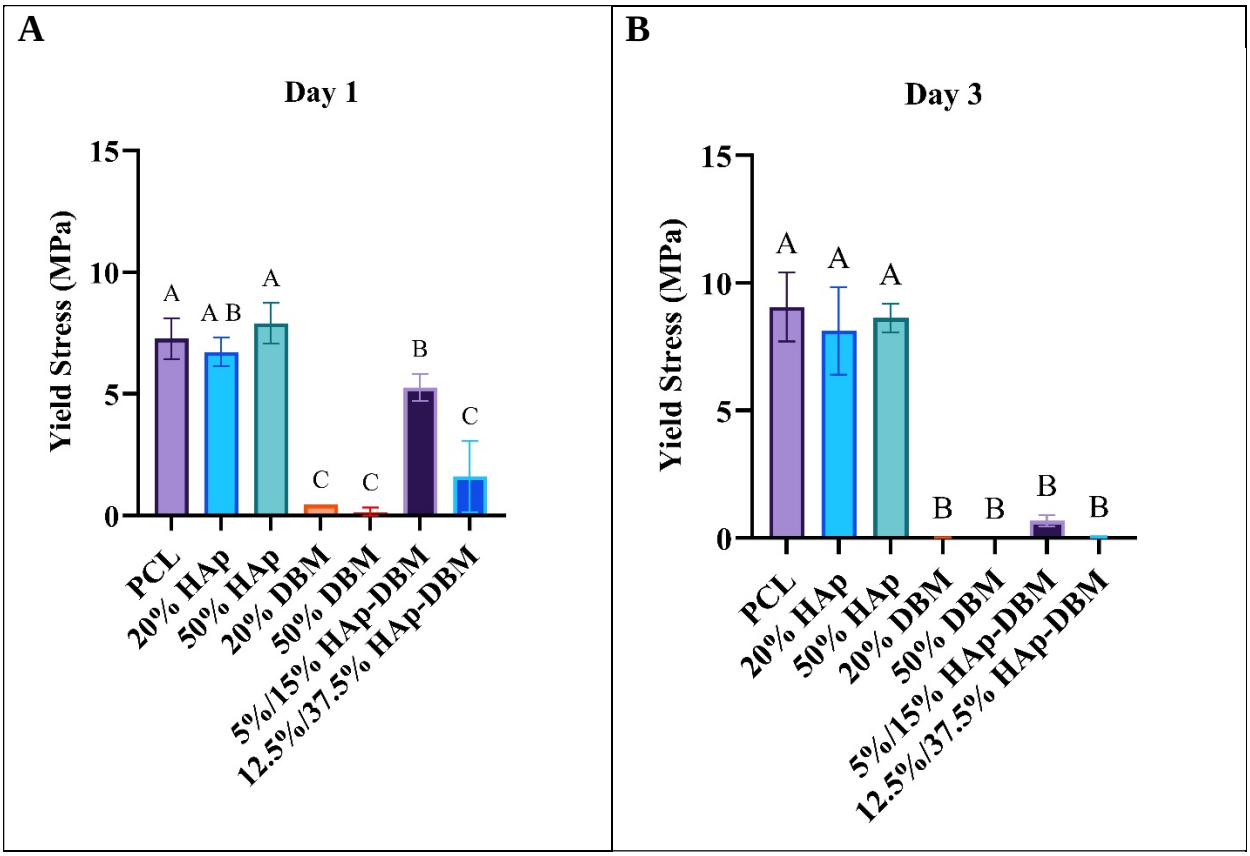

Figure 3.18: Yield stress of solid PCL-composite scaffolds at day one and three.

(A) *Yield stress comparison at day one, showing significant decreases in the yield stress of DBM-containing scaffolds compared to PCL and HAp-only groups ($p < 0.0001$). Similar trends were observed to compressive modulus, except for the 5/15 wt% HAp-DBM group showing no significant difference compared to the 20 wt% HAp group.* ***(B)*** *Yield stress at day three, indicating no significant change in PCL and HAp-only groups, while all DBM or multimaterial groups showed a significant decrease in yield stress ($p < 0.0001$). Statistical analysis was performed using one-way ANOVA with Tukey's post hoc test.*

3.5 Discussion

End-stage surgical interventions of the mandibular condyle pose a significant hurdle, especially for pediatrics, metal hypoallergenic patients, and those with multiple failed surgeries. Other indications include unsalvageable condylar trauma and hyperplasia (32). To overcome these limitations, bioresorbable materials, such as aliphatic polyesters and ECM-derived materials have been used extensively as tissue engineering scaffolds (13). In the current study, we display the feasibility of fabricating PCL, HAp, and DBM composite scaffolds to tailor the mechanical and physiochemical properties.

The first step towards the development of full mandibular condylar prostheses is preprocessing bioactive ingredients. Unmilled (i.e., coarse) compositions, that is, shaken in a vessel for 2 minutes, displayed rough topography and poor uniformity. The use of cryogrinding displayed a reduction in composite particle size, yet a rougher topography and low homogeneity. In our methodology, we use cryogrinding to process the larger 2 mm DBM particle sizes. However, the results indicate that cryogrinding is not effective for homogenizing compositions together. The particle size is one of many parameters effecting the performance and properties of fused deposition filament (98). Other preprocessing procedures include ball milling, which was employed in the pilot. Planetarium ball milling has been concluded to grind particles to the nanoscale, influencing microstructure and homogeneity (99). Using SEM, our positive control, ball-milled 20 wt% HAp displayed the smallest particle sizes compared to cryoground samples, qualitatively. Due to the unavailability of ball milling over the course of the project, roller milling was utilized as an alternative to further refine composite particle size to near nanometer and micron size. This technique involves tumbling particles under unidirectional rotation to enhance homogeneity while minimizing particle size by ceramic balls. While roller milling did not achieve the nanoscale refinement of ball milling, it offered an improved balance of particle size reduction and material integrity, compared to cryoground or coarse compositions. Therefore, the results suggest that for the development of 3D-printed implants for tissue engineering, material compositions should undergo ball milling to minimize particle size and maximize elemental uniformity and mechanical performance. Though coarse HAp composites still display enhanced performance compared to PCL alone, variability was observed in these processed materials (i.e., 30 wt% HAp).

Following milling, the powder must undergo screw extrusion to produce 3D-FDM usable filament. PCL pellets (i.e., purge) were used to clear and remove any contamination from the hopper and heated screw extruder unit. To retain bioactivity of PCL-composites, a temperature of 60℃ was used, where exposure times were less than 3 minutes. During extrusion, the melt is quenched in an iced water trough, where after the filament was dried in a vacuum desiccator to remove excess moisture. The diameter tolerance is solely impacted by the puller and extruder rate of speed (data not shown). Our results suggested that filament fabrication performance is dependent on milling method and the rates of the extruder and puller. Additionally, SEM-EDS analysis indicated that the distribution of HAp and DBM particles appeared relatively homogenous across the different biomaterial compositions.

The last step includes any commercially available 3D-printer. Here, we employed two printers, a LulzBot Edition TAZ 6 and a Prusa MK4. Both displayed the ability to 3D-print experimental samples with various settings. However, significant jamming issues were observed in the heat break lumen or turning gear with filament diameters above 1.80 mm for the TAZ 6. The larger MK4 gear allowed better gripping of most composites compared to smaller gears observed in other 3D-printers. Additionally, fabricated filaments with 60-80 wt% bioactive materials were unusable for 3D-FDM (data not shown). In this experimental study, our results suggest that 50 wt% PCL composite filaments can be 3D-printed at a range of 1.60-1.80 mm, however, non-uniform filaments may lead to varied material flow rates, which may affect mass, height, or diameter, particularly for DBM composites. Previous research determined that at 80℃ nozzle temperature and a print speed of 60 $mm \times s^{-1}$ maximizes the print quality, which was used for this study.

In the interest of higher amounts of bioactive materials, a range of 0-50 wt% HAp compositional experimental prints were evaluated mechanically. Following similar designs to the pilot prosthesis, these scaffolds were porous and retained the same infill geometry and void space. Conclusive to previous results, the inclusion of bioactive materials enhanced the compressive modulus. Similar trends were observed with the yield strength, or the point where the material deforms plastically. However, coarse material compositions displayed differences between filament fabrication batches. A retest of 30 wt% HAp displayed a nonsignificant modulus compared to control, causing concerns for performance variability without ball milling. Further

comparison between coarse and ball milled prints displayed a significant difference between Young's moduli and yield strength, indicating that ball milling may increase mechanical performance.

We further investigated other scaffold architectures to compare against zigzag porous features. Gyroid is an irregular geometry which mimics the zigzag orientation, but may be superior towards bone regeneration and strength as it resembles bone trabeculae (100). Our results indicate that zigzag orientation retained a higher Young's modulus compared to gyroid structures. However, gyroid architecture exhibited isotropic properties, which means each axis under compression performs the same. In contrast, the zigzag geometry displayed anisotropic properties, which indicate the mechanical performance is dependent on the axis. The x- and y-axes were superior for both compressive modulus and yield strength. Our results reinforce the orientation of the prosthesis on the build plate used in pilot study. When printing the architecture in the z-axis, the scaffold is vertical, while printing the scaffold horizontally, the infill will be compressed in the x- and y-axes **(Figure 3.19)**. Our results indicate that prints should be printed horizontally, to maximize performance and lessen failures during printing from support material.

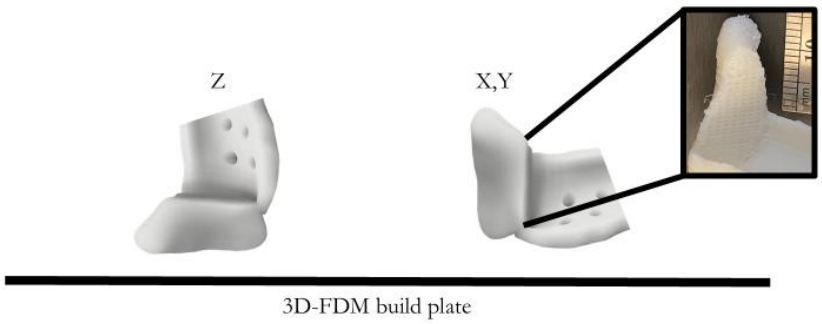

Figure 3.19: Infill performance dependent of print orientation on 3D-FDM build plate.

The zigzag infill pattern exhibits anisotropic behavior, with a stronger modulus observed along the x- and y-axis compared to the z-axis. This directional strength arises from the layered nature of fused deposition modeling, where interlayer bonding in the z-direction is weaker than along the x- and y-plane. The choice of print orientation significantly impacts the mechanical performance of the final prosthesis, influencing load-bearing capacity and structural integrity for use in Aim 2.

Our pilot study results observed successful regeneration of osteochondral structures in the mandibular condyle by the implantation of an anatomically accurate PCL and HAp implant. Furthermore, the implant was able to maintain the load-bearing environment throughout the study.

However, there was a dissatisfaction with osteogenesis in correlation with the non-degraded biomaterial. Non-localized bone ingrowth was observed exterior to the infill microarchitecture. The acellular implant design relied solely on the osteoconductive capabilities of HAp, which has the potential to aid in attachment and stability at the ramus interface. To enhance regenerative capabilities in the following preclinical model, DBM was introduced to the PCL composites. The demineralization process of DBM removes the extracellular matrix and other mineral content but preserves collagen and bone morphogenetic proteins, which may stimulate differentiation and encourage bone formation.

After assessing the porous infill, solid scaffolds underwent mechanical and physiochemical evaluation to better understand the biomaterial's properties and based on revisions to the microarchitecture of the prosthesis (i.e., no infill pattern). Here, HAp and DBM particles were combined with PCL at two weight ratios, 20 and 50 wt%, in addition to two combinatory HAp-DBM. Due to the various material ingredients and preprocessing conditions, quality assessment of prints was considered. The control (PCL) and positive control (ball milled 20 wt% HAp) were generally heavier than coarse scaffolds. All specimens were between 4 and 5 mm for both diameter and height. A cylindrical 3D-printed scaffold was used to evenly distribute stress rather than the corners of a cube. Compared to porous coarse PCL, 20 wt% HAp, and 50 wt% HAp scaffolds, the roller milled solid specimens exhibited a 3.23-fold, 1.73-fold, and 1.34-fold increase in Young's modulus, respectively. The coarse experimental groups were significantly less than PCL alone, but still above par for the required strength experienced by the mandibular condyle (50-100lb_f) (97).

A limitation of previous degradation studies was the lack of time points during the first week. Therefore, solid cylindrical scaffolds of 20 and 50 wt% bioactive compositions were submerged in 5 M NaOH for one week consisting of 10 timepoints, and up to three weeks. Comparable to earlier degradation studies, controls (PCL alone and HAp groups) degraded slightly. Based on the pilot study, we understand that the ball milled 20 wt% HAp did not break down much *in vivo*. Therefore, we are interested in a faster degradation rate, which was observed by 5/15 wt% HAp-DBM. However, this multimaterial group lost sufficient mechanical properties by day four, compared to HAp only composites. The relationship between DBM and HAp degradation kinetics is not fully understood in this study; however, our findings suggest that DBM alone experiences rapid bulk degradation, likely due to its organic components being more

susceptible to hydrolytic breakdown (enzymatic *in vivo).* In contrast, HAp, with its mineralized and crystalline structure, shows slower bulk degradation, likely due to its resistance to hydrolytic breakdown, which contributes to its sustained mechanical integrity over time. The tradeoffs of degradation kinetics may contribute to the processing method as well. Based on these results, we suggest using 50 wt% HAp or even a multimaterial HAp-DBM with higher HAp content *in vivo* based on degradation kinetics and mechanical analysis. Additionally, a long-term degradation study was conducted by evaluating PCL in phosphate-buffered saline (PBS) for 6 months offering relevant similarities to *in vivo* degradation. Compared to PCL under accelerated conditions, the data may indicate that one day in 5 M NaOH is similar to one month in PBS **(Figure A.7)**.

3.6 Conclusion

The current study demonstrated the feasibility of processing and fabrication of 3D-FDM PCL-composites for mandibular condyle tissue engineering. PCL was mixed with bioactive HAp and DBM, fabricated into commercially sized filament, and 3D-printed into experimental specimens. Although the PCL-composite particle sizes were decreased with cryogrinding, material composites exhibited smaller particle sizes and greater uniformity under roller mill and ball mill processing methods. Filament fabrication topography and tolerance is dependent on milling method and the rates of the extruder and puller. A maximum of 50 wt% bioactive materials can be 3D-printed at a range of 1.60-1.80 mm, however, non-uniform filaments may lead to varied material flow rates, which may affect mass and print quality. Nevertheless, HAp and DBM composites displayed excellent homogeneity up to 50 wt%. A dispersed mixture is desired to inhibit bioactive gradients, which could lead to bone ingrowth in non-desired areas or irregular degradation.

Theoretically, tissue engineers desire an implant that matches the degradation rate of biomaterial to bone resorption, to mechanically support cell adhesion, differentiation, and proliferation of osteo cells. The success of the device depends on a variety of factors, but mainly osseointegration and stress distribution (101). Other factors include mechanical performance, implant geometry, implant position, demographic bone density, and interface gaps. Regardless, the purpose of this study was to elucidate the mechanical integrity and degradation kinetic tradeoffs of various PCL composites. Based on the data, the PCL-composite should be ball milled to maximize uniformity and enhance mechanical performance *in vivo*. Additionally, our results

indicate that final prosthesis prints should be printed horizontally, to maximize performance and lessen failures during printing from support material. During 3D-printing, the biomaterial should undergo 60-80°C during processing (i.e., filament fabrication and 3D-printing) to retain osteogenic properties, which enhance bone regeneration capabilites. Based on the results, an increase of HAp only, such as 50 wt% HAp, or a future multimaterial HAp-DBM may promote bone regeneration *in vivo*, aligning with the natural timeline of bone resorption. Future work should evaluate multimaterial ratios consisting of higher HAp ratios compared to DBM, that is, 40 wt% HAp/10 wt% DBM, 42.5 wt% HAp/7.5 wt% DBM, and 45 wt% HAp/5 wt% DBM.

Chapter 4: Bioengineering of a Patient-Specific Temporomandibular Joint Mandibular Condyle Prosthesis

4.1 Abstract

A bioresorbable, patient-specific temporomandibular joint (TMJ) mandibular condyle prosthesis may restore functionality for skeletally immature patients, those with metal hypersensitivity, and those with hyperplasia. Here, we detail the complete workflow of implant development, including advanced computed tomography (CT) segmentation and computer-aided design (CAD) modeling to create a patient-specific design. The first iteration outlines the initial prosthesis prototype, which underwent implantation for 6 months in a pilot goat study. Following the pilot study, design improvements were made to enhance anatomical accuracy and mechanical durability, resulting in a second iteration intended for an upcoming caprine study. These advancements include optimized geometries for load distribution, improved material composition to enhance osteointegration, and dowel placement for fixation. In addition, the surgical guide required for condylectomy will be discussed, highlighting the importance of precision during implant placement to achieve successful outcomes. Constraints, justification, and design details are presented for each iteration. Mechanical characterization was conducted to determine the optimal shell thickness, leading to the selection of a 2.5 mm shell, which promoted a higher ultimate pound force range of 60-90 lb_f. By combining patient-specific modeling with iterative design improvements, this study establishes a robust framework for bioresorbable TMJ prosthesis development to house a ground bone, bone marrow, and growth factor slurry, paving the way for clinically viable solutions tailored to individual anatomical and biomechanical requirements.

4.2 Introduction

Temporomandibular joint (TMJ) disorders (TMD) are not limited to the mandibular condyle, but also the facial musculature, nerves, and other anatomical components. Consequently, the pathology and etiology of TMD are multifactorial and complex (3). Therefore, management options must be tailored to the patient. In the case of mandibular condyle TMD patients, symptoms experienced include, but are not limited to, limited mouth opening, pain, and clicking (6). If conservative treatments (pharmacology, splints) and minimally invasive surgeries (arthrocentesis) fail, surgical intervention may be required. Costochondral grafts are autogenous bone grafts derived from the rib. This construct resembles the native mandibular condyle, however, results have varied for the height and regenerative outcomes (102). Alloplastic devices, that is, total joint replacement (TJR) is another option. Using alloys and ceramic interfaces, TJR has a notorious history and can't be used for all mandibular condyle TMD patients (e.g., juvenile patients) (103). Ultimately, the current devices for end stage mandibular condyle TMD leave immature, arthritic, and metallic allergenic patients out of solutions (32).

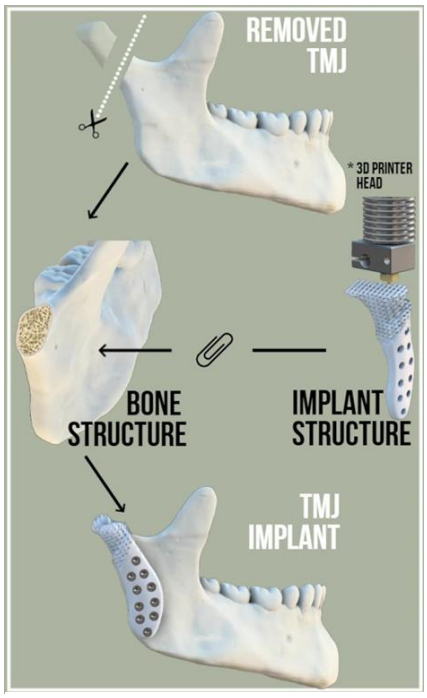

Bioengineered condylar implants present a promising alternative to conventional TJR by leveraging patient-specific designs and bioresorbable materials, offering an off-the-shelf surgical intervention (31). This approach addresses the challenges of anatomical accuracy, mechanical stability, and patient-specific needs while minimizing long-term complications. One critical advantage of bioengineered implants lies in their ability to achieve anatomical precision through advanced computed tomography (CT) segmentation (19; 54). By generating a 3D model from patient CT data, precise replication of the native condyle can be achieved, ensuring optimal fit and functional restoration by 3D-FDM

Figure 4.1: Condylectomy procedure for the bioengineered mandibular condyle device.

Using an oscillating saw, the condylar head is removed leaving the marrow cavity and trabecular bone from the resected ramus exposed. We employ 3D-fused deposition modeling to create the implant device and fixate the prosthetic onto the lateral side of the ramus. Repurposed from Ali Rassi.

(three dimensional fused deposition modeling) **(Figure 4.1)**. Moreover, computer-aided design (CAD) enhances the customization of the implant geometry to mimic the native mandibular condyle while incorporating features that promote osteointegration and load distribution. This includes the design of interconnected pores to facilitate vascularization and bone ingrowth, as well as a hollow condyle structure that houses a osteogenic cellular vehicle without compromising mechanical integrity (19). Strategic dowel placement within the condylar base also enhances initial fixation and long-term stability. An additional benefit of bioengineered condylar implants is the ability to ensure precise surgical placement using guide-assisted resection. Customized surgical guides derived from CT data ensure accurate condylectomy and implant placement, thereby reducing intraoperative errors and improving long-term outcomes. These guides enable the surgeon to achieve proper alignment and orientation, which is crucial for maintaining joint function, reducing the interface space, and minimizing complications in the surrounding TMJ tissues (19).

By integrating anatomical accuracy, advanced modeling techniques, optimized mechanical design, and precise placement, bioengineered condylar implants hold the potential to surpass current TJR solutions, particularly for patients with unique challenges, that is, (1) skeletally immature patients, (2) those with metal hypersensitivity, and (3) those with hyperplasia. As the TMJ bioengineering field progresses, the development of patient-specific bioresorbable prostheses could significantly enhance the quality of life for individuals with TMD, who are unsuitable candidates for traditional joint replacement or costochondral grafts.

4.3 Materials and methods

4.3.1 Materials

All materials were purchased from Sigma-Aldrich (St. Louis, MO) unless otherwise stated.

4.3.2 Composite fabrication and filament manufacturing

For the 6-month pilot study, a 20 wt% hydroxyapatite/polycaprolactone (HAp, Sigma-Aldrich, St. Louis, MO/PCL, 50k MW, Polysciences, Inc., Warrington, PA) material underwent planetarium ball milling for 6 hours, bi-directionally, reducing particle size to 100 microns. The composition was poured into a filament extruder (Filabot, Barre, VT) and extruded at 60°C through a cylindrical die. The filament melted was cast through a cold DI water trough and pulled by a

custom puller motor assembly. Manually adjusting the rate of extruder and puller allowed the formation of a filament diameter of ~1.75 mm. The resulting filament was collected on a spool and placed in a desiccator (Stat Pro, PAC, Grapevine, TX) to remove moisture and prepare for fused deposition modeling.

For the new biomaterial composite, that is, 50 wt% HAp, the HAp (50 wt%) and PCL (50 wt%) were combined to form a 100 g batch. The composite was combined with ceramic balls of varied size at a 2:1 ratio and milled by planetarium ball mill for 6 hours. The homogenized batch was then collected and prepared for filament fabrication with the same extruder, water trough, and puller motor. The resulting filament was collected on a spool and placed in a desiccator (Stat Pro, PAC, Grapevine, TX) to remove moisture and prepare for fused deposition modeling.

4.3.3 Image segmentation

A patient-specific prosthesis was developed based on computed tomography (CT) scans of a sheep mandibular condyle. The medical imaging data were acquired and segmented using Seg3D (University of Utah SCI Institute) software. A Gaussian blur and threshold layer were used to select the mandible, ramus, and condyle bone structures. The coronal plane was placed perpendicular to the mandible, with the rams and condyle positioned posteriorly. A connected component filter was run, isolating the bone anatomy, and masking the right mandible. Registration points were generated based on the Frankfort plane (i.e., right inferior orbit and right superior external auditory meatus). The points were exported into custom MATLAB (MathWorks, Inc., Natick, MA) script, along with the masked right mandible. The standard triangle language (STL) output file was generated according to the new coordinate system based on registration points.

4.3.4 Prosthesis: Iteration 1

The right mandibular condyle and ramus STL file was modeled in Meshmixer (San Rafael, CA). The part was smoothed and scaled by 0.165 mm in all directions to ensure anatomical compatibility with the resected bone. The condylar head was cut 2 mm below superior guide height. The flange was made of three selections: 5 mm, 3 mm, and 2mm extrusions laterally. To be anatomically accurate, a Boolean difference was performed on the ramus. The flange was smoothed and combined with the condylar head to form a rough prosthesis. The flange was smooth

and tapered. Dowels were imported to create 8 screw holes sized 0.094”. The final STL output file was made solid and exported to Cura LulzBot Edition (Lulzbot, Fargo, North Dakota). Additionally, a separate condylar head STL output file was made solid and exported to Cura LulzBot Edition to generate the infill microarchitecture.

4.3.5 Prosthesis: Iteration 2

The right mandibular condyle and ramus STL file was modeled in Meshmixer (San Rafael, CA). The part was smoothed and scaled by 0.165 mm in all directions to ensure anatomical compatibility with the resected bone. The condylar head was cut 2 mm below superior guide height. Here, the flange was made of two selections: 5 mm and 3 mm extrusions laterally, creating a shorter flange. To be anatomically accurate, a Boolean difference was performed on the ramus. The flange was smoothed and combined with the condylar head to form rough prosthesis. The prosthesis neck and guide were smoothed. Dowels were imported to create 8 screw holes sized 0.094”. A 60% scaled condylar head was used to hollow out the main file by Boolean difference command, forming the 2.5 mm shell. The final STL output file was made solid and exported to PrusaSlicer 2.8.0 (Prusa Research, Prague, Czech Republic).

4.3.6 Prosthesis: Fused deposition modeling

The prosthesis was oriented to lay flat on the guide, laterally. For the Cura LulzBot Edition software, the final exported prosthesis and condylar head were aligned by rotation. The condylar head was scaled by 90% and edited with unique parameters: infill line distance of 0.6, infill pattern of zigzag, infill density of 80%, and wall count of 0. The flange piece was edited with unique parameters: layer height of 0.3, line width of 0.4, infill pattern of concentric, and infill density of 100%. The final slice exhibited the open zigzag porous face because the condylar head was edited as a mesh type of modification for overlap. Supports were automatically added to support the print during 3D-FDM. An initial brim line was used to assist with filament flow and print bed adhesion. The material used for 3D-FDM was 20 wt% HAp/PCL. For the PrusaSlicer 2.8.0 software, the final hollow exported prosthesis was imported. The flange was aligned in parallel with print bed and ready for slicing. The parameters were implemented from similar config presets: layer height of 0.3, line width of 0.4, infill pattern of rectilinear, and infill density of 100%. Both printing setups used a printing temperature of 70°C. The material used for 3D-FDM was 50 wt% HAp.

4.3.7 Guide: Iteration 1

The guide was configured using the enlarged flange portion of the prosthesis. The same dowel holes were used for both the guide and prosthesis. A plane was added to Meshmixer and aligned with the superior edge at a 30° angle. To generate the curve around the medio-posterior ramus, a Boolean difference was taken of the plane and ramus anatomy. The plane and flange were combined, made solid, and exported to Cura LulzBot Edition.

4.3.8 Guide: Iteration 2

The revised guide was generated by the same methods, keeping the same dowel positions and angle of plane. The plane section was shifted laterally by 5 mm and smoothed. This created a shorter wrap around medially and provided an extended shelf laterally, offering increased control of oscillating blade during condylectomy.

4.3.9 Guide: Fused deposition modeling

For the Cura LulzBot Edition software, the part was edited with unique parameters: layer height of 0.2, line width of 0.3, infill pattern of concentric, and infill density of 100%. Supports were automatically added to support the print during 3D-FDM. An initial brim line was used to assist with filament flow and print bed adhesion. For the PrusaSlicer 2.8.0 software, the final guide was imported. The flange was aligned in parallel with print bed and ready for slicing. The parameters were implemented from similar config presets: layer height of 0.2, line width of 0.3, infill pattern of rectilinear, and infill density of 100%. Both printing setups used a printing temperature of 210℃, commonly used for polylactic acid (PLA).

4.3.10 Sterilization

Each 3D-FDM printed prosthesis, and guide were sterilized overnight using an AN74i ethylene oxide sterilizer (Anderson Sterilizers, Haw River, North Carolina). The parts were placed in a sealed sterilization pouch and prepared for shipment.

4.3.11 Shell thickness

Two shell thicknesses were evaluated for prosthesis iteration 2: 1.5 mm and 2.5 mm. Two material compositions were 3D-FDM to form half-prostheses (i.e., cut flange), maximizing sample size of prints (n=3). The study compared PCL alone and 20 wt% HAp using both shell sizes. The prostheses were screwed onto a PLA-printed resected condyle for uniaxial compression

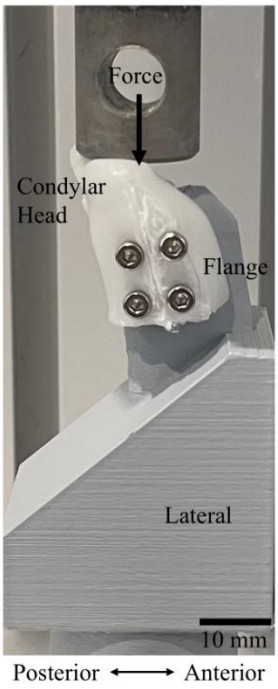

Figure 4.2: Illustration of the testing setup for shell thickness uniaxial compression.

The upper half of the prosthesis iteration 2 was mounted onto a 3D-printed resected ramus with an adapter for the mechanical tester. A 10 N taper load was applied then compressed uniaxially at 1 mm × min^{-1}.

(TestResources, Shakopee, MN). The same 10 N taper load and 1 mm × min^{-1} rate were used and aligned where the TMJ disc distributes loads onto the condylar head **(Figure 4.2)**.

4.3.12 Marrow packing

3D-FDM printed mandibular condylar heads were printed without the flange. Two bone marrow and iliac crest bone ratios were assessed for packing, that is, 2:1 and 1:1. The formulations were 1 g of iliac crest bone and 0.5 mL of heparinized bone marrow and 1 g of iliac crest bone and 1 mL of heparinized bone marrow, respectively.

4.3.13 Dowel placement

Two dowel orientations were assessed by an oral and maxillofacial surgeon. A staggered placement, advised by TMJ Concepts (Stryker) was used in iteration 1. A clustered placement was also evaluated by project clinician, which localized four dowels near the top and bottom flange portions. To limit micromotion and distribute stresses along the flange, the staggered placement from iteration 1 was used.

4.4 Results

4.4.1 Prosthesis: Iteration 1

Bioengineered mandibular condylar implants represent a transformative approach to TMJ reconstruction, offering enhanced anatomical precision and mechanical stability compared to conventional TJR devices or autogenous grafts. By leveraging advanced CT segmentation, 3D-FDM, and patient-specific CAD modeling, these implants ensure an optimal fit that closely replicates the native condyle. The integration of bioresorbable materials further promotes osteointegration while minimizing long-term complications. Additionally, customized surgical guides derived from patient CT data enhance the accuracy of condylectomy and implant placement, leading to improved clinical outcomes.

The initial prostheses were developed with relation to TMJ Concepts (n=6). The bioresorbable prosthesis consisted of a flange lining the length of the ramus laterally and wrapping around the posterior edge **(Figure 4.3)**. The condyle and flange portion overlapped by 2 mm, facilitating integrated fabrication using 3D-FDM. To optimize load distribution and stability, an open microarchitecture was generated using a zigzag pattern with x- and y-axis orientation on the build plate, featuring a pore size of 150 microns to uptake blood supply from the resected ramus.

Eight staggered dowels were incorporated along the flange to align with screw holes sized 0.094” for a tapered 2 mm screw (KLS Martin). The dowels acted as anchor points to secure the device along the ramus, maintaining positional integrity during load-bearing activities such as mastication. This staggered arrangement ensured uniform load transfer while minimizing micromotion at the bone-implant interface. The reduction of micromotion is critical to mitigating fibrous tissue formation and promoting osseointegration, thereby improving the long-term stability and functionality of the prosthesis.



Figure 4.3: Prosthesis Iteration 1

The initial prosthesis design featured a smooth, anatomically compatible condylar head with three lateral flange extrusions (5 mm, 3 mm, and 2 mm) for stability. 150-micron infill was generated using zigzag microarchitecture. Eight screw holes (0.094" diameter) were incorporated for secure fixation. The final STL file was exported to Cura LulzBot Edition for 3D printing and was subsequently prepared for sterilization.

4.4.2 Prosthesis: Iteration 2

Building upon the initial prosthesis design, an updated iteration was developed to further enhance mechanical robustness and house a ground bone, bone marrow, and growth factor slurry. Similarly to the original, the condyle and flange portion overlapped by 2 mm, maintaining a secure interface while optimizing joint stability. To better mimic the morphology of the native condylar head, a rounded extrusion was incorporated, creating a more anatomically accurate and structurally robust interface **(Figure 4.4)**.

In contrast to the original design, the flange edge wrapped a reduced amount around the posterior edge of the ramus, to lessen the obstruction of soft tissues around the TMJ environment. Furthermore, the overall flange length was shortened to decrease material bulk while maintaining sufficient coverage for fixation. The staggered dowel placement remained consistent, with eight screw holes strategically positioned to ensure secure attachment and minimize micromotion during condylar loading. To house a slurry of ground bone, aspirate bone marrow, and bone morphogenetic protein-2 (BMP-2), the condyle was hollowed out, eliminating the infill microarchitecture without compromising structural integrity. This design refinement aimed to optimize load distribution while minimizing stress concentrations at the condyle-flange junction, inhibit soft tissue damage, and deliver a vehicle of growth factors and osteogenic cells for enhanced osteogenesis at the resection interface.

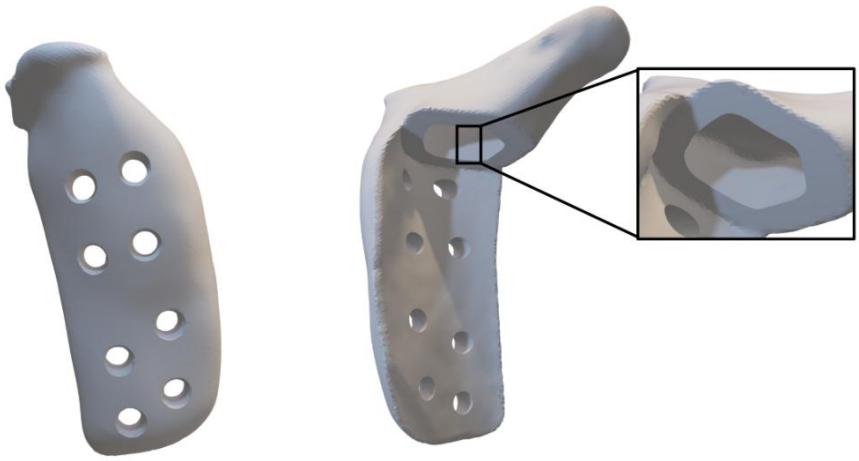

Figure 4.4: Prosthesis Iteration 2

The refined prosthesis was modeled to improve anatomical compatibility and reduce mass by hollowing the condylar head using a 60% or 70% scaled model. The flange was shortened and smoothed, with two lateral extrusions of 5 mm and 3 mm. Eight screw holes (0.094" diameter) were incorporated for secure fixation. The final STL file was exported to PrusaSlicer 2.8.0 for 3D printing and was subsequently prepared for sterilization.

4.4.3 Guide: Iteration 1

To ensure accurate fixation and compatibility with the prosthesis, the dowels on the guide were aligned to match the staggered dowel placement of the prosthesis. This consistent positioning facilitated seamless transition from condylectomy to prosthesis attachment, reducing intraoperative adjustments and promoting stability. The precision of dowel alignment was critical to maintaining the positional integrity of the final implant. The guide was designed with a prominent, straight edge along the intended cut line to accommodate the oscillating saw during surgery. This edge acted as a stable and secure surface against which the saw could be positioned, ensuring a clean and precise condylectomy. The rigidity of the flange also contributed to maintaining alignment during cutting, minimizing deviation and promoting accurate bone resection. The wrapped portion of the guide aided in proper positioning during placement, allowing it to conform closely to the ramus and maintain stability throughout the procedure. However, any misalignment during guide placement could result in an inaccurate cut, potentially creating a gap that may never fully osseointegrate, compromising long-term stability.

The Boolean difference with the ramus and the flange were combined into a single solid model and exported to Cura LulzBot Edition for 3D-FDM printing on the flange edge **(Figure 4.5)**. The material used was PLA, with support material added to ensure successful print completion. After printing, the guide was carefully removed from the build plate and prepared for sterilization.



Figure 4.5: Guide: Iteration 1

The guide was designed with dowels aligned to match the staggered placement of the prosthesis, facilitating accurate fixation and seamless transition during implant attachment. A prominent, straight edge was incorporated to accommodate the oscillating saw, ensuring a precise cut while maintaining alignment. The wrapped portion of the guide assisted with positioning against the ramus, enhancing stability during surgical placement. The guide was fabricated using PLA with support material to complete the print and was subsequently prepared for sterilization.

4.4.4 Guide: Iteration 2

For the second iteration of the surgical guide, design improvements focused on enhancing control and precision during the condylectomy procedure. The shifted and extended plane, featuring a rounded shelf, was incorporated to provide better stability and facilitate more accurate control during surgery. To ensure the same level of accurate fixation as the previous iteration, the plane was extended anteromedially into the sigmoid notch, optimizing alignment with the ramus while maintaining compatibility with the prosthesis.

The shorter flange was retained to minimize bulk, and its edges were carefully tapered to reduce the risk of soft tissue damage to surrounding structures, ensuring a more comfortable surgical process. Dowels were again positioned in alignment with the staggered prosthesis placement, maintaining precise fixation and minimizing potential misalignment during the procedure. The guide was designed to allow for smooth integration with the oscillating saw, ensuring that the cutting edge could be properly positioned against the guide's surface for a precise osteotomy.

The shifted and extended plane (dull) was combined with the shorter flange, made solid, and exported to Prusa Slicer for 3D-FDM on the flange edge **(Figure 4.6)**. Support material was added to complete the print. The guide was removed and prepared for sterilization.

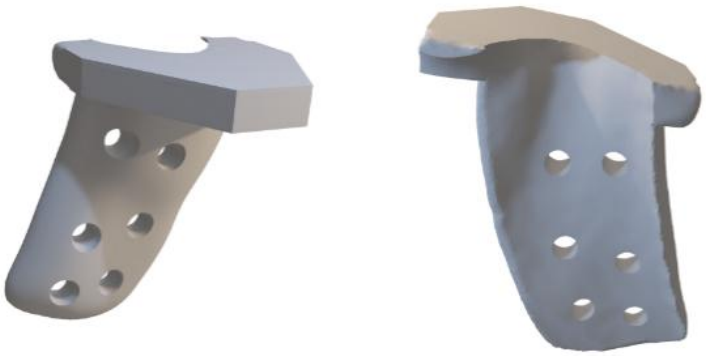

Figure 4.6: Guide: Iteration 2

The guide featured a shifted and extended plane, laterally, designed to improve oscillating saw control during condylectomy. Similar to the prosthesis iteration 2, the flange wrapping was reduced inferiorly. To accurately align the guide, the plane extruded anteromedially to fit in the sigmoid notch. Dowels remained aligned to match the staggered placement of the prosthesis, ensuring consistent fixation and accurate attachment. The guide was fabricated using 3D-FDM with support material, utilizing Prusa Slicer for optimal print settings. After printing, the guide was carefully removed from the build plate and prepared for sterilization.

4.4.5 Shell Thickness

The objective of this experiment was to evaluate the compressive performance of prosthesis iteration 2 based on shell thickness and material composition. Two shell thicknesses (i.e., 1.5 mm and 2.5 mm or 70% and 60%) were tested to determine their impact on compressive modulus and yield strength. To maximize the sample size, half-prostheses were printed using 3D-FDM after the flange was cut (n=3 per group). Two material compositions were compared: polycaprolactone (PCL) alone and a composite of 20 wt% hydroxyapatite (HAp) and PCL. The prostheses were secured onto a PLA-printed resected condyle with tapered 2 mm screw (KLS Martin) and subjected to uniaxial compression (TestResources, Shakopee, MN). The alignment was designed to simulate load distribution comparable to the TMJ disc on the condylar head **(Figure 4.2)**. A constant compression rate 1 mm × min^{-1} was applied throughout testing until failure.

The results, shown in **(Figure 4.7A)**, indicate no statistically significant difference in compressive modulus between the different shell thicknesses or material compositions. Yield stress results are presented in **(Figure 4.7B)**. PCL (0% HAp) at 1.5 mm shell thickness demonstrated significantly lower yield stress compared to PCL at 2.5 mm. For the composite material (20 wt% HAp), the 1.5 mm shell thickness exhibited significantly lower yield stress compared to the 2.5 mm thickness. Additionally, the yield stress of PCL (1.5 mm) was significantly lower than that of 20 wt% HAp (2.5 mm). An overall trend of increased yield strength was observed with the thicker 2.5 mm shell in both material compositions, suggesting that increasing shell thickness may enhance load-bearing capacity. We further investigated the ultimate force required to deform the prosthetic **(Figure 4.7C)**. The 2.5 mm shell groups displayed a maximum mechanical loading of 60-90 lb_f where the prosthetic should withstand 50-100 lb_f in an ovine animal model (97). One limitation of this experiment was the occasional slipping of the condylar head during compression, likely caused by the angle of the resected ramus-prosthesis interface or loose screw fixation. Additionally, lower strain values were observed due to this protocol flaw. This issue could be addressed in future iterations by tapering the hollow interface or thickening the wall to achieve a more secure and stable connection at the ramus interface.

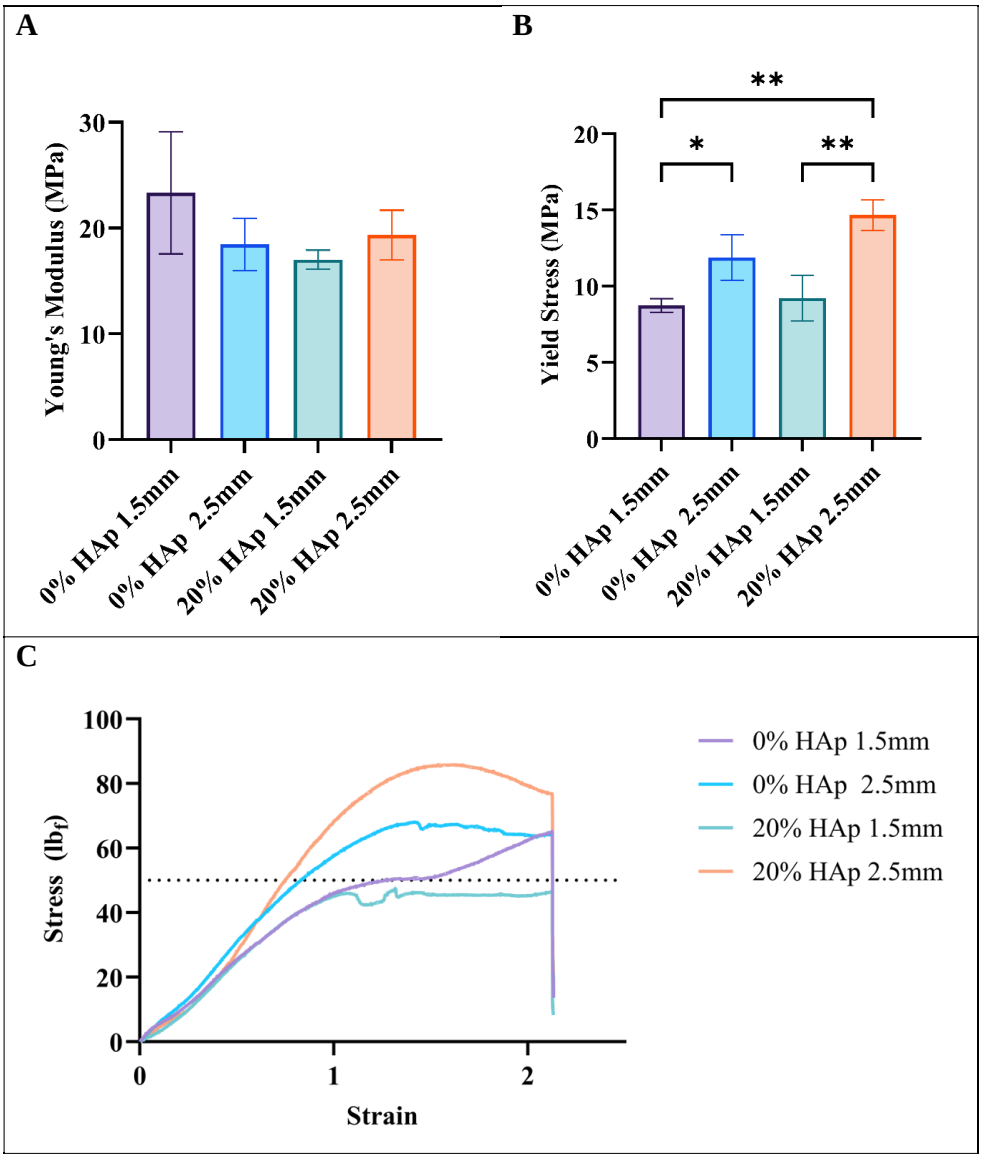

Figure 4.7: Modulus and yield stress of bioengineered condylar prostheses with varying shell thicknesses.

(A) *Compressive modulus of PCL (0% HAp) and 20 wt% HAp/PCL prostheses at 1.5 mm and 2.5 mm shell thicknesses, showing no statistically significant differences between shell thickness or material composition.* ***(B)*** *Yield stress comparison indicating a significant increase for PCL (2.5 mm) compared to PCL (1.5 mm) ($p < 0.05$), and a significant increase for 20 wt% HAp/PCL (2.5 mm) compared to 20 wt% HAp/PCL (1.5 mm) ($p < 0.01$). Additionally, the yield stress of 20 wt% HAp/PCL (2.5 mm) was significantly higher than that of PCL (1.5 mm) ($p < 0.01$). A trend of increased yield strength was observed with the thicker 2.5 mm shell in both material groups, indicating that increased shell thickness may enhance load-bearing capacity.* ***(C)*** *Stress-strain curve displaying relationship between strain (%) and pound force. The dash line indicates 50 lb_f, which is the necessary mechanical performance for use in an ovine animal model. Experimental limitations include potential slipping of the condylar head during compression, which may be mitigated in future designs by tapering the hollow interface with the resected ramus. Statistical analysis was performed using one-way ANOVA with Tukey's post hoc test.*

4.4.6 Marrow packing

3D-FDM printed mandibular condylar heads were packed with 2:1 and 1:1 ratios of ground iliac crest bone and heparinized bone marrow to assess the optimal consistency for integration within the condylar head shell **(Figure 4.8)**. A ratio of 1:1 was chosen as it provided a balanced mixture that maximized cellular content while maintaining sufficient structural integrity to remain in position within the hollow condylar cavity. This consistency ensured that the cell-laden mixture did not flow or collapse during handling and implantation, preserving a stable interface with the surrounding bone.

Additionally, the 1:1 ratio demonstrated favorable packing characteristics by conforming to the internal geometry of the condylar head, thereby maximizing contact with the internal surface and enhancing potential osteointegration. This combination of bone-marrow content (and latter addition of bone morphogenetic protein-2) and scaffold design aimed to promote osteogenesis and bone ingrowth while minimizing displacement during load-bearing activities. Future iterations may further investigate the influence of different ratios on mechanical stability and cell viability to optimize both the packing efficiency and biological performance of the prosthesis.



Figure 4.8: Packing condylar heads with marrow and ground bone mixture.

In the first illustration represents 1 g of ground autologous bone from iliac crest was prepared for combination. Then, 1 mL of marrow was added to ground bone, forming a 1:1 ratio mixture. The resulting mixture packed into the hollow cavity of the 3D-FDM printed PLA condylar head, demonstrating stable retention and conformation to the internal geometry. This packing strategy enhances the potential for osteointegration and will later serve as a vehicle for recombinant human bone morphogenetic protein-2. This finding was generated by Dr. Jakob Towsend at the Colorado State University.

4.5 Discussion

Regenerative solutions by tissue engineering have taken significant stride over the past two decades. However, a successful regenerative solution has not been clinically translated for the mandibular condyle. Our previous research has generated a polycaprolactone/hydroxyapatite (PCL/HAp) proof-of-concept prosthesis, capable of bone ingrowth and mechanical loading *in vivo* (19). We employed a mass ratio of 20 wt% HAp/80 wt% PCL. Utilizing low-temperature 3D-fused deposition modeling (3D-FDM), computer-aided design (CAD), and computed tomography (CT) technologies produced a feasible way to construct mandibular condyle scaffolds. After excision at the 6-month timepoint, micro-CT displayed novel osteo tissue growth and neocartilage. Yet, there was dissatisfaction with the amount of bone regeneration relative to the degradation of the implant and localized osteogenesis of the condyle. Using an acellular approach relies on the temporomandibular joint (TMJ) environment for blood supply, nutrients, and waste management, which may have contributed to the result. Preliminary data show our manufacturing process was successful in producing the implant. Therefore, adding more bioactive biomaterials to the material composition may overcome the limitations in the previous study. For the new loaded condyle, our approach would continue to allow for smooth clinical translation, functionally restoring the mandibular condyle for a lifetime, requiring a single surgical site.

Synthetic polymers, natural polymers, and extracellular matrix (ECM) derived materials have been used extensively for maxillofacial applications (See Chapter 2). However, the proposed synthetic polymer dominant blend is innovative for various reasons. First, no group has combined PCL, HAp, and demineralized bone matrix (DBM) together for a mandibular condyle regenerative replacement. However, some groups have fabricated PCL, HAp, or DBM scaffolds alone for large orthotopic models (54; 56; 58; 59). Other groups have developed scaffolds out of aliphatic copolymers, such as polylactic acid (PLA) and polyglycolic acid (PGA), with gelatin sponge (53). To our knowledge, our pilot study was the first of its kind. Additionally, no mandibular condyle prosthesis has been orthotopically implanted into a goat (13). One group fabricated PCL/HAp mandibular condyle prostheses that were implanted ectopically (subcutaneously). Since mandibular condyle temporomandibular joint disorders (TMD) encapsulate the bone, cartilage, muscles, and nerves, prosthesis designs should be evaluated orthotopically (sheep, minipig, goat) (24).

Second, the cellular design harvests autologous ground bone from the iliac crest, bone marrow from iliac crest, and recombinant human bone morphogenetic protein-2, streamlining clinical translation by minimizing immune rejection (i.e., versus allogeneic). However, the use of autologous materials may introduce additional regulatory challenges and increase overall costs, as stringent protocols must be followed to ensure safety and efficacy during harvesting, processing, and implantation. Despite these hurdles, Gordana Vunjak-Novakovic's group has displayed the feasible approach of custom bioreactors to seed cells onto a mandibular condyle scaffold (59). HAp and DBM have displayed bone growth and regenerative potential *in vivo* (56; 104). Therefore, increasing the amount of HAp or DBM, using similar manufacturing processes, may potentially enhance regenerative outcomes.

Third, 3D-FDM will be used to rapidly fabricate test specimens and prostheses. To our knowledge, no group has utilized 3D-FDM technology for fabricating mandibular condyle prostheses. One group used a laser sintering technique to create custom PCL scaffolds (57). Another group has employed solid free-form fabrication to successfully create PCL scaffolds (54). 3D-FDM systems allow rapid prototyping, are cost-effective, and can use custom bioactive filaments. Generally, CT and CAD are used to design microarchitecture and custom devices prior to 3D-FDM (19; 54; 57). Therefore, utilizing these technologies facilitates the fabrication of patient-specific devices to fit onto the resected ramus, hastening patient applicability. Finally, the 3D-FDM manufacturing process relies on low temperatures to print bioactive filaments. DBM is known to denature under high temperatures, reducing osteoinductive tendencies *in vivo* (105). During filament fabrication and 3D-FDM in future iterations, DBM blends will be quickly processed at 60-80°C to avoid loss of inductive components in the ECM-derived biomaterial.

4.6 Conclusion

To advance our pilot mandibular condyle device, we developed increased HAp and DBM composites scaffolds up to 50 wt%. Using design considerations and wants **(Table A.1, 2)**, CAD modeling allowed for a hollow prosthesis to address regenerative limitations observed in our pilot study. One major limitation identified was insufficient bone regeneration within the internal microarchitecture of the device, primarily due to a mismatch between the degradation rate and the natural bone resorption process. To improve performance *in vivo*, we evaluated increased bioactive ingredients that optimize design tradeoffs of mechanical performance (i.e., Young's modulus and

yield strength) and degradation rate. As a result, the 50 wt% HAp composite demonstrated enhanced compressive properties and a more favorable degradation profile for long-term use *in vivo*. The multimaterial HAp-DBM composites degraded rapidly causing concerns for mechanical integrity *in vivo*.

Another limitation was the acellular design and geometry of the device, which inherently relied on the blood supply of the resected ramus and the TMJ environment. In the pilot study, the HAp prostheses demonstrated the ability to conform to mechanical loads, maintaining structural integrity under physiological stress, allowing goats to retain function. We further revised the condyle-flange overlap and robustness, creating a more anatomically accurate mandibular condyle device, enabling strong osseointegration into the ramus and resection plane, facilitating bone ossification, and minimizing micromotion. In future iterations, a combinatory HAp-DBM with higher HAp content may enhance the recruitment of osseous cells. Moreover, together with an aliphatic polyester PCL, the composition may be capable of maintaining high stress distribution, while enabling bone regeneration of the mandibular condyle.

To further enhance bone regenerative capabilities, the hollow condylar head of the device will be packed with bone marrow, ground bone, and BMP-2, to create a bioactive slurry gradient in the hollow space. The slurry will be contained by the walls of the prosthesis, which were determined to be 2.5 mm thick to maintain the compressive loads experienced in the TMJ. Future iteratives include adding porosity to the anterior and posterior sides of the condylar head to allow blood intrusion or tapering the hollow interface to prevent slipping during masticatory loads. The utilization of pores would establish a tradeoff to make the shell thicker, such as 3 mm or 3.5 mm, to further ensure mechanical integrity.

Chapter 5: Discussion and Conclusion

5.1 Summary

The temporomandibular joint (TMJ) is a bilateral-complex joint that connects the mandible to the skull, enabling essential functions such as chewing, speaking, and swallowing. TMJ disorders (TMD) affect millions worldwide, leading to pain, dysfunction, and reduced quality of life. In severe cases involving advanced internal derangement, trauma, or osteoarthritis, surgical interventions, such as condylectomy, costochondral grafts, or total joint replacement may be required. However, alloplastic total joint replacement or autogenous grafts, limit adaptability, risk foreign body reaction, and require secondary surgeries. These permanent prosthetics, which do not adapt to the patient's growth and are fabricated from a limited range of metallic materials are inadequate for (1) juvenile patients, (2) patients with metal hypersensitivity, and (3) patients with advanced tissue degeneration or structural damage (i.e., scar tissue) to the TMJ. In contrast, a bioengineered tissue replacement, developed using biodegradable materials, stem cells, and chondrogenic/osteogenic growth factors, may offer a promising solution for restoring TMJ functionality.

The purpose of this study was to build on recent data which indicated limitations regarding osteogenesis, and the mismatch between *in vivo* degradation and bone resorption rate. To determine an optimal solution for the revised biomaterial composition and prosthetic design, we asked two questions: (1) How can the compressive modulus and degradation rate of these scaffolds be tuned to match natural bone remolding and (2) What specific scaffold design will maximize osseointegration and mechanical performance when implanted? To elucidate the optimal composition, we developed combinatory experimental specimens composed of polycaprolactone (PCL), hydroxyapatite (HAp), and demineralized bone matrix (DBM), leveraging three dimensional-fused deposition modeling (3D-FDM) techniques to evaluate mechanical performance and degradation kinetics. Mechanical testing demonstrated that increased bioactive material weight percentages improved compressive properties. Under accelerated degradation conditions, PCL/DBM composites were more prone to bulk degradation compared to PCL/HAp composites, suggesting that while HAp may be necessary for structural integrity, DBM could accelerate degradation while also providing enhanced osteoinductive properties. This may be due

to the highly crystallized native structure of HAp, compared to a collagen-based DBM biomaterial. This indicates that a HAp composition, such as 50 wt% HAp, may improve mechanical performance and biological outcomes compared to previously used 20 wt% HAp *in vivo*. Moreover, to further induce an osteoinductive response, a multimaterial composite may be used in the future. However, high weight percentages of DBM may cause failure during implantation. For now, the 50 wt% composite biomaterial, homogenized with planetarium ball milling, and combined with an osteogenic cellular vehicle, addresses the limitations of our pilot and existing end-stage devices by offering a patient-tailorable solution that integrates with the mandibular condyle, providing biomechanical stability and promoting bone regeneration. These advancements offer a significant step toward clinically translatable mandibular condyle replacements.

5.2 Future Directions

The study displayed the feasibility of creating composites up to 50 wt%. Further experiments should investigate mixing higher amounts of HAp with DBM, such as, 40 wt% HAp/10 wt% DBM, 42.5 wt% HAp/7.5 wt% DBM, and 45 wt% HAp/5 wt% DBM. For prosthetic modeling, future iterations might include pores (e.g., inferior surface) for additional vascularization and waste diffusion of the hollow cavity. The utilization of pores would establish a tradeoff to make the shell thicker, such as 3 mm or 3.5 mm, to further ensure mechanical integrity **(Figure A.8)**. Additionally, tapering of the condyle-ramus interface may assist with load distribution to the ramus interface to address slipping during mastication **(Figure A.9)**. Long term future work would analyze our tissue engineered prosthetic in other large animal models, such as a porcine model, introducing other variables contributing to *in vivo* performance. To further enhance clinical translation, equipment should be sterilized throughout the processing, fabrication, and 3D-fused deposition modeling steps to address formulation contamination.

5.3 Conclusion

The development of a bioengineered TMJ replacement presents a promising and exciting alternative to current surgical interventions, which often rely on FDA-approved and non-adaptive alloplastic implants or autogenous grafts with major limitations. By investigating biodegradable materials such as PCL, HAp, and DBM, this study aimed to address key challenges related to degradation kinetics, mechanical performance, and osteogenic potential. Our findings indicate that the 50 wt% HAp composite biomaterial, balanced structural integrity and controlled degradation,

attractive for use in future sheep animal model. Beyond material characterization, scaffold design and fabrication techniques play a critical role in optimizing performance. 3D-FDM enabled precise structural control, while homogenization techniques such as ball milling, improved composite uniformity. A systematic review of preclinical TMJ studies suggests that an ideal prosthetic solution will likely incorporate polymer scaffolds, osteoinductive growth factors, and patient-specific fabrication strategies, therefore we will continue this forward. Further research, including alternative animal models and sterile manufacturing approaches, will be necessary to translate these findings into a clinically viable TMJ replacement. Ultimately, the continued advancement of biomaterials research, interdisciplinary collaboration between clinicians and biomedical engineers, and the refinement of tissue engineering approaches are essential to enable a clinically translatable, patient-specific solution for TMJ mandibular condyle reconstruction.

References

1. Acri TM, Shin K, Seol D, Laird NZ, Song I, et al. 2019. Tissue Engineering for the Temporomandibular Joint. *Adv Healthc Mater* 8:e1801236
2. Zieliński G, Pająk-Zielińska B, Ginszt M. 2024. A Meta-Analysis of the Global Prevalence of Temporomandibular Disorders. *Journal of Clinical Medicine* 13:1365
3. Murphy MK, Macbarb RF, Wong ME, Athanasiou KA. 2013. Temporomandibular Disorders: A Review of Etiology, Clinical Management, and Tissue Engineering Strategies. *The International Journal of Oral & Maxillofacial Implants* 28:e393-e414
4. Bäckström E, Wänman A, Sjöström M. 2024. The majority of patients report satisfaction more than 24 years after temporomandibular joint discectomy. *Oral and Maxillofacial Surgery* 28:1539-45
5. Dimitroulis G. 2018. Management of temporomandibular joint disorders: A surgeon's perspective. *Australian Dental Journal* 63:S79-S90
6. Stowell AW, Gatchel RJ, Wildenstein L. 2007. Cost-effectiveness of treatments for temporomandibular disorders: Biopsychosocial intervention versus treatment as usual. *The Journal of the American Dental Association* 138:202-8
7. Luis G. Vega DDS RG-GM, PhD, Patrick J. Louis DDS, MD. 2013/05/01. Reconstruction of Acquired Temporomandibular Joint Defects. *Oral and Maxillofacial Surgery Clinics of North America* 25
8. Vaira LA, De Riu G. 2023. Temporomandibular Joint Disorders: Functional and Conservative Treatment. *J Clin Med* 12
9. Mercuri L. 2015. *Temporomandibular Joint Total Joint Replacement – TMJ TJR: A Comprehensive Reference for Researchers, Materials Scientists, and Surgeons*. 1-301 pp.
10. Ingawalé S, Goswami T. 2009. Temporomandibular Joint: Disorders, Treatments, and Biomechanics. *Annals of Biomedical Engineering* 37:976-96
11. Mercuri LG. 2024. Alloplastic temporomandibular joint replacement – past, present, and future: “Learn from the past, prepare for the future, live in the present.” Thomas S. Monson. *British Journal of Oral and Maxillofacial Surgery* 62:91-6
12. Sekhoto MG, Rikhotso RE, Rajendran S. 2019. Management of unpredictable outcomes of costochondral grafts. *International Journal of Surgery Case Reports* 62:144-9
13. Helgeland E, Shanbhag S, Pedersen TO, Mustafa K, Rosén A. 2018. Scaffold-Based Temporomandibular Joint Tissue Regeneration in Experimental Animal Models: A Systematic Review. *Tissue Eng Part B Rev* 24:300-16
14. Roychoudhury A, Yadav P, Bhutia O, Mane R, Yadav R, et al. 2021. Alloplastic total joint replacement in management of temporomandibular joint ankylosis. *J Oral Biol Craniofac Res* 11:457-65
15. Rauniyar D, Upadhyaya C, Chaurasia N, Shakya M, Sharma S. 2023. Total temporomandibular joint replacement in recurrent temporomandibular joint ankylosis: a case report. *J Surg Case Rep* 2023:rjad426

16. Lee SH, Ryu DJ, Kim HS, Kim HG, Huh JK. 2013. Alloplastic total temporomandibular joint replacement using stock prosthesis: a one-year follow-up report of two cases. *J Korean Assoc Oral Maxillofac Surg* 39:297-303
17. Resnick CM. 2018. Temporomandibular Joint Reconstruction in the Growing Child. *Oral and Maxillofacial Surgery Clinics of North America* 30:109-21
18. Aryaei A, Vapniarsky N, Hu JC, Athanasiou KA. 2016. Recent Tissue Engineering Advances for the Treatment of Temporomandibular Joint Disorders. *Current Osteoporosis Reports* 14:269-79
19. Nedrelow DS, Rassi A, Ajeeb B, Jones CP, Huebner P, et al. 2023. Regenerative Engineering of a Biphasic Patient-Fitted Temporomandibular Joint Condylar Prosthesis. *Tissue engineering.* 29:307-20
20. Detamore MS, Athanasiou KA. 2003. Structure and function of the temporomandibular joint disc: implications for tissue engineering. *J Oral Maxillofac Surg* 61:494-506
21. 2000 Mar. Three-dimensional finite element analysis of the human temporomandibular joint disc - PubMed. *Journal of biomechanics* 33
22. Michael S. Detamore KAA. 2003. Motivation, characterization, and strategy for tissue engineering the temporomandibular joint disc. *Tissue Eng.* 9
23. Durham J, Wassell R. 2011/03. Recent Advancements in Temporomandibular Disorders (TMDs). *Reviews in Pain* 5
24. Alejandro J. Almarza P, Bryan N. Brown, PhD, Boaz Arzi, DVM, DAVDC, DEVDC, David Faustino Ângelo, MD, William Chung, MD, DDS, Stephen F. Badylak, DVM, PhD, MD, and Michael S. Detamore, PhD. 2018. Preclinical Animal Models for Temporomandibular Joint Tissue Engineering. *Tissue Eng. Part B Rev* 24
25. Xiang T, Tao Z-Y, Liao L-F, Wang S, Cao D-Y. 2021. Animal Models of Temporomandibular Disorder. *Journal of Pain Research* 14
26. Van Bellinghen X, Idoux-Gillet Y, Pugliano M, Strub M, Bornert F, et al. 2018. Temporomandibular Joint Regenerative Medicine. *Int J Mol Sci* 19
27. Melville JC, Mañón VA, Blackburn C, Young S. 2019. Current Methods of Maxillofacial Tissue Engineering. *Oral Maxillofac Surg Clin North Am* 31:579-91
28. 2007 Aug. A call to action for bioengineers and dental professionals: directives for the future of TMJ bioengineering - PubMed. *Annals of biomedical engineering* 35
29. Almarza AJ, Mercuri LG, Arzi B, Gallo LM, Granquist E, et al. 2020. Temporomandibular Joint Bioengineering Conference: Working Together Toward Improving Clinical Outcomes. *Journal of Biomechanical Engineering* 142
30. Mercuri LG. 2023/05. Temporomandibular Joint Facts and Foibles. *Journal of Clinical Medicine* 12
31. Detamore MS, Athanasiou KA, Mao J. 2007. A Call to Action for Bioengineers and Dental Professionals: Directives for the Future of TMJ Bioengineering. *Annals of Biomedical Engineering* 35:1301-11

32. Jean R. Salash RHH, Alejandro J. Almarza, Joli C. Chou, Joseph P. McCain, Louis G. Mercuri, Larry M. Wolford, Michael S. Detamore. 2016. Potential Indications for Tissue Engineering in Temporomandibular Joint Surgery. *J Oral Maxillofac Surg* 74
33. Matheus HR, Özdemir ŞD, Guastaldi FPS. 2022. Stem cell-based therapies for temporomandibular joint osteoarthritis and regeneration of cartilage/osteochondral defects: a systematic review of preclinical experiments. *Osteoarthritis and Cartilage* 30:1174-85
34. Weng Y, Cao Y, Arevalo C, Vacanti MP, Vacanti CA. 2001. Tissue-engineered composites of bone and cartilage for mandible condylar reconstruction. *Journal of oral and maxillofacial surgery* 59:185-90
35. Schek RM, Taboas JM, Hollister SJ, Krebsbach PH. 2005. Tissue engineering osteochondral implants for temporomandibular joint repair. *Orthod Craniofac Res* 8:313-9
36. Schek RM, Taboas JM, Segvich SJ, Hollister SJ, Krebsbach PH. 2004. Engineered Osteochondral Grafts Using Biphasic Composite Solid Free-Form Fabricated Scaffolds. *Tissue Engineering* 10:1376-85
37. Alhadlaq A, Mao JJ. 2003. Tissue-engineered neogenesis of human-shaped mandibular condyle from rat mesenchymal stem cells. *J Dent Res* 82:951-6
38. Alhadlaq A, Mao JJ. 2005. Tissue-engineered osteochondral constructs in the shape of an articular condyle. *J Bone Joint Surg Am* 87:936-44
39. Embree MC, Chen M, Pylawka S, Kong D, Iwaoka GM, et al. 2016. Exploiting endogenous fibrocartilage stem cells to regenerate cartilage and repair joint injury. *Nature Communications* 7:13073
40. Puelacher WC, Wisser J, Vacanti CA, Ferraro NF, Jaramillo D, Vacanti JP. 1994. Temporomandibular joint disc replacement made by tissue-engineered growth of cartilage. *J Oral Maxillofac Surg* 52:1172-7; discussion 7-8
41. Wu Y, Gong Z, Li J, Meng Q, Fang W, Long X. 2014. The pilot study of fibrin with temporomandibular joint derived synovial stem cells in repairing TMJ disc perforation. *Biomed Res Int* 2014:454021
42. Li Y, Cai H, Fang W, Meng Q, Wu Y, et al. 2014. Triple-layered cell sheet for tissue-engineering the synovial membrane of the temporomandibular joint. *Cells Tissues Organs* 199:150-8
43. Zheng YH, Su K, Kuang SJ, Li H, Zhang ZG. 2012. [New bone and cartilage tissues formed from human bone marrow mesenchymal stem cells derived from human condyle in vivo]. *Zhonghua Kou Qiang Yi Xue Za Zhi* 47:10-3
44. Wang F, Hu Y, He D, Zhou G, Yang X, Ellis E, 3rd. 2017. Regeneration of subcutaneous tissue-engineered mandibular condyle in nude mice. *J Craniomaxillofac Surg* 45:855-61
45. Zheng YH, Su K, Jian YT, Kuang SJ, Zhang ZG. 2011. Basic fibroblast growth factor enhances osteogenic and chondrogenic differentiation of human bone marrow mesenchymal stem cells in coral scaffold constructs. *J Tissue Eng Regen Med* 5:540-50

46. Chen F, Mao T, Tao K, Chen S, Ding G, Gu X. 2002. Bone graft in the shape of human mandibular condyle reconstruction via seeding marrow-derived osteoblasts into porous coral in a nude mice model. *J Oral Maxillofac Surg* 60:1155-9
47. Bordoni B, Varacallo M. 2024. Anatomy, Head and Neck, Temporomandibular Joint. In *StatPearls*. Treasure Island (FL): StatPearls Publishing Copyright © 2024, StatPearls Publishing LLC. Number of.
48. Wilkie G, Al-Ani Z. 2022. Temporomandibular joint anatomy, function and clinical relevance. *British Dental Journal* 233:539-46
49. Singh B, Kumar NR, Balan A, Nishan M, Haris PS, et al. 2020. Evaluation of Normal Morphology of Mandibular Condyle: A Radiographic Survey. *J Clin Imaging Sci* 10:51
50. Kuroda S, Tanimoto K, Izawa T, Fujihara S, Koolstra JH, Tanaka E. 2009. Biomechanical and biochemical characteristics of the mandibular condylar cartilage. *Osteoarthritis and Cartilage* 17:1408-15
51. Garstka AA, Kozowska L, Kijak K, Brzózka M, Gronwald H, et al. 2023. Accurate Diagnosis and Treatment of Painful Temporomandibular Disorders: A Literature Review Supplemented by Own Clinical Experience. *Pain Research and Management* 2023:1002235
52. Athanasiou KA, Almarza AA, Detamore MS, Kalpakci KN. 2009. Tissue Engineering of the Mandibular Condyle. In *Tissue Engineering of Temporomandibular Joint Cartilage*, ed. KA Athanasiou, AA Almarza, MS Detamore, KN Kalpakci:57-61. Cham: Springer International Publishing. Number of 57-61 pp.
53. Ueki K, Takazakura D, Marukawa K, Shimada M, Nakagawa K, et al. 2003. The use of polylactic acid/polyglycolic acid copolymer and gelatin sponge complex containing human recombinant bone morphogenetic protein-2 following condylectomy in rabbits. *J Craniomaxillofac Surg* 31:107-14
54. Smith MH, Flanagan CL, Kemppainen JM, Sack JA, Chung H, et al. 2007. Computed tomography-based tissue-engineered scaffolds in craniomaxillofacial surgery. *Int J Med Robot* 3:207-16
55. El-Bialy T, Uludag H, Jomha N, Badylak SF. 2010. In vivo ultrasound-assisted tissue-engineered mandibular condyle: a pilot study in rabbits. *Tissue Eng Part C Methods* 16:1315-23
56. Ciocca L, Donati D, Fantini M, Landi E, Piattelli A, et al. 2013. CAD-CAM-generated hydroxyapatite scaffold to replace the mandibular condyle in sheep: preliminary results. *J Biomater Appl* 28:207-18
57. Abramowicz S, Crotts SJ, Hollister SJ, Goudy S. 2021. Tissue-engineered vascularized patient-specific temporomandibular joint reconstruction in a Yucatan pig model. *Oral Surg Oral Med Oral Pathol Oral Radiol* 132:145-52
58. Bhumiratana S, Bernhard JC, Alfi DM, Yeager K, Eton RE, et al. 2016. Tissue-engineered autologous grafts for facial bone reconstruction. *Sci Transl Med* 8:343ra83

59. Chen D, Wu JY, Kennedy KM, Yeager K, Bernhard JC, et al. 2020. Tissue engineered autologous cartilage-bone grafts for temporomandibular joint regeneration. *Science Translational Medicine* 12:eabb6683
60. Ba S, Zhou P, Yu M. 2021. Ultrasound is Effective to Treat Temporomandibular Joint Disorder. *J Pain Res* 14:1667-73
61. Jazayeri HE, Tahriri M, Razavi M, Khoshroo K, Fahimipour F, et al. 2017. A current overview of materials and strategies for potential use in maxillofacial tissue regeneration. *Materials Science and Engineering: C* 70:913-29
62. Durham EL, Howie RN, Hall S, Larson N, Oakes B, et al. 2018. Optimizing bone wound healing using BMP2 with absorbable collagen sponge and Talymed nanofiber scaffold. *Journal of Translational Medicine* 16:321
63. Shi H, Zhou Z, Li W, Fan Y, Li Z, Wei J. 2021. Hydroxyapatite Based Materials for Bone Tissue Engineering: A Brief and Comprehensive Introduction. *Crystals* 11:149
64. Habibah TU, Amlani DV, Brizuela M. 2023. *Hydroxyapatite Dental Material*. StatPearls Publishing, Treasure Island (FL)
65. Rezwan K, Chen QZ, Blaker JJ, Boccaccini AR. 2006. Biodegradable and bioactive porous polymer/inorganic composite scaffolds for bone tissue engineering. *Biomaterials* 27:3413-31
66. Temple JP, Yeager K, Bhumiratana S, Vunjak-Novakovic G, Grayson WL. 2014. Bioreactor cultivation of anatomically shaped human bone grafts. *Methods Mol Biol* 1202:57-78
67. Grayson WL, Fröhlich M, Yeager K, Bhumiratana S, Chan ME, et al. 2010. Engineering anatomically shaped human bone grafts. *Proc Natl Acad Sci U S A* 107:3299-304
68. Trindade D, Cordeiro R, José HC, Ângelo DF, Alves N, Moura C. 2021/07. Biological Treatments for Temporomandibular Joint Disc Disorders: Strategies in Tissue Engineering. *Biomolecules* 11
69. Tanaka E, Detamore MS, Tanimoto K, Kawai N. 2008. Lubrication of the temporomandibular joint. *Ann Biomed Eng* 36:14-29
70. Nickel JC, Iwasaki LR, Gonzalez YM, Gallo LM, Yao H. 2018. Mechanobehavior and Ontogenesis of the Temporomandibular Joint. *J Dent Res* 97:1185-92
71. Chan WP, Lin MF, Fang CL, Lai WF. 2004. MRI and histology of collagen template disc implantation and regeneration in rabbit temporomandibular joint: preliminary report. *Transplant Proc* 36:1610-2
72. Lai WF, Tsai YH, Su SJ, Su CY, Stockstill JW, Burch JG. 2005. Histological analysis of regeneration of temporomandibular joint discs in rabbits by using a reconstituted collagen template. *Int J Oral Maxillofac Surg* 34:311-20
73. Brown BN, Chung WL, Pavlick M, Reppas S, Ochs MW, et al. 2011. Extracellular Matrix as an Inductive Template for Temporomandibular Joint Meniscus Reconstruction: A Pilot Study. *Journal of Oral and Maxillofacial Surgery* 69:e488-e505

74. Brown BN, Chung WL, Almarza AJ, Pavlick MD, Reppas SN, et al. 2012. Inductive, Scaffold-Based, Regenerative Medicine Approach to Reconstruction of the Temporomandibular Joint Disk. *Journal of Oral and Maxillofacial Surgery* 70:2656-68
75. Ahtiainen K, Mauno J, Ellä V, Hagström J, Lindqvist C, et al. 2013. Autologous adipose stem cells and polylactide discs in the replacement of the rabbit temporomandibular joint disc. *J R Soc Interface* 10:20130287
76. Kobayashi E, Nakahara T, Inoue M, Shigeno K, Tanaka A, Nakamura T. 2015. Experimental Study on In Situ Tissue Engineering of the Temporomandibular Joint Disc using Autologous Bone Marrow and Collagen Sponge Scaffold. *Journal of Hard Tissue Biology* 24:211-8
77. Tarafder S, Koch A, Jun Y, Chou C, Awadallah MR, Lee CH. 2016. Micro-precise spatiotemporal delivery system embedded in 3D printing for complex tissue regeneration. *Biofabrication* 8:025003
78. Wang KH, Chan WP, Chiu LH, Tsai YH, Fang CL, et al. 2017. Histological and Immunohistochemical Analyses of Repair of the Disc in the Rabbit Temporomandibular Joint Using a Collagen Template. *Materials (Basel)* 10
79. Vapniarsky N, Huwe LW, Arzi B, Houghton MK, Wong ME, et al. 2018. Tissue engineering toward temporomandibular joint disc regeneration. *Science Translational Medicine* 10:eaaq1802
80. Ângelo DF, Wang Y, Morouço P, Monje F, Mónico L, et al. 2021. A randomized controlled preclinical trial on 3 interposal temporomandibular joint disc implants: TEMPOJIMS-Phase 2. *J Tissue Eng Regen Med* 15:852-68
81. Brown BN, Chung WL, Lowe J, LoPresti ST, Cheetham J, et al. 2022. Inductive Remodeling of Extracellular Matrix Scaffolds in the Temporomandibular Joint of Pigs. *Tissue Eng Part A* 28:447-57
82. Chung WL, Brown BN, Almarza AJ. 2022. Decellularized small intestine submucosa device for temporomandibular joint meniscus repair: Acute timepoint safety study. *Plos one* 17:e0273336
83. Jeong HJ, Koch A, Park S, Tarafder S, Lee CH. 2025. Bioactive scaffolds integrated with micro-precise spatiotemporal delivery and in vivo degradation tracking for complex tissue regeneration. *Engineered Regeneration*
84. Legemate K, Tarafder S, Jun Y, Lee CH. 2016. Engineering Human TMJ Discs with Protein-Releasing 3D-Printed Scaffolds. *J Dent Res* 95:800-7
85. Angelo DF, Morouço P, Alves N, Viana T, Santos F, et al. 2016. Choosing sheep (Ovis aries) as animal model for temporomandibular joint research: Morphological, histological and biomechanical characterization of the joint disc. *Morphologie* 100:223-33
86. Ângelo DF, Gil FM, González-García R, Mónico L, Sousa R, et al. 2018. Effects of bilateral discectomy and bilateral discopexy on black Merino sheep rumination kinematics: TEMPOJIMS – phase 1 – pilot blinded, randomized preclinical study. *Journal of Cranio-Maxillofacial Surgery* 46:346-55

87. Ângelo DF, Morouço P, Monje Gil F, Mónico L, González-Gárcia R, et al. 2018. Preclinical randomized controlled trial of bilateral discectomy versus bilateral discopexy in Black Merino sheep temporomandibular joint: TEMPOJIMS – Phase 1- histologic, imaging and body weight results. *Journal of Cranio-Maxillofacial Surgery* 46:688-96
88. S Abramowicz MFD, S B Lewis, C Dolce. 2008 Aug. Temporomandibular joint reconstruction after failed teflon-proplast implant: case report and literature review - PubMed. *International journal of oral and maxillofacial surgery* 37
89. Ang KC, Leong KF, Chua CK, Chandrasekaran M. 2007. Compressive properties and degradability of poly(epsilon-caprolatone)/hydroxyapatite composites under accelerated hydrolytic degradation. *J Biomed Mater Res A* 80:655-60
90. Cousin MA, Greenberg AJ, Koep TH, Angius D, Yaszemski MJ, et al. 2016. The Value of Systematic Reviews in Estimating the Cost and Barriers to Translation in Tissue Engineering. *Tissue Eng Part B Rev* 22:430-7
91. Badylak SF, Freytes DO, Gilbert TW. 2009. Extracellular matrix as a biological scaffold material: Structure and function. *Acta Biomater* 5:1-13
92. Donahue RP, Hu JC, Athanasiou KA. 2019. Remaining Hurdles for Tissue-Engineering the Temporomandibular Joint Disc. *Trends in Molecular Medicine* 25:241-56
93. Hollister SJ, Lin CY, Saito E, Lin CY, Schek RD, et al. 2005. Engineering craniofacial scaffolds. *Orthod Craniofac Res* 8:162-73
94. Valenti C, Federici MI, Coniglio M, Betti P, Pancrazi GP, et al. 2024. Mechanical and biological properties of polymer materials for oral appliances produced with additive 3D printing and subtractive CAD-CAM techniques compared to conventional methods: a systematic review and meta-analysis. *Clin Oral Investig* 28:396
95. Nedrelow DS, Townsend JM, Detamore MS. 2024. Osteochondral Regeneration With Anatomical Scaffold 3D-Printing-Design Considerations for Interface Integration. *J Biomed Mater Res A*
96. Ottenbrite RM, Javan R. 2005. Biological Structures. In *Encyclopedia of Condensed Matter Physics*, ed. F Bassani, GL Liedl, P Wyder:99-108. Oxford: Elsevier. Number of 99-108 pp.
97. Orassi V, Duda GN, Heiland M, Fischer H, Rendenbach C, Checa S. 2021. Biomechanical Assessment of the Validity of Sheep as a Preclinical Model for Testing Mandibular Fracture Fixation Devices. *Front Bioeng Biotechnol* 9:672176
98. Kukla C, Gonzalez-Gutierrez J, Duretek I, Schuschnigg S, Holzer C. 2016. *Effect of Particle Size on the Properties of Highly-Filled Polymers for Fused Filament Fabrication*.
99. Kong Z, Wang Z, Chen B, Li Y, Li R. 2023. Effect of Ball Milling Time on the Microstructure and Properties of High-Silicon-Aluminum Composite. *Materials (Basel)* 16

100. Hayashi K, Kishida R, Tsuchiya A, Ishikawa K. 2023. Superiority of Triply Periodic Minimal Surface Gyroid Structure to Strut-Based Grid Structure in Both Strength and Bone Regeneration. *ACS Applied Materials & Interfaces* 15:34570-7
101. Nimbalkar S, Dhatrak P, Gherde C, Joshi S. 2021. A review article on factors affecting bone loss in dental implants. *Materials Today: Proceedings* 43:970-6
102. Troulis MJ, Tayebaty FT, Papadaki M, Williams WB, Kaban LB. 2008. Condylectomy and costochondral graft reconstruction for treatment of active idiopathic condylar resorption. *J Oral Maxillofac Surg* 66:65-72
103. Feinerman DM, Piecuch JF. 1993. Long-term retrospective analysis of twenty-three Proplast®-Teflon® temporomandibular joint interpositional implants. *International Journal of Oral and Maxillofacial Surgery* 22:11-6
104. Gruskin E, Doll BA, Futrell FW, Schmitz JP, Hollinger JO. 2012. Demineralized bone matrix in bone repair: history and use. *Adv Drug Deliv Rev* 64:1063-77
105. Mardas N, Kostopoulos L, Stavropoulos A, Karring T. 2003. Denaturation of demineralized bone matrix significantly reduces bone formation by guided tissue regeneration. *Clin Oral Implants Res* 14:804-11

Appendix A

Chapter 1: Figures A.1-A.3

Chapter 2: No figures

Chapter 3: Figures A.4-A.7

Chapter 4: Tables A.1-A.2

Chapter 5: Figures A.8-A.9

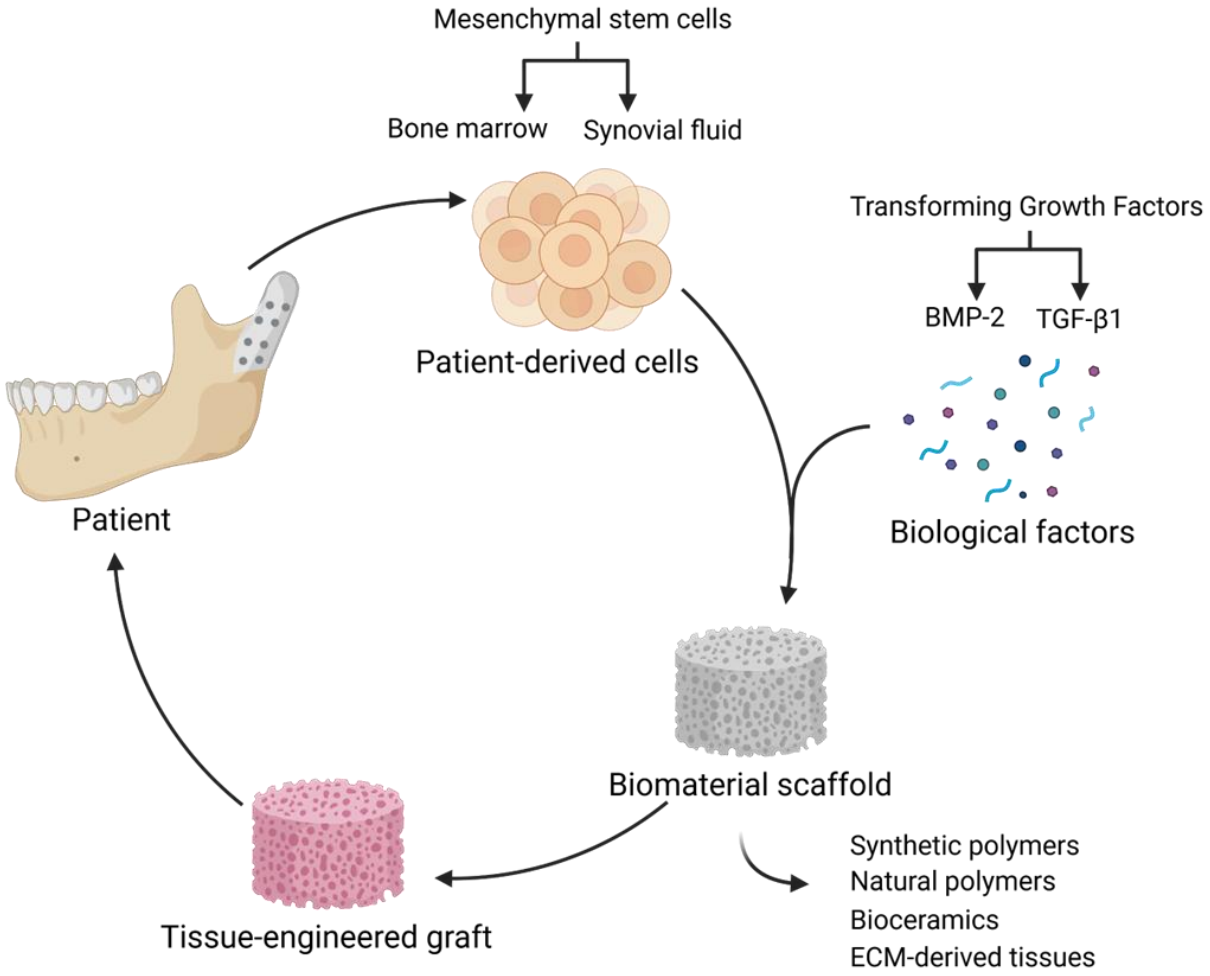

Figure A.1: Temporomandibular joint tissue engineering triad approach.

For patients indicated for a bioengineered prosthetic, the general approach includes patient-derived cells, biological factors (i.e., growth factors), and biomaterial scaffold. Temporomandibular joint (TMJ) patient-derived cells generally are aspirated from bone marrow in the iliac crest or harvested from the synovial fluid which surrounds the TMJ. Bone morphogentic protein-2 (BMP-2) and transforming growth factor-beta 1 (TGF-β1) have been shown to regulate and promote osteogenesis and chondrogensis. Synthetic polymers, natural polymers, bioceramics, and ECM-derived tissues have been used as biomaterial scaffolds. In combination, a tissue-engineered graft can be fabricated directly for the patient. Created in https://BioRender.com.

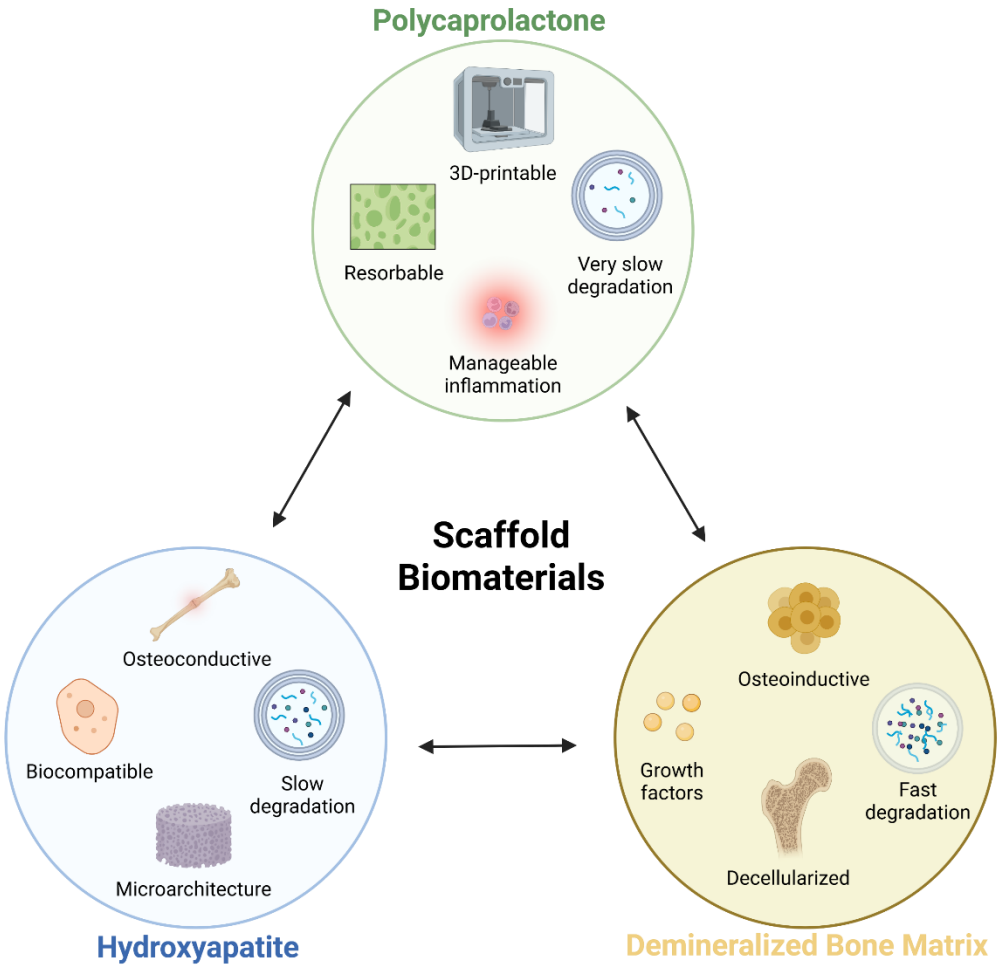

Figure A.2: Scaffold biomaterials allow for tailoring mechanical, degradation, and bioactive properties.

The sythetic polymer of choice was polycaprolactone (PCL), which is an aliphatic polyester. This material is bioinert, bioresorbable and displays a very slow degradation rate of 1-2 years in vivo. Combined with hydroxyapatite (HAp), the bioceramic material is highly biocompatible and osteoconductive, assisting with the guidance and facilitation of bone growth. For PCL/demineralized bone matrix (DBM), an osteoinductive material can be 3D-printed to induce osseo cells. DBM is generally composed of type I collagen and growth factors. Created in https://BioRender.com.

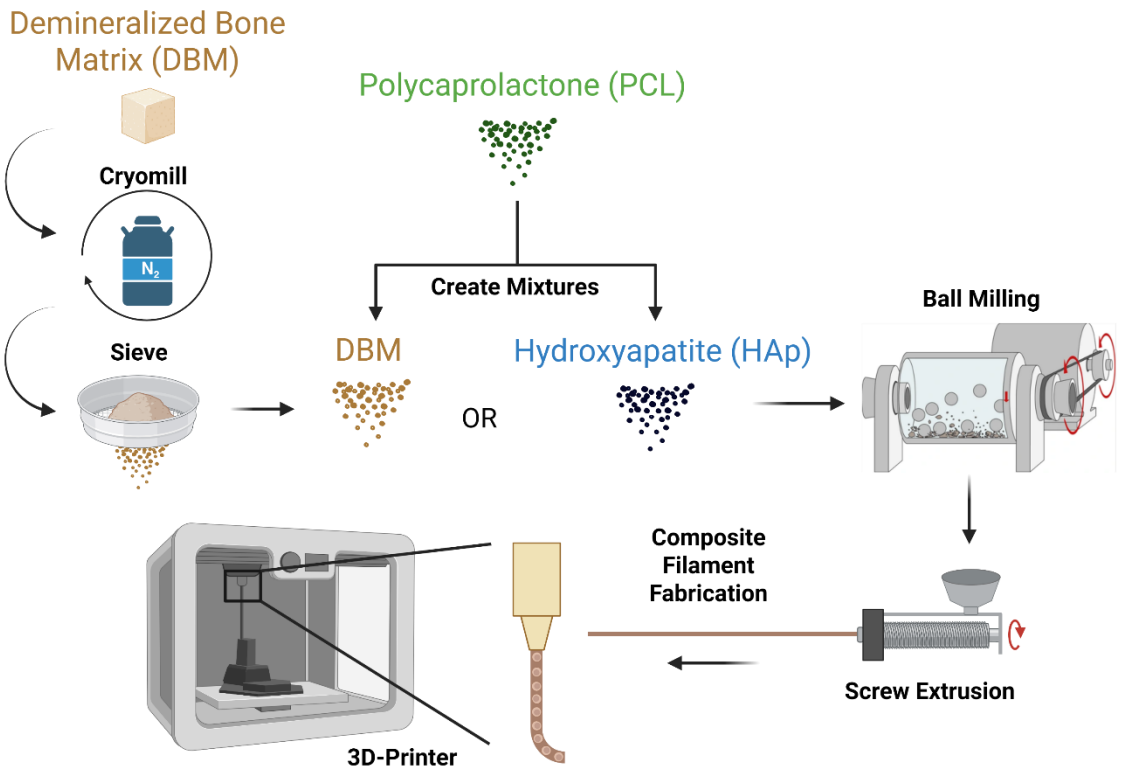

Figure A.3: Fabrication of biomaterial composites.

The illustration represents the pre- and post-processing of biomaterial composite fabrication. Demineralized bone matrix (DBM) is cryomilled onced and sieved to prepare for mixing. Polycaprolactone (PCL) and hydroxyapatite (HAp) composites are mixed at accurate ratios and ball milled for 6 hours. The resulting mixture is poured into the screw extrusion and filament fabrication setup to create 3D-printable filament for use in commerical 3D-printer. Created in https://BioRender.com.

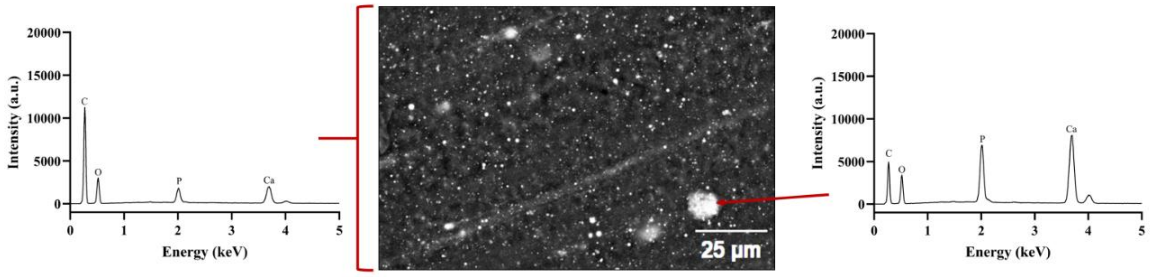

Figure A.4: Energy dispersive spectroscopy of 20 wt% HAp dot and rectangular mapping.

The raw electon count data were quantified for the entire rectangular mapping (left) versus bright white dot mapping (right). Higher amounts of Ca and P were displayed for the white dot, indicating higher amounts of HAp. The HAp retains excellent uniformity throughout this qualitative image.

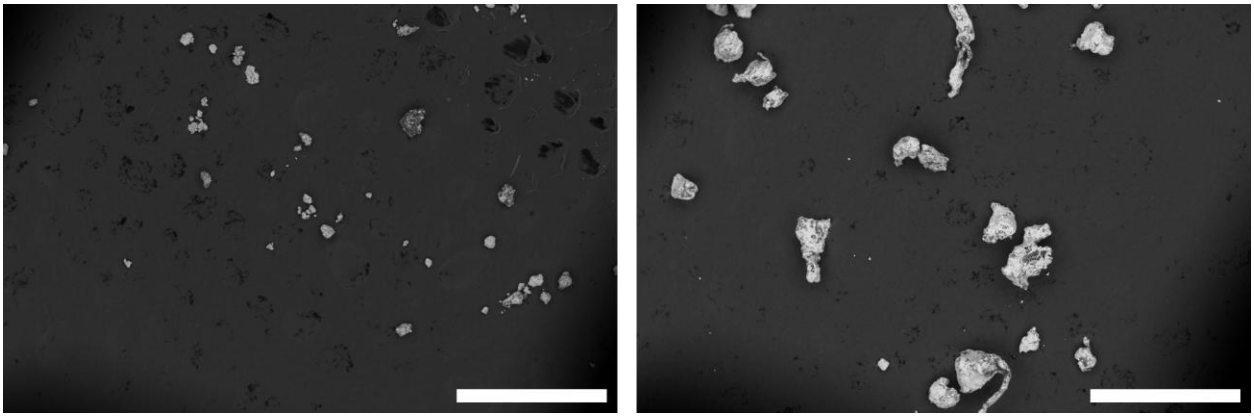

Figure A.5: Ball milling versus roller milling for 6 hours.

The positive control (20 wt% HAp) composite was used to compare the pre-processing ball milling methods. On the left, is planetarium ball milled 20 wt% HAp while the right image shows roller milled 20 wt% HAp, both after 6 hours. Scale bar represents 1 mm.

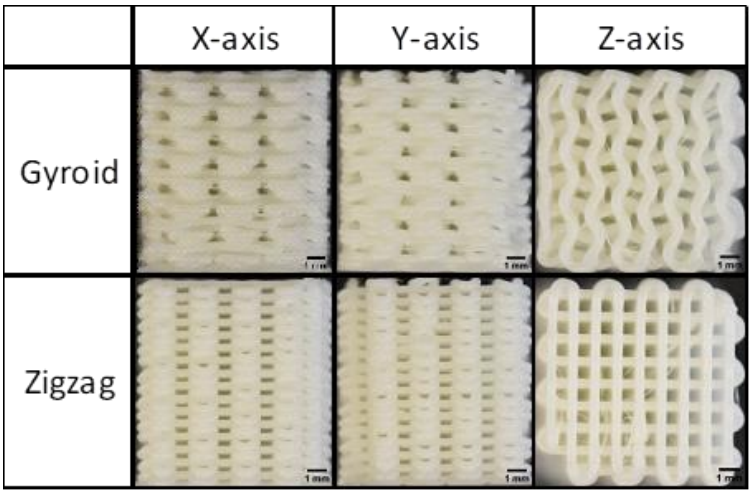

Figure A.6: Macroscopic images of microarchitecture.

Two microarchitectures were used to design a porous 10 x 10 mm^2 cubes, fabricated from PCL alone to assess the anisotropic mechanical properties. The x- and y-axis look roughly similar due to the 0- and 90-degree orientation between 3D print layers. The z-axis displays the unique properties of a gyroidal pattern. Scale bar represents 1 mm.

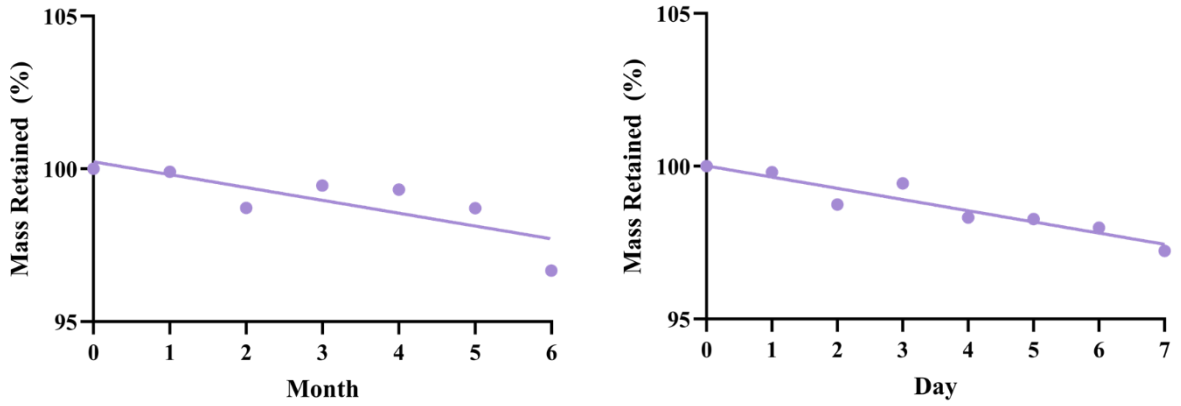

Figure A.7: Polycaprolactone long-term versus accelerated degradation.

PCL was submerged in phosphate-buffered saline (PBS) for 6 months to translate accelerated degradation conditions in 5 M sodium hydroxide (NaOH) for one week. The data were compared which elucidated that one month in PBS is similar to one day in 5 M NaOH. For sheep, the natural bone remodeling rate is every 3-6 months, suggesting we desire a material that last a full week under accelerated conditions.

Table A.1: Prosthesis Design Criteria

Constraint	Target	Justification
Enlarging ramus during digital prosthesis fabrication	1.65 mm scale	• Such an increment increases the feasibility of application during surgery. • 1:1 3D-FDM printed female and male counter parts are too tight using registered part.
Shorter flange	50 mm down ramus	• No irritation of soft tissues on the lateral-inferior edges of ramus. • Potential for non-degraded biomaterial
Thick flange	5 mm-3mm gradient	• More robust and increased mechanical performance
Posterior edge of flange	30 mm across ramus	• No irritation of soft tissues on the medial-posterior edges of ramus.
Posterior condyle smoothing	10 mm	• Increased mandibular condyle and ramus mimicry. • Increased mechanical performance
Dowel placement	Staggered 8 dowels	• Performing surgeon can choose. • Staggered advised by TMJ surgeon.
Hollow condyle	2.5 mm shell thickness	• House autologous ground bone and bone marrow compound.

Table A.2: Guide Design Criteria

Constraint	Target	Justification
Enlarging ramus during digital prosthesis fabrication	1.65 mm scale	• Such an increment increases the feasibility of application during surgery. • 1:1 3D-FDM printed female and male counter parts are too tight using registered part.
Shorter flange	50 mm down ramus	• No irritation of soft tissues on the lateral-inferior edges of ramus. • Potential for non-degraded biomaterial
Thick flange	5 mm-3mm gradient	• More robust and increased mechanical performance
Posterior edge of flange	30 mm across ramus	• No irritation of soft tissues on the medial-posterior edges of ramus.
Posterior condyle smoothing	10 mm	• Increased mandibular condyle and ramus mimicry. • Increased mechanical performance
Dowel placement	Staggered 8 dowels	• Performing surgeon can choose. • Staggered advised by TMJ surgeon.
Hollow condyle	2.5 mm shell thickness	• House autologous ground bone and bone marrow compound.

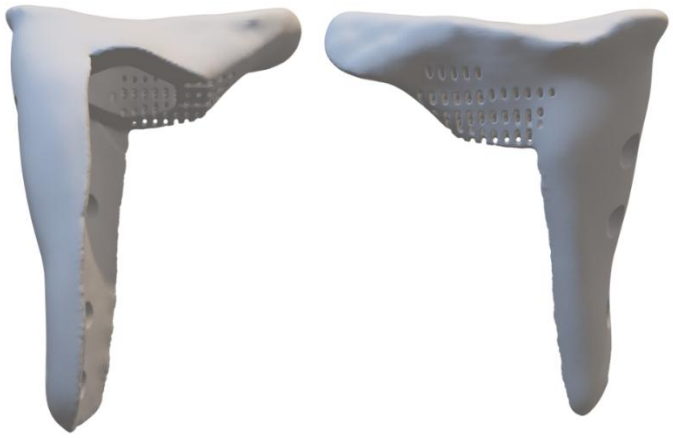

Figure A.8: Porosity generation on inferior side of prosthesis.

3D model of porosity generated on the inferior-posterior side of the prosthesis to not disrupt or interfere with TMJ disc translation on the anterior portion of the mandibular condyle. The inclusion of this microarchitecture may induce blood diffusion and waste management in the hollow cavity, allowing the thickening of the shell to further support masticatory loads.



Figure A.9: Tapered condyle-ramus interface.

During masticatory loads and daily usage, a tapered solution may enable the inhibition of sliding or micromotion. The opening would allow for blood transfer from the bone marrow of the resected ramus. In this 3D model, a 2.5 mm shell was used.